Modeling Buoyant Droplet Plumes in a Stratified Environment

by

Brian C. Crounse

Submitted to the Department of Civil and Environmental Engineering
in partial fulfillment of the requirements for the degree of

Master of Science in Civil and Environmental Engineering

at the

MASSACHUSETTS INSTITUTE OF TECHNOLOGY

June 2000

Author ....
Department of Civil and Environmental Engineering
May 5, 2000

Certified by ....
E. Eric Adams
Senior Research Engineer
Thesis Supervisor

Accepted by ....
Daniele Veneziano
Chairman, Departmental Committee on Graduate Studies

Modeling Buoyant Droplet Plumes in a Stratified Environment

by

Brian C. Crounse

Submitted to the Department of Civil and Environmental Engineering
on May 5, 2000, in partial fulfillment of the
requirements for the degree of
Master of Science in Civil and Environmental Engineering

Abstract

This work describes the formulation and application of a novel two-phase integral plume model. This model describes the characteristics of a vertical plume driven by the continuous release of dissolving buoyant droplets from a fixed point in a stratified, stagnant environment. Model development is motivated by a specific application, the injection of CO_2 into the deep ocean by means of a buoyant droplet plume. This application is one method of sequestering anthropogenic CO_2 emissions from the atmosphere. The goal of such measures is to reduce the environmental risks associated with atmospheric emissions. Of course, sequestration of CO_2 in the ocean introduces other environmental concerns, as dissolved CO_2 tends to lower seawater pH. It is also necessary to ensure that the CO_2 is delivered to a depth where it will not be transported to the surface over short time scales. To assess the feasibility and begin to estimate the potential for environmental impacts, a multinational group of researchers plans to conduct a pilot-scale field experiment in 2001.

The aim of this work is to build a model of a buoyant droplet plume that will aid both design and interpretation of the field experiment, as well as any production-scale CO_2 releases. Such a model is also applicable to other two-phase plume flows. To that end, an integral model is formulated which accounts for the dynamics of the primary processes associated with a droplet plume: buoyant forces acting upon the droplets and plume water, dissolution of the droplets, turbulent entrainment of ambient water into the plume, and buoyant detrainment, or "peeling." The resulting model, at its core, is expressed as a set of nonlinear, coupled differential equations.

Typical integral plume models are one-dimensional, initial-value problems which require a single integration to solve the governing equations. The particular nature of the class of plumes under investigation (droplet plumes where droplet buoyancy decreases with height due to dissolution, and dissolved CO_2 increases fluid density), however, is characterized by regions of upward flow, driven by the buoyant droplets, and downward flow, driven by stratification and other density effects. As these flows are coupled, solution of the governing equations for flow in each direction is iterative, increasing the complexity of the solution scheme.

One implicit model assumption is that plume fluid in the vicinity of the droplets advects in the same direction as the droplets. As some coarse grid models predict that the fluid actually flows in the opposite direction, some scoping experiments were carried out to verify the nature of the velocity profile in a countercurrent droplet plume.

The model is analyzed for sensitivity to both design variables, such as the flow rate of droplets at the source, and parameters which are uncertain, such as turbulent entrainment coefficients and droplet dissolution rates. In the case of CO_2 droplets, the dissolution rate is quite uncertain due to the formation of hydrates on the droplet surface, whose effect on mass transfer is poorly understood. Fortunately, it is clear that reduced mass transfer rates can be offset by reducing the size of the droplets. Also, while plume characteristics such as plume height are sensitive to parameter uncertainty, the dilution of CO_2 is strongly controlled by quantifiable factors such as the CO_2 mass flux and the ambient stratification. This is attributable to the density effect of dissolved CO_2; high concentrations of dissolved CO_2 creates negative buoyancy which induces mixing. This mixing aids dilution.

The model is also compared to datasets describing different plume regimes in order to assess its validity. Though, when tuned to a given situation, the model agrees well with the data, there is no set of parameters which is universally applicable. Although the reasons why some parameters, such as the entrainment coefficients, change from case to case are partially understood, parameter uncertainty limits the accuracy of the model. In the case of a CO_2 droplet plume, the rise height predictions are estimated to be accurate to within ±30 percent.

Thesis Supervisor: E. Eric Adams
Title: Senior Research Engineer

Acknowledgments

I would like to acknowledge the the National Science Foundation for providing me with a Graduate Research Fellowship, and to the many sponsors of the CO_2 field experiment project, including the United States Department of Energy.

On the international front, I wish to thank Guttorm Alendal of the Nansen Center and Toru Sato of the University of Tokyo for sharing their work. I would also like to acknowledge all those involved with the CO_2 sequestration experiment with whom I have worked, including, but not limited to, Perry Bergman of the U.S. DOE, Stephen Masutani of the University of Hawaii, Lars Golmen of NIVA, Rick Coffin of NRL, and Howard Herzog of the MIT Energy Lab.

There are several more people at MIT whom I would like to thank. These include fellow Parsons Lab students Scott Rybarczyk, Durelle Scott, and Megan Kogut, for their good humor, and Assistant Director of the Parsons Lab, Sheila Frankel, for keeping things lively. I would also like to thank fellow graduate student Scott Socolofsky for all his help, which ranged from configuring Linux installations to editing manuscripts to teaching me how to body-surf in Hawaii. Tim Harrison, an MIT senior, was instrumental in carrying out the scoping experiments of Chapter 3. I also wish to thank my thesis advisor, E. E. Adams, for his kindness and patience. I was always amazed by how often a quick stop by his office evolved into a lengthy, constructive discussion.

Finally, I would like to thank my family for supporting me these past few months. I especially thank my wonderful wife, Madeleine. I am lucky to be married to her.

I dedicate this work to my father, Jerome B. Crounse.

Contents

List of Figures

List of Tables

Chapter 1

Introduction

This work is concerned with modeling the flow structure of a plume induced by the continuous release of bubbles, droplets or particles at a fixed point in a water body. Although the model described herein is applicable to a wide range of two-phase plume flows, this work is motivated by an application involving the intentional release of dissolving CO_2 droplets in the ocean. Model applicability is limited to the consideration of plume flows in environments without ambient currents. This limit is applied in order to minimize the number of dynamic processes involved, and because the no-current case probably represents a worst case scenario in terms of dilution of the droplet material.

1.1 Carbon Dioxide Sequestration

The application motivating this study is, ultimately, the threat of global warming due to anthropogenic emissions of greenhouse gases such as carbon dioxide. While it is beyond the scope of this work to assess the risks associated with greenhouse gas emissions, it is worth

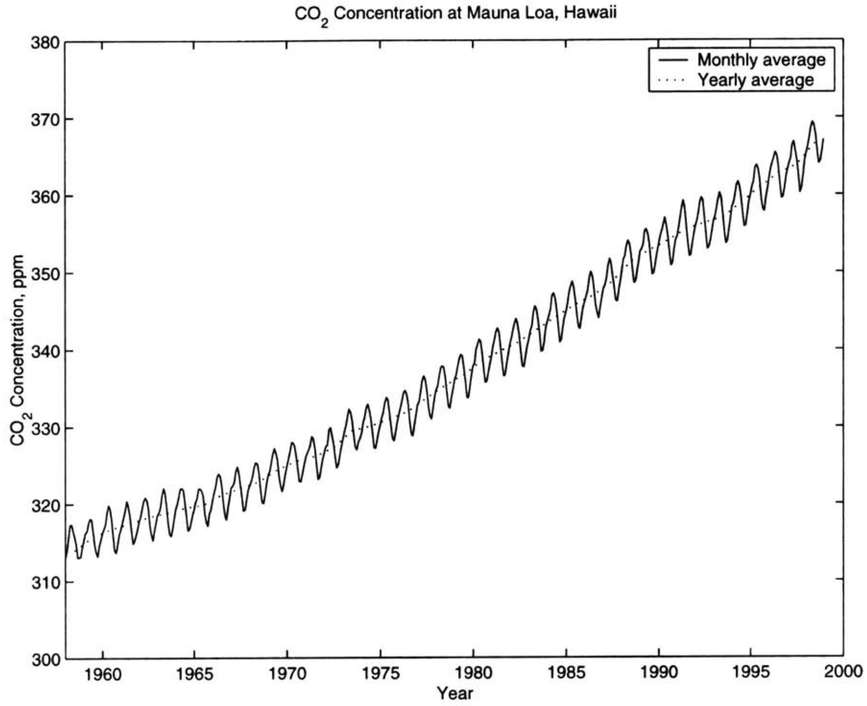

Figure 1-1: CO_2 concentrations measured at Mauna Loa, Hawaii. Source: C. D. Keeling and T. P. Whorf, Scripps Institute of Oceanography [34].

briefly reviewing a few broad trends.

1.1.1 Background

The time series of atmospheric CO_2 concentration is shown in Figure 1-1. The global temperature trend is shown in Figure 1-2. In addition to this trend in atmospheric temperature, recent work indicates that the globe's oceans have measurably warmed over the past fifty years, with the upper 300 meters of the world's oceans warming by 0.3 degrees C, which corresponds to an increase of energy of about 10^{23} Joules [38].

The trends in greenhouse gas concentrations and global temperatures are well-correlated.

Furthermore, no one disputes the fact that these so-called greenhouse gases, such as methane and carbon dioxide, absorb thermal radiation eminating from the globe's surface, thereby trapping heat. The remaining uncertainty is whether other factors in the climate system serve to reduce or amplify this thermal forcing. The risks involved with this uncertainty are great enough to cause any risk-averse individual or society to consider substantially reducing greenhouse gas emissions. Of course, there are many options for reducing fossil fuel consumption and thus emissions reduction, including more efficient use of energy and the adoption of alternative, less emissions-intensive energy sources. However, the unfortunate reality is that humans will most likely continue to combust significant amounts of fossil fuels for many years to come. One approach to controlling atmospheric CO_2 emissions from fossil

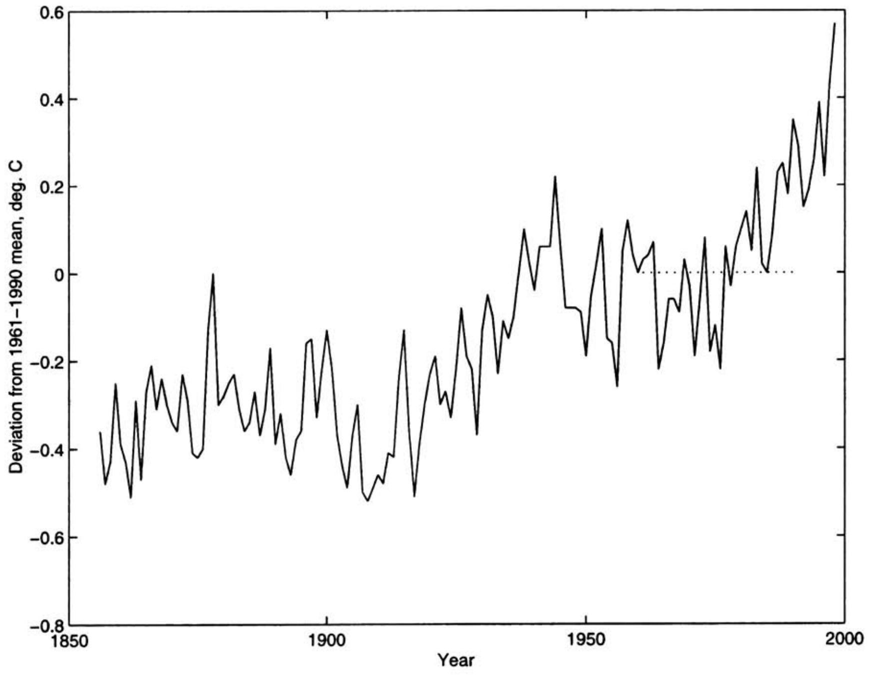

Figure 1-2: Global average surface temperature deviations from the 1961-1990 average. Source: Jones et al. [33]

fuel combustion is to capture and sequester the exhaust CO_2 away from the atmosphere. There are several locations where the captured CO_2 could be stored, including unminable coal beds, deep saline aquifers, depleted oil and gas reservoirs, and even mined salt domes [29].

1.1.2 Ocean Sequestration

Perhaps the most promising sequestration medium is the world's oceans, which currently hold about sixty times as much carbon as the atmosphere, and are capable of holding much more. The concept of ocean sequestration was formally introduced by Marchetti [41], who argued that injecting CO_2 into the ocean would speed up the natural process of CO_2 uptake into the ocean by chemical and biological processes.

Several techniques for transferring CO_2 to the deep ocean have been proposed. One proposed method is to release the CO_2 as buoyant droplets at an intermediate depth, allowing them to rise and dissolve before reaching the ocean's thermocline, which serves as a cap inhibiting mixing between the surface and deep ocean. Of course, over long time scales (hundreds of years), CO_2 concentrations will equilibrate between the ocean and atmosphere. The intent of such a sequestration strategy, then, is to minimize atmospheric CO_2 concentrations over the next few hundred years, by which point, presumably, humans' CO_2 emissions will have significantly decreased [3].

Introducing CO_2 into the deep ocean in this manner has potential environmental impacts. The main concerns are that high concentrations of dissolved CO_2 can cause respiratory distress in macrofauna [61], and that increasing the inorganic concentration of carbon in seawater tends to lower the pH, as CO_2 dissociates into bicarbonate, HCO_3^- [45]. The latter effect is of great concern, as the pH of ocean water is quite sensitive to the concentration of total dissolved inorganic carbon (DIC). Thus, the primary concerns of designing a CO_2 sequestration system are its effectiveness at sequestering CO_2, and the potential for environmental impacts.

Of course, current practices already impact the oceans, even if the warming of the world's oceans is not attributed to greenhouse gas emissions. Increased DIC concentrations due to increased atmospheric concentrations have been detected to depths of up to 1000 meters [28]. Increasing DIC levels in the productive surface waters, and thereby altering the carbon chemistry, could have significant impacts on important ecosystems. And if a rising atmospheric CO_2 concentration does cause significant global warming, the warming of the surface ocean is also problematic. Wallace Broecker has suggested a graver possibility: He suggests that global warming could cause the oceans' thermohaline circulation system to adopt a different mode of operation, which would result in dramatic changes in ocean circulation, with unknown impacts [15]. The environmental impacts of CO_2 ocean sequestration must be weighed against these effects.

The possible impacts of decreased pH on passive marine organisms due to the deliberate injection of CO_2 into the deep ocean have been estimated in work previously performed at MIT [4, 3, 10, 17]. For the case where CO_2 is injected by means of a droplet plume, these studies found that the greatest threat to plankton and similar biota was exposure to moderate pH depressions over intermediate time scales of days to weeks. These studies showed that the local impacts due to a CO_2 droplet plume could become negligible if the injected CO_2 is effectively diluted and dispersed at the source.

1.1.3 International Field Experiment

Japan, Norway, the United States, Canada, and Australia, as well as the company ABB, are currently involved in a joint research project evaluating CO_2 sequestration. As part of this project, researchers plan to conduct a field experiment involving the release of CO_2 as buoyant droplets in the ocean at a depth of about 800 meters. The mass flow rates envisioned for the experiment are in the range of 0.1 to 1.0 kg/s. The goals of this experiment are to better characterize the physics and chemistry associated with a CO_2 droplet plume, to evaluate the feasibility of the technique, and to develop effective monitoring techniques for future experiments [5]. Because many of the processes affecting the behavior of the plume are poorly understood, it is desirable to develop a model of the release in order to aid design of the experiment, and, once validated, to extrapolate the experimental results to other release situations. It is in this context that the current work is motivated.

1.2 Two-Phase Plumes

The dynamics of two-phase plumes are of interest in many contexts: air bubbles plumes are used for applications such as the mixing and aeration lakes [69], and accidental oil well blowouts can result in plumes driven both by oil droplets and natural gas bubbles [70]. Use of two-phase plumes as a means of delivering CO_2 to the deep ocean is a relatively recent notion. Before delving into the model formulation, it is worthwhile reviewing plume physics and the type of modeling approach used in this work.

1.2.1 Phenomenological Description

Single-phase plume flows occur when a concentrated source of buoyancy is introduced into a fluid. This buoyancy source may be the input of fluid with a different density than that of the ambient fluid, due, for example, to a difference in temperature or salinity, or it may be the input of an agent such as heat which alters the density of the receiving ambient fluid. In either case, the buoyancy causes fluid advection, which will be primarily vertical in the case where there is no ambient current. In almost all environmental flows, the induced flow is turbulent. The rising turbulent flow, in turn, induces ambient fluid to flow into the plume through a process known as turbulent entrainment— essentially, turbulent eddies in the plume "grab" ambient fluid. The resulting flow structure exhibits self-similarity— the cross-sectional profiles of velocity and density have the same near-Gaussian shape at all heights away from the source, and may be described by two parameters, a centerline value and a nominal width. The property of similarity occurs because the flow has no inherent length-scales. The scale of the plume flow in a stagnant, unstratified environment is primarily governed by the buoyancy flux [25].

Plume flows behave somewhat differently when the ambient fluid is stably stratified. In the unstratified case, the plume's density is always less dense than the ambient fluid, and it will continue to rise until an obstruction such as the fluid surface is encountered. When ambient stratification is present, this is no longer the case— as fluid rises in a plume, its density, relative to the adjacent ambient water, increases. At some height, the plume fluid becomes negatively buoyant, and at some height above that, it ceases to rise. The fluid then falls back a short distance until it reaches a point of neutral buoyancy, and begins to flow horizontally, intruding into the ambient water column as a gravity current. This is known as "trapping". Such plumes are not strictly self-similar, although the self-similarity approximation has been employed in previous models successfully.

The height at which the plume fluid intrudes into the environment has been shown to be

$$h_T = 3.8 \left(\frac{B_0}{N^3} \right)^{\frac{1}{4}} \tag{1.1}$$

where B_0 is the source buoyancy flux and N is the buoyancy frequency, $N^2 = g(d\rho/dz)/\rho_{ref}$; the reference ρ_{ref} is a density typical of the environment in the vicinity of the plume [65].

A two-phase plume differs somewhat from a single-phase plume. In such a plume, a dispersed phase, composed of buoyant bubbles, droplets, or particles (for brevity, hereafter referred to primarily as "droplets"), provides the initial buoyancy. The movement of these agents of buoyancy is partially determined by the plume flow and partially by the dynamics of the droplets, both individually and as a group. As a result, the plume buoyancy advects somewhat independently from the plume itself. In the unstratified case, this does not dramatically affect the character of the plume. However, when the ambient is stratified, or a crossflow is present, the droplets and the bulk plume flow can separate due to significantly different trajectories.

For example, when the ambient water column is stratified, plume fluid driven by buoyant droplets is initially pulled upward in the droplet's wakes (this work assumes rising droplets, although it is equally applicable to sinking ones). However, this fluid becomes progressively denser than the adjacent ambient water due to the latter's stratification. At some height, the negative buoyancy of the plume fluid is greater than the positive forcing of the droplets, and the plume fluid's velocity decreases and eventually reverses. At this point, this dense fluid leaves the plume core. This is called "peeling" or "buoyant detrainment". Unlike the case of the single-phase plume, the peeling fluid may be well above the elevation at which it would be neutrally buoyant. Thus, it must descend a significant distance, mixing with both the ambient water column and plume core, until it reaches neutral buoyancy and forms an intruding gravity current, or "intrusion."

The details governing peeling are not well understood. What is known is that the modes of peeling can be divided into two basic categories, based on the droplet slip velocity, source buoyancy flux, and strength of stratification. In one mode, where the droplet slip velocity is low relative to the characteristic plume velocity (which scales with the buoyancy flux and the strength of the stratification), peeling events are discrete, and occur over a vertical distance that is small relative to the size of the plume. The convention is call these Type 2 plumes. If the slip velocity is very high, fluid peels from the plume in a more continuous manner—essentially, the bubbles do not effectively transmit the buoyant forcing to the plume fluid. Such plumes are labeled Type 3 plumes [9, 59].

Socolofsky [58] found that plume type could be predicted with just one dimensionless number, the dimensionless slip velocity,

$$U_N = \frac{u_b}{(B_0 N)^{\frac{1}{4}}}, \tag{1.2}$$

where u_b is the bubble slip velocity. When U_N is below 1, the bubble slip velocity is so low that the bubbles themselves peel with the fluid, spreading out the bubbles laterally and creating a more diffuse plume. Socolofsky refers to these plumes as Type 1*; the asterix

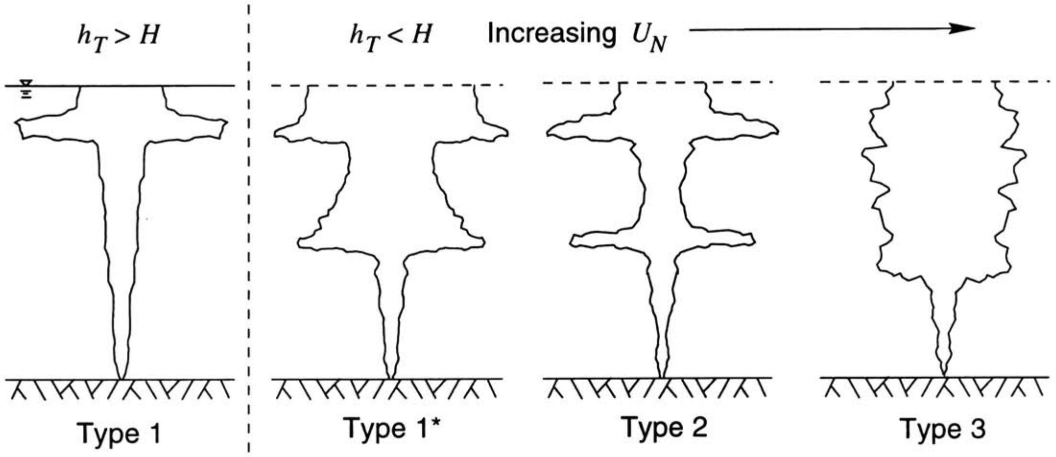

Figure 1-3: Plume type classification. H represents the water depth. Source: Socolofsky [59].

serving to differentiate the type from the classification scheme of Asaeda and Imberger, in which a Type 1 plume is merely one that does not peel before reaching the water surface. For $1.4 < U_N < 2.4$, the plume is a Type 2. For $U_N \geq 2.4$, the plume behaves as a Type 3 with unsteady peeling. Figure 1-3 contains schematics of the different plume types.

1.2.2 Modeling Approach

A modeling technique known as integral modeling has been employed successfully in the past to describe the gross characteristics of single- and two-phase plumes [9, 22, 42, 43, 49, 69]. This approach involves describing the plume structure in the simplest possible terms. Rather than attempting to solve a boundary value problem subject to the Navier-Stokes equations, or some approximation thereof, an integral model relies on the basic Newtonian principles of conservation of mass and momentum and the assumption that the flow is approximately self-similar. Details of the fluid dynamics of the flow are modeled with established parameterizations. By doing so, a three dimensional flow structure can be described by a set of one-dimensional variables; the one dimension preserved is the direction of mean flow. These variables describe plume characteristics such as its nominal width and mean centerline velocity. Collapsing a three dimensional boundary value problem into a one dimensional initial value problem necessarily leads to a simplified description of the plume; however, this simple model supplies information sufficient for engineering purposes.

1.2.3 Previous Work

There is a healthy body of published work concerning bubble plumes. This section briefly reviews some key contributions.

Kobus [35] presented one of the first theoretical studies of bubble plume flows. His experimental bubble plume data indicated that the radial velocity profiles were approximately Gaussian, and concluded that the plumes were approximately self-similar. Ditmars and Cederwall [22] applied an integral model to Kobus's data, incorporating the entrainment assumption. Wilkinson [68] noted that bubble plumes lose their similarity for large source Weber numbers because of the formation of a gaseous core. Chesters, van Doorn and Goossens [19] examined unstratified bubble plume flows. Their analytical treatment indicated that unstratified plume behavior is primarily determined by the initial bubble buoyancy flux, is relatively insensitive to parameters such as bubble slip velocity, and thus acts much like a single-phase plume. Their experimental work showed that bubble slip velocity did not vary significantly with radial location and was comparable to the isolated-bubble slip velocity. They also suggested that the turbulent component of momentum flux, usually ignored in integral models, can be significant. Tacke et al. [60] measured axial and radial distributions of gas concentration and bubble frequency for two-phase plumes with compositions of air/water, helium/water, and nitrogen/mercury. Milgram [43] performed large-scale bubble plume experiments. The primary contributions of this work were correlations for the rate of entrainment and the magnitude of turbulent momentum flux as functions of local plume conditions. Leitch and Baines [36] conducted elegant bubble plume experiments. They emphasized the effect of bubble turbulence on turbulent momentum flux and the rate of entrainment into the plume, and found that the plume fluid volume flux does not scale with height quite like a single-phase plume. Brevik and Kluge [13] presented an analysis in which the entrainment assumption is replaced with the kinetic energy equation and an assumption about self-preservation of the Reynolds stresses.

Only a few researchers have examined bubble plumes in stratification. McDougall [42] developed the first "double-plume" model, which is discussed in greater detail in Section 2.1, as are the models of Liro et al. [39] and Asaeda and Imberger [9]. Asaeda and Imberger also introduced two dimensionless numbers which correlated with plume type. Schladow [57] reported on a numerical model of a bubble plume coupled to a reservoir mixing model. Baines and Leitch [11] conducted experiments which focused on the evolution of stratification profiles mixed by a bubble plume. Wüest et al. [69] described a numerical model for bubble plumes in lakes which incorporated bubble dissolution. Lemckert and Imberger [37] took field measurements of a bubble plume in a stratified reservoir. Their limited velocity measurements indicated that the plume velocity profile was not Gaussian.

Reingold [53] studied the dependence of the height of the first peel of a two-phase plume on the slip velocity of the dispersed phase. To control the particle slip velocity, Reingold used sediment particles of known size to form upside-down plumes in some experiments, in order to regulate the slip velocity. Socolofsky [58] extended this work and suggested correlations predicting the height and volume flux of the initial intrusion as functions of the particle slip velocity u_b, initial buoyancy flux B_0, and ambient stratification N:

$$\frac{h_T}{(B_0/N^3)^{\frac{1}{4}}} = 3.8 - 1.2\left(\frac{u_b}{(B_0N)^{\frac{1}{4}}}\right)^{0.5} \tag{1.3}$$

$$\frac{Q_i}{(B^3/N^5)^{\frac{1}{4}}} = 1.4 - 0.8\left(\frac{u_b}{(B_0N)^{\frac{1}{4}}}\right)^{0.2} \tag{1.4}$$

The constants on the left hand side, 3.8 and 1.4, are the appropriate values for a single-phase plume in stratification, where $u_b = 0$. These correlations are examined in Section 4.3.3.

1.2.4 Modeling Strategy

There are, of course, many different methods of mathematically modeling fluid dynamics. The most general method is to impose boundary conditions for a flow of interest and then solve the 3-D, time-dependent Navier-Stokes equations at a finite set of points. In addition to being computationally intensive, the model acts as a sort of "black box", in that construction of the model yields little intuitive insight into the character of the flow. Furthermore, such models are inevitably limited by the resolution of the model mesh. Computational constraints generally do not allow a grid spacing that resolves the smallest scales of turbulence, so that a turbulence model must be invoked. Similarly, in flows where both small-scale and large-scale features are of interest, it may not be practical to resolve the former. In short, while Navier-Stokes models are quite powerful and rely on as few simplifications as possible, they do have significant limitations.

The great advantage of the integral modeling approach is its conceptual and numerical simplicity. The main properties of the flow are described by a set of first order differential equations as an initial value problem, which is much simpler to solve than the Navier-Stokes equations. Furthermore, the process of constructing the model yields insight into the important factors controlling the flow. Thus, integral models yield information about the large-scale nature of a flow more easily than more complex models.

Integral modeling, of course, also has several disadvantages. The fact that it does not resolve small-scale features of the flow (such as the character of the turbulence) limits the contexts in which it is a pertinent modeling strategy. Another disadvantage, which is always pertinent, is its reliance on several simplifying assumptions. In the case of simple jets and plumes, these simplifications have been rigorously demonstrated to be valid and appropriate. In the case of bubble plumes in stratification, assumptions such as those regarding the behavior of the bubble core and the rate of entrainment are not as well established, and must always be viewed critically.

1.3 Scope

The scope of this study is to develop a numerical model to predict the gross characteristics of a stationary, point-source CO_2 droplet plume in a stratified water column without significant crossflow. The purpose of this study is to assist the design of the international CO_2 field experiment by determining what source conditions are likely to produce a plume of acceptable height ($O(100m)$) for the experiment, and to predict the dilution of the CO_2. Once validated, the model could be used to predict the behavior of plumes with a wider range of parameters than those actually measured during the experiment. Supporting these applied goals, another more fundamental aim is to use the model to gain insight about certain aspects of two-phase plume behavior.

Chapter 2

Model Formulation and Solution

This chapter describes the formulation of the numerical model employed in this work. First, the integral models upon which the current formulation is based are reviewed. The primary state variables are then defined, and the general forms of the governing equations controlling these variables are introduced. The terms of these equations generally represent submodels which are described in turn. The chapter ends with a description of the methods used to solve the system of governing equations.

2.1 Pertinent Integral Models

Models of two-phase plumes in stratification can be considerably more complex than models of stratified single-phase plumes or unstratified two-phase plumes. The primary source of complexity arises from the separation of the plume fluid from the droplets at peeling events. Any attempts to account for the dynamics of the fluid descending from a peeling event add more complexity.

Liro [39] developed a model for the same primary application as the current work, deep ocean sequestration of CO_2. In this model, the governing equations are integrated upward from the release just like a conventional integral model. This model also defined peeling criteria for the plume so that, at whatever heights the plume met the criteria (which are described in Section 2.3.8), a portion of the plume was removed in order to simulate a peeling event. This model did not attempt to explicitly model the dense detrained fluid.

Schladow [57], in a study of the evolution of stratification of a water body mixed by an air bubbler, described another model which included peeling events. In this model, water leaving the rising plume at a peeling event was assumed to intrude into the ambient environment at the depth at which it would be neutrally buoyant. Thus, this model was based on the first order approximation that the water in the descending portion of the plume does not mix with either the rising plume or the ambient.

McDougall [42] presented the first double-plume model for bubbles plumes in stratified environments. The formulation of this model was based on observations of laboratory experiments. McDougall observed that the plume consisted of an upward flowing inner core composed of an bubble-water mixture. This inner plume had a roughly constant radius and velocity with height. Outside of this core, a concentric flow consisting only of water flowed upward. The flow in this outer plume slowed with height, eventually stopping and forming a horizontal intrusion. McDougall also observed a a descending flow outside the inner core just above the intrusion. At some point above that region, the plume was observed to restart with both inner and outer cores flowing upward.

McDougall proposed an integral model based on the decomposition of the plume into two upward coflowing annular flows. In this model, the inner and outer plumes are treated as separate entities with separate volume, momentum, and buoyancy fluxes. This model formulation has a few shortcomings. First, as McDougall noted, the model cannot be applied in the region of an intrusion; integration of the governing equations must be stopped below the intrusion, and restarted at a point above the intrusion where there is minimal flow in the outer plume. Second, the model does not provide insight concerning the nature of the outer plume above an intrusion, where it was observed to flow downward. Finally, aspects of the model are not consistent with the governing physics: fluid lifted by bubbles in the inner core is more dense than than the ambient when it is forced to peel by buoyant forces; it should then descend a significant distance until it reaches neutral buoyancy, mixing with the plume and the ambient fluid as it descends. Although McDougall observes a downward flowing plume above intrusions, this model fails to describe it.

Asaeda and Imberger [9] formulated a different double plume model. In this model, the inner plume encompasses both the bubble-water core and the surrounding upward-moving fluid, while the outer plume consists of fluid descending from a peel. To solve the governing equations of this model, the governing equations of the inner plume are integrated from the release to the point where the momentum flux of the inner plume approaches zero. At this point, Asaeda and Imberger approximate the peeling process by assuming that 100 percent of the inner plume fluid exits the plume and begins to descend. This is the start of an outer plume section. As the outer plume descends, it mixes with the inner plume and the ambient environment in a manner similar to McDougall's outer plume.

In this model, fluid in the outer plume descends until it reaches neutral buoyancy, at which point the outer plume is assumed to form an axisymmetric intrusion into the ambient environment. As the properties of the inner plume had been calculated without the presence of the outer plume initially, the process of integration of the inner plume, and then the outer plume, must be repeated until the system converges. Once convergence is achieved, the inner plume is re-initialized above the previous peel location, and the process is repeated until the water surface is reached. Although this integral model is still computationally cheap compared to a 3-D fluid dynamics numerical model, iteration does complicate model evaluation.

The Asaeda and Imberger model forfeits the McDougall decomposition of the inner plume. McDougall's treatment is useful because it allowed the air-bubble core to have a significantly higher velocity than the rest of the upward-flowing fluid, which is phenomenon observed in field experiments [37]. This type of velocity profile also causes one to suspect the validity of the self-similarity assumption, which is implicit in the integral models, although the field study did not provide enough data to evaluate this question. The Asaeda and Imberger formulation could be extended into a triple plume model, in which the inner plume is divided into McDougall's two rising plumes. However, as the mixing assumptions between two plumes are not well known, adopting another mixing interface is unlikely to improve modeling accuracy.

The Asaeda and Imberger model formulation is an improvement over the McDougall model in that it better accounts for the fact that the location of the intrusion is generally significantly below the depth of the peeling event. The assumption that all of the plume fluid detrains at a peeling event is reasonable, as the actual percentage for a Type 2 plume is approximately 90 percent [59]. It also guarantees that the outer plume will intrude at some depth between peeling events, and cannot overlap a lower outer plume segment, avoiding a potential modeling complication. This approach is only appropriate for standard Type 2 plumes.

2.2 Model Formulation

The spatial evolution of a two-phase plume is controlled by four primary processes: buoyant forces acting upon the droplets and plume water, dissolution of the droplets, turbulent entrainment of ambient water into the plume, and buoyant detrainment, or "peeling".

This integral model of two-phase flow essentially consists of a definition of flux quantities which describe the plume and the formulation of governing equations which describe the vertical evolution of these quantities. The other primary ingredient is an algorithm for solving the governing equations.

This model adopts the Asaeda and Imberger [9] decomposition of the plume into a rising inner plume and descending outer plume sections. Because the velocity and density profiles of bubble plumes in stratification have not been observed in detail experimentally, and are not likely to be Gaussian, this model also employs "top-hat" profiles within the respective plumes. This model neglects details of the plume turbulence; the plumes are described by characteristic mean velocities. Pertinent artifacts of the turbulent nature of the flow are parameterized explicitly, as discussed in section 2.3.4.

Given this modeling framework, the next step is to define the pertinent integral flux quantities. One quantity is the flux of droplet mass, W_b. In this model, the released droplets

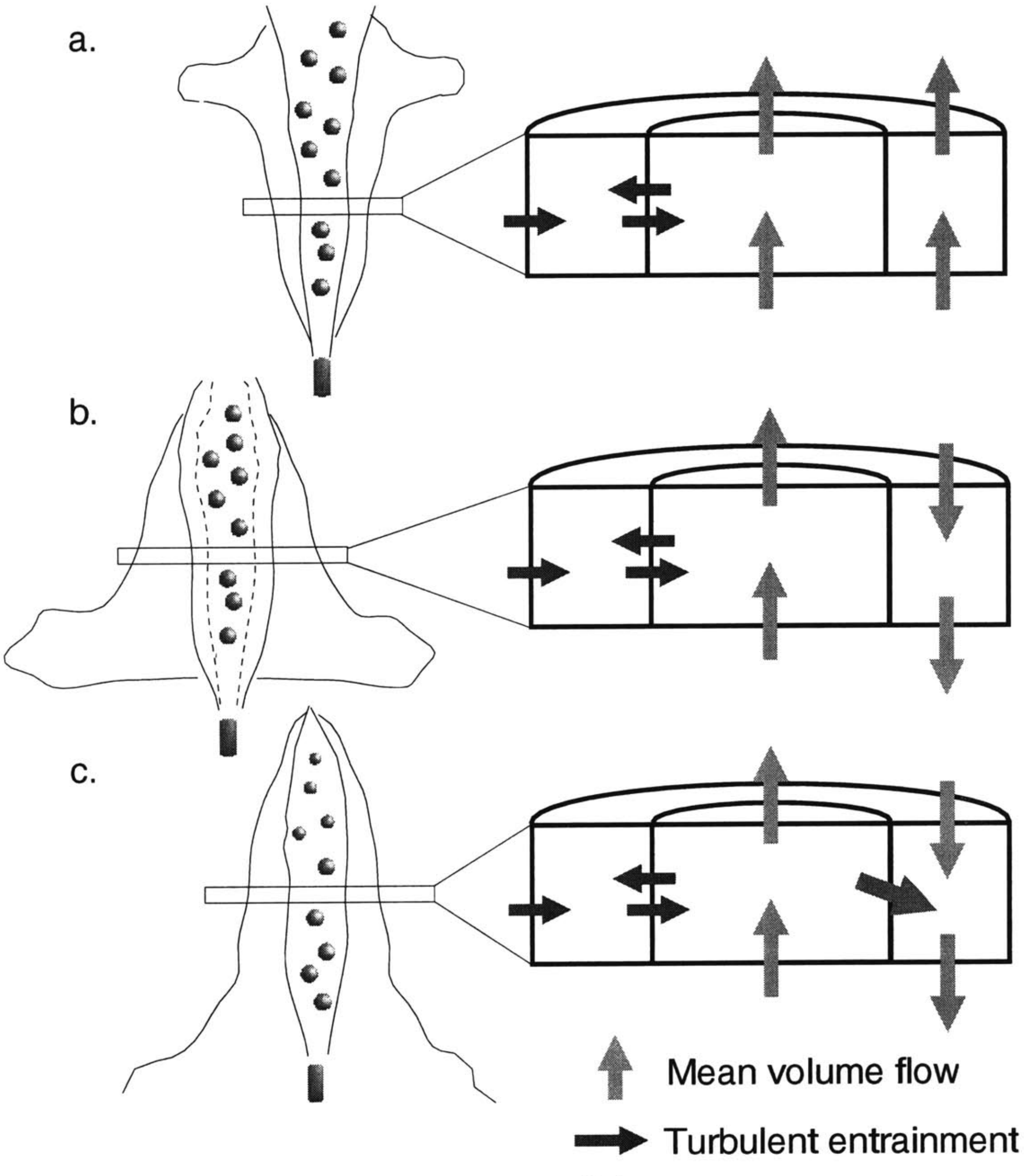

Figure 2-1: Plume Model Schematics. a. McDougall's coflowing model. b. Asaeda and Imberger's counterflowing model. The bubble core is narrow than the rising inner plume. c. The present model. This formulation includes bubble dissolution and continuous peeling based on local plume conditions.

are all assumed to be identical in size, with an effective spherical diameter d_b. Also, the number flux of bubbles, N_b, is assumed to be constant with height, which implies that bubble fracturing and coalescence are insignificant (or balance one another). Denoting the droplet material density as ρ_b, the mass flux of droplets is defined as

$$W_b(z) = Q_b(z)\rho_b(z) = \frac{1}{6}\pi d_b^3(z) N_b(z)\rho_b(z), \tag{2.1}$$

where Q_b is the droplet volume flux and ρ_b is the droplet density.

The buoyancy flux associated with the droplets is defined as

$$B_b(z) = gQ_b(z)\frac{\rho_a(z) - \rho_b(z)}{\rho_{ref}} \tag{2.2}$$

where ρ_a is the *in-situ* density of the ambient water column, and ρ_{ref} is an arbitrary reference density, $\approx \rho_a$. As buoyancy fluxes such as B_b are tracked as dependent variables in this model, the choice of ρ_{ref} is unimportant.

The volume flux of fluid in the inner plume is defined as

$$Q_i(z) = (1 - C_b(z))\pi b_i^2(z)u_i(z) \approx \pi b_i^2(z)u_i(z). \tag{2.3}$$

C_b represents the volume fraction of the plume cross-section occupied by droplets. Experimental data indicate that, away from the plume source, $C_b(z) \ll 1$ [43]. The average inner plume velocity, u_i, is defined as positive for a rising plume. b_i is the nominal plume radius.

The momentum flux of the inner plume (including the droplets) is approximated as

$$M_i(z) = \xi[1 - C(z)]\rho_i(z)\pi bi^2(z)u_i(z)^2 + C(z)\rho_b(z)b_i^2(z)[u_i(z) + u_b(z)]^2 \qquad (2.4)$$

where ξ, an amplification term defined in Milgram [43], accounts for the fact that use of the mean velocity u_i in (2.4) implicitly ignores turbulent momentum transport. Because $C_b \ll 1$, and $u_b = O(u_i)$, the momentum associated with the droplets themselves may be ignored, so the previous equation reduces to

$$M_i(z) \approx \xi\rho_i(z)\pi b_i^2(z)u_i(z)^2 = \xi Q_i(z)\rho_i(z)u_i(z). \qquad (2.5)$$

Most previous integral models for either single- or two-phase plumes are based on the conservation of volume, momentum, and buoyancy fluxes [9, 42, 49]. At least three state variables are required for a single-phase plume because there are at least three quantities that are governed by physical laws: conservation of mass (fluid), conservation of momentum, and conservation of the agent responsible for density differences in incompressible flow (e.g. salinity or temperature differences). So tracking volume, momentum, and buoyancy fluxes is the integral model equivalent to the Navier-Stokes equations coupled with a mass transport equation.

Choosing to track volume and buoyancy flux, rather than fluxes of fluid mass and stratifying agent, results in state variables that are intuitive because a plume source may intuitively be characterized by initial volume, momentum, and buoyancy flux. Furthermore, it is less cumbersome to define governing equations for these three integrated fluxes rather than another appropriate set of variables, such as plume width, mean centerline velocity, and density difference. Tracking buoyancy flux is also convenient because it is usually sufficiently accurate to model fluid density as a linear function of the concentration of the stratifying agent. It is also useful for formulating dimensional scaling arguments.

The alternative to using buoyancy flux is to track the flux of each individual stratifying agent. This approach is much less useful for analytical purposes, but is more appropriate for numerical models. This is especially true in the current work, where water density is affected not only by the mixing of ambient fluid from different heights in a stratified environment, but also because of the density effects of dissolved CO_2. Although it is still possible to formulate a model in terms of buoyancy flux, it is more straightforward to track the stratifying agents and then determine the fluid density with an appropriate equation of state. This approach is similar to that of Wüest [69].

The quantities that must then be tracked are the fluxes of salt, heat, and dissolved bubble material (e.g. dissolved CO_2). The salinity flux, $S_i(z)$, is defined as

$$S_i(z) = Q_i(z)s_i(z), \tag{2.6}$$

where $s_i(z)$ is the salinity of the inner plume. Salinity is assumed to be a conserved quantity. The heat energy flux of the inner plume is expressed as

$$J_i(z) = Q_i(z)\rho_{ref}c_pT_i(z), \tag{2.7}$$

where c_p is the heat capacity of the fluid, assumed to be constant, and T_i is the temperature of the inner plume in degrees Celsius. Note that the heat energy flux is expressed as a value relative to an arbitrary datum of seawater at 0 degrees C. This expression is defined in terms of ρ_{ref} rather than ρ_i for reasons explained shortly. The mass flux of dissolved droplet material is defined similarly, as

$$C_i(z) = Q_i(z)c_i(z), \tag{2.8}$$

where c_i is the concentration of dissolved droplet material.

The state variables for the outer plume are nearly identical. The primary difference is that, because the outer plume is assumed to be annular, the volume flux of the outer plume is defined as

$$Q_o(z) = \pi(b_o^2 - b_i^2)u_o, \tag{2.9}$$

where u_o, the characteristic velocity of the outer plume, has a sign opposite that of u_i. b_o is the radius of the outer plume. If $u_i > 0$, the inner plume flux quantities are all positive, and the outer plume fluxes (with the exception of momentum flux) are negative. They are:

$$\begin{aligned} M_o(z) &= \xi Q_o(z)\rho_o(z)u_o(z), && (2.10) \\ S_o(z) &= Q_o(z)s_o(z), && (2.11) \\ J_o(z) &= Q_o(z)\rho_{ref}c_pT_o(z), && (2.12) \\ C_o(z) &= Q_o(z)c_o(z) && (2.13) \end{aligned}$$

Although buoyancy flux is not used as a state variable in this model, it is still of interest for analysis. The buoyancy fluxes of the inner and outer plumes, respectively, may be defined as

$$\begin{aligned} B_i &= Q_i(z)g\frac{\rho_i(z)-\rho_a(z)}{\rho_{ref}}, &(2.14)\\ B_o &= Q_o(z)g\frac{\rho_o(z)-\rho_a(z)}{\rho_{ref}}. &(2.15) \end{aligned}$$

Properties such as characteristic plume width, velocity, and density difference (with respect to the ambient) may be deduced from the state variables:

$$\begin{aligned} &c_i = \tfrac{C_i}{Q_i}, && c_o = \tfrac{C_o}{Q_o},\\ &s_i = \tfrac{S_i}{Q_i}, && s_o = \tfrac{S_o}{Q_o},\\ &T_i = \tfrac{J_i}{Q_i c_p \rho_{ref}}, && T_o = \tfrac{J_o}{Q_o c_p \rho_{ref}},\\ &\rho_i = f(s_i, T_i, P(z)), && \rho_o = f(s_o, T_o, P(z)), \qquad (2.16)\\ &\Delta\rho_i = \rho_i - \rho_a, && \Delta\rho_o = \rho_o - \rho_a,\\ &u_i = \tfrac{M_i}{\xi Q_i \rho_i}, && u_o = \tfrac{M_o}{\xi Q_o \rho_o},\\ &b_i = \left(\tfrac{Q_i}{\pi u_i(1-C_b)}\right)^{\frac{1}{2}}, && b_o = \left(\tfrac{Q_i}{\pi u_i} + b_i^2\right)^{\frac{1}{2}}. \end{aligned}$$

The heat energy flux is expressed relative to a reference density. As the fluid density is a function of the fluid temperature, this approximation avoids the need to solve for density and temperature iteratively. P is the *in-situ* pressure.

With the state variables and dependent variables defined, it is possible to set up a framework for the model's governing equations. These equations describe how the state variables change along the plume axis due to the primary physical processes controlling the plume. In this section, the governing equations are expressed in terms of quantities representing sub-models of these processes; the details of these sub-models are described in Section 2.3.

First, the droplet mass flux, W_b, changes due to dissolution of the droplets. Thus, the governing equation for W_b is of the form

$$\frac{dW_b}{dz} = f(d_b, u_i, u_b, \ldots). \tag{2.17}$$

and is discussed further in Section 2.3.3 (see Equation 2.51). The inner plume volume flux changes due to turbulent entrainment and peeling. The model treats the two as distinct processes which may be superimposed. The governing equation is

$$\frac{dQ_i}{dz} = E_i + E_o + E_p, \tag{2.18}$$

where E_i is the rate at which volume flux is entrained to the inner plume from either the outer plume, if present, or the ambient fluid. E_i thus has units of $[m^2/s]$, or velocity times a distance. E_o represents the entrainment of fluid from the inner plume to the outer plume, and E_p represents the rate at which fluid leaves the inner plume due to buoyant detrainment. E_o and E_p are both negative. By continuity, the governing equation for the volume flux of the outer plume is

$$\frac{dQ_o}{dz} = E_i + E_o + E_p + E_a, \tag{2.19}$$

where E_a is the rate of entrainment from the ambient fluid into the outer plume. The signs of this equation and Equation 2.18 are consistent because Q_i and Q_o have opposite signs by definition. The nature of E_i, E_o, and E_a is discussed in Section 2.3.7; E_p is defined in Section 2.3.8.

Just as the fluxes of stratifying agents are closely related to the volume flux, so are the governing equations for these variables. For the inner plume, they are defined as:

$$\frac{dC_i}{dz} = E_i c_o + E_o c_i + E_p c_i, \tag{2.20}$$

$$\frac{dS_i}{dz} = E_i s_o + E_o s_i + E_p s_i, \tag{2.21}$$

$$\frac{dJ_i}{dz} = c_p \rho_{ref}(E_i T_o + E_o T_i + E_p T_i) + \frac{dW_b}{dz} \Delta H_{sol}. \tag{2.22}$$

The last term of the the equation for J_i accounts for the heat released by the dissolution of CO_2, as discussed in Section 2.3.1.

Similarly, for the outer plume,

$$\frac{dC_o}{dz} = E_i c_o + E_o c_i + E_p c_i + E_a c_a, \tag{2.23}$$

$$\frac{dS_o}{dz} = E_i s_o + E_o s_i + E_p s_i + E_a s_a, \tag{2.24}$$

$$\frac{dJ_o}{dz} = c_p \rho_{ref}(E_i T_o + E_o T_i + E_p T_i + E_a T_a). \tag{2.25}$$

These equations spring from the implicit assumption that the mechanisms of mass and heat transfer are primarily the advection of water parcels between the inner and outer plumes, and that the turbulent Schmidt and Prandtl numbers are $O(1)$.

Momentum is also transferred due to turbulent entrainment. Entrainment of a water parcel moving with a nonzero velocity implies a change in momentum flux, as does loss of a water parcel due either to entrainment or peeling.

The dominant factor controlling momentum flux, however, is buoyancy. At a given height, the fluid in the inner plume will experience an upward force transmitted from the droplets by drag forces, and a downward force due to their own negative buoyancy with respect to the ambient environment. Fluid in the outer plume will also experience a buoyant force due to density differences with respect to the ambient. Thus, the governing equations for momentum flux for the inner and outer plumes are

$$\frac{dM_i}{dz} = \hat{B}_b - \hat{B}_i + E_i \rho_o u_o + E_o \rho_i u_i + E_p \rho_i u_i, \tag{2.26}$$

$$\frac{dM_o}{dz} = \hat{B}_o + E_i \rho_o u_o + E_o \rho_i u_i + E_p \rho_i u_i + E_a \rho_a u_a, \tag{2.27}$$

where $\hat{B}_b$, $\hat{B}_i$, and $\hat{B}_o$ represent the buoyant forces associated with the droplets, inner plume fluid, and outer plume fluid. These terms are discussed in Section 2.3.6.

2.3 Processes and Properties

In this section, the submodels for the entities and processes of multiphase plumes are described. These submodels describe physical and chemical properties of the plume phases (in this study, CO_2 and seawater), behavior of bubbles, droplets and particles, buoyant forces, turbulent entrainment, and buoyant detrainment.

2.3.1 Phase Properties

Any fluid mechanics model relies on knowledge of the physical properties of the fluids involved. In the current context, the fluids involved are seawater and either carbon dioxide or air. The properties of these fluids are determined primarily by the ambient temperature, pressure, and salinity of the seawater.

The model has been designed to allow use of arbitrary (i.e. real) ambient stratification profiles. Supplied with a minimum of depth, ambient temperature, and either salinity or seawater density (from which salinity may be calculated), the model constructs a table of seawater and dispersed phase properties. Ambient properties for depths in between the specified depths are obtained by linear interpolation.

Seawater

The model depends on the knowledge of several properties of ocean water at any given depth. These include the ambient salinity, temperature, and pressure, and properties which are functions of these three quantities. The most important dependent property is in-situ density, which may be calculated using the UNESCO equation of state for seawater, detailed in Appendix A [27]. Another pertinent property is viscosity, which may be calculated by the equation

$$\mu = 2.6 \times 10^{-6} e^{1750/T} \tag{2.28}$$

where T is the temperature in Kelvins [40].

The stratification used for the analyses in the present work were obtained during a research cruise conducted in August 1999. The cruise focused on the waters off of Keahole Point on the island of Hawaii, which is a likely site for the planned field experiment. Over thirty CTD (conductivity, temperature, depth) casts were taken in this area over a three day period [1]. The calculated density profile based on one of the casts is shown in Figure 2-2. This data was very slightly modified in order to obtain a linear density gradient from 600 to 900 meters depth. The buoyancy frequency over this depth is $N = 3.2 \times 10^{-3}\ s$.

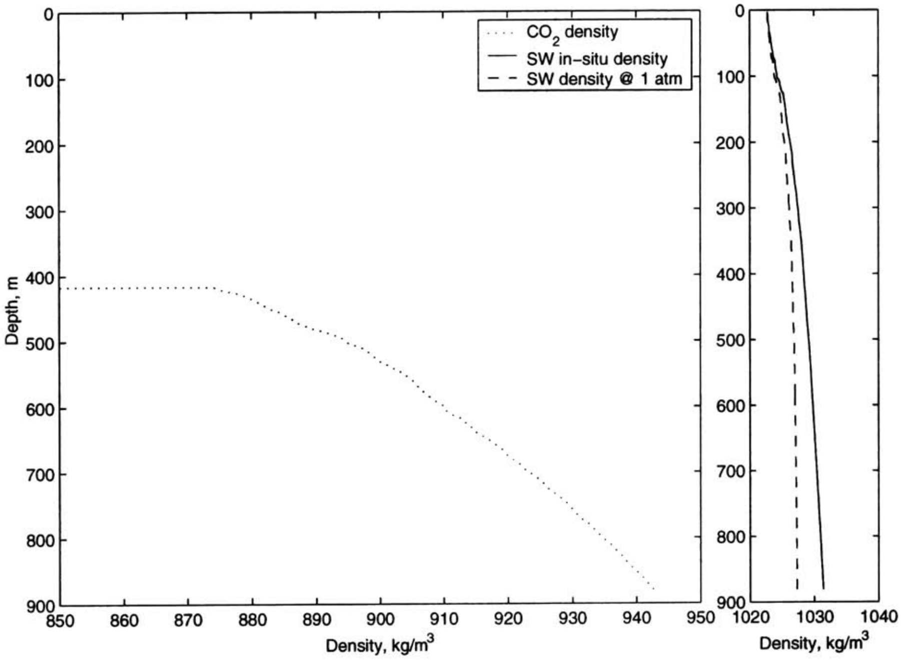

Figure 2-2: Stratification profile near Keahole Point. The density profiles of CO_2, on the left, and seawater, on the right, are calculated from temperature, salinity, and pressure measurements. CO_2 flashes to vapor at about 400 meters. Source: Arild Sundfjord, NIVA.

Carbon Dioxide

There are several physical and chemical properties of the droplet material which are relevant to the current work. These include density, solubility in seawater, molar volume in seawater, surface tension, and the rate of diffusion in seawater.

The density of CO_2 is calculated from the IUPAC equation of state [8] which explicitly calculates pressure given CO_2 density and temperature (see Appendix B. Density as a function of pressure and temperature is calculated iteratively by Newton's method [16]. Fugacity is also calculated from the equation of state.

The solubility of CO_2 in seawater may determined by an empirical relationship [63]. The solubility of CO_2 in synthetic seawater, expressed as a mole fraction, is

$$x_{CO_2} = \frac{f_{CO_2}}{K_H} e^{\alpha S} \tag{2.29}$$

where f_{CO_2} is the fugacity of CO_2, K_H is the Henry's Law coefficient for the CO_2-seawater system, α represents a salting-out coefficient, and S is the seawater salinity in psu. This expression is Henry's Law, modified by the Setchenow equation. Teng and Yamasaki [63] found empirical values for K_H and α as a function of temperature and pressure:

$$\begin{aligned} K_H &= a + bP + cP^2, \\ a &= 5.20 \times 10^3 - 3.92 \times 10^1 T + 7.5 \times 10^{-2} T^2, \\ b &= -1.03 \times 10^2 + 7.08 \times 10^{-1} T - 1.20 \times 10^{-3} T^2, \\ c &= 2.2 \times 10^{-2}, \end{aligned} \tag{2.30}$$

$$\alpha = 5.43 \times 10^{-1} - 3.54 \times 10^{-3} + 5.69 \times 10^{-6} T^2,$$

where K_H has units of MPa, as does the ambient pressure, P. Temperature, T, is on the Kelvin scale. This relationship agrees with experimental data within 3 percent, on average.

One critical factor affecting the behavior of a CO_2 droplet plume is the fact that the density of seawater changes due to the concentration of dissolved CO_2. Weiss [67] estimated that the specific volume of CO_2 in water was 32.3 ± 0.5 cm^3/mol, or 7.34×10^{-4} m^3/kg, and did not vary significantly with temperature or pressure. Ohsumi et al. [51] reported density measurements taken at 276 K and 343 atm, with CO_2 concentrations ranging from 4.4 to 15.4 kg/m^3. The molar volume of CO_2 was calculated to be 31.0 ± 0.9 cm^3/mol, or 7.05×10^{-4} m^3/kg. Alendal and Drange [6] assumed a constant specific volume of 34 cm^3/mol (7.7×10^{-4} m^3/kg), which is consistent with the values obtained by Enns et al. [23]. This model assumes the specific volume to be 7.05×10^{-4} m^3/kg.

The change in seawater density due to dissolved CO_2 concentration, known as the solute density effect, is

$$\delta\rho = (1.0 - \bar{V}\rho_{ref})[CO_2] \tag{2.31}$$

where $\bar{V}$ is the specific volume $[m^3/kg]$ and the concentration of dissolved CO_2 has units of kg/m^3.

A countering effect is the release of heat due to CO_2 dissolution. The height of solution for CO_2 in water is $\Delta H_{sol} = 25$ kJ/mol $= 568$ kJ/kg [40].

The diffusion coefficient for CO_2 in pure water changes slightly with depth. This work uses the relation

$$D = \frac{D_0 \mu_0 T}{T_0 \mu} = 3.6671 \times 10^{-6} \frac{T}{\mu} D_0 \tag{2.32}$$

where $D_0 = 1.94 \times 10^{-5}\ cm^2/s$, T is in Kelvins, and μ is in kg/ms [7]; the "0" subscript refers to values at standard temperature and pressure. The surface tension is nearly constant over the range of interest: $\sigma = 7.1 \times 10^{-2} N/m$.

Air

The model can also simulate air bubbles instead of CO_2 droplets. The purpose of including this option is to compare the model results with other air-bubble plume studies. Because air-bubble plumes are generally deployed in relatively shallow environments, the density of the air is modeled as an ideal gas:

$$\rho_{air} = \frac{M_{air} P}{RT} \tag{2.33}$$

where M_{air}, the effective molecular weight of air, is 29.0 g/mol, and R is the ideal gas constant.

2.3.2 Carbonate Chemistry

The inorganic chemistry of dissolved CO_2 is central to the issue of ocean sequestration and to the global carbon cycle in general. The primary reactions of interest are [45]:

$$\begin{aligned} CO_2 + H_2O &\rightleftharpoons H_2CO_3 \\ CO_2 + H_2O &\rightleftharpoons HCO_3^- + H^+ \end{aligned}$$

$$
\begin{aligned}
H_2CO_3 &\rightleftharpoons HCO_3^- + H^+ \\
HCO_3^- &\rightleftharpoons CO_3^{2-} + H^+
\end{aligned}
$$

Because of the importance of these reactions in chemical oceanography, as well as many other fields, the equilibrium constants for these equations are known quite accurately as a function of temperature and salinity [21, 54]. Knowledge of these constants and the background ambient inorganic carbon and alkalinity concentrations allows determination of the change in equilibrium pH due to an increase in the total amount of dissolved carbon. The definitions of DIC and carbon alkalinity ($C - Alk$) are [45]:

$$DIC = [H_2CO_3^*] + [H_CO_3^-] + [CO_3^{2-}] \tag{2.34}$$

$$C - Alk = -[H^+] + [OH^-] + [HCO_3^-] + 2[CO_3^{2-}] \tag{2.35}$$

where $H_2CO_3^*$ represents the sum of hydrated (H_2CO_3) and unhydrated (CO_2) dissolved carbon dioxide. Carbon alkalinity is the dominant source of total alkalinity. The relationship between additional DIC and pH is shown in Figure 2-3.

The kinetics of CO_2 dissociation in isolation have also been rigorously studied [45]. While the kinetics of these reactions by themselves should be quick, Zeebe et al. suggested [71] that the carbonate chemistry couples with other chemical systems (e.g. $H_2O, B(OH)_3$) in such a way that the time constant of the CO_2 dissociation reaction may be much larger than the time constants of any single reaction in the system. Zeebe et al. estimate that the relaxation time for CO_2 equilibrium at the ocean surface (25 degrees C) is about 16 seconds. While relatively quick, this time-scale approaches that of some plume processes.

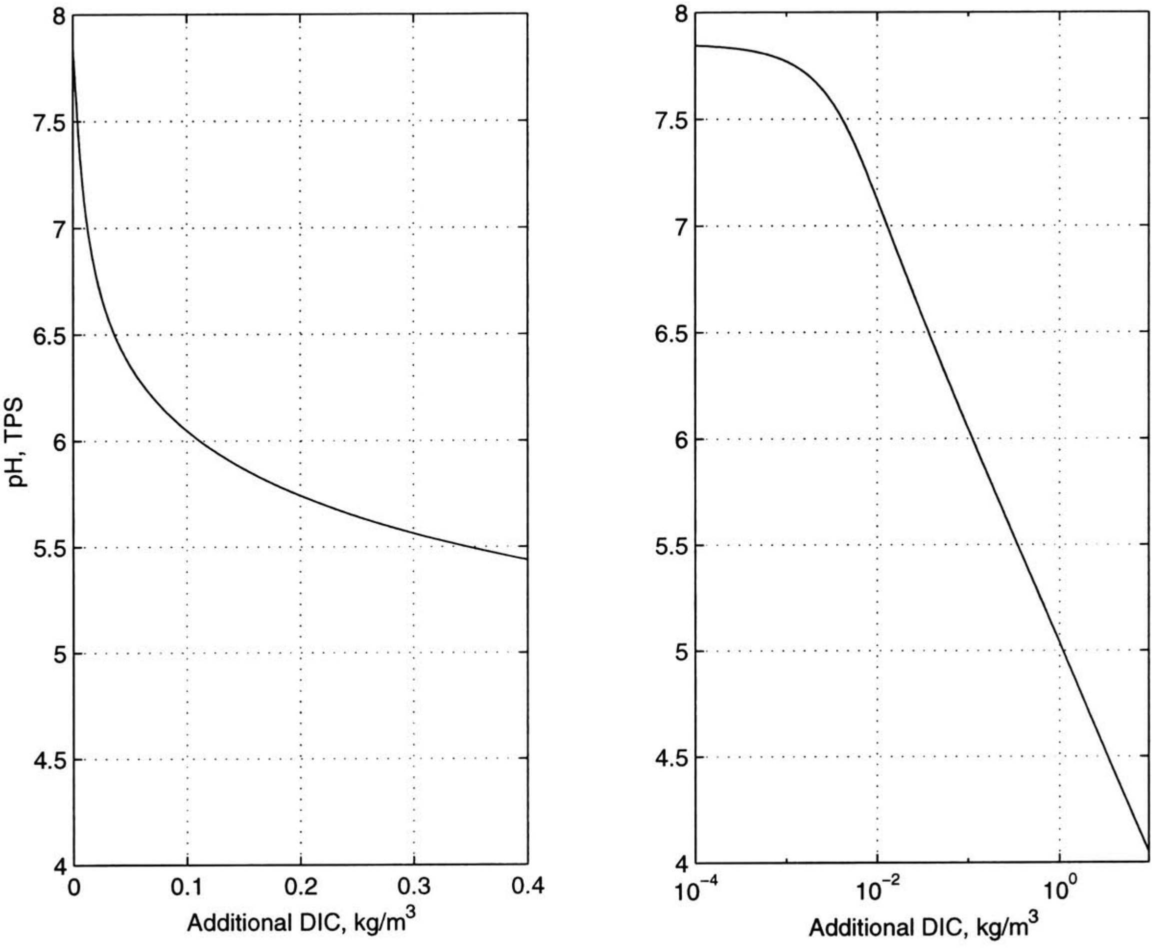

Figure 2-3: CO_2 Concentration vs. pH. pH is expressed in terms of the total proton scale at the *in-situ* temperature. The amount of added DIC is shown on both a linear and logarithmic scale. Equilibrium constants are based on the DOE carbon dioxide handbook [21]. The ambient DIC and alkalinity values off of Keahole Point at 800 meters are 2.32×10^3 and 2.38×10^3 $\mu mol/kg$, respectively [44]. A CO_2 concentration of 1 kg/m^3 corresponds to 22.7×10^3 $\mu mol/kg$.

2.3.3 Bubble Dynamics

Plume behavior is primarily controlled by the amount of buoyant force acting on the CO_2 droplets. As the droplets will rise in the plume at an approximately constant velocity relative to the plume water, the buoyant forcing is essentially balanced by drag force on the droplets. As the droplets move, the drag forces do work on the ambient liquid, so the end result is that the buoyant force of the droplets is transferred to the water in the plume.

Of the many factors that determine the effective buoyant force of the buoyant droplets, two, slip velocity and dissolution rate, are determined primarily by the characteristics of the CO_2 droplets themselves. Droplet behavior is determined by the size and shape of the droplets as well as the material properties of CO_2 and seawater.

Dimensionless expressions for slip velocity and dissolution rate are the Reynolds number Re and the Sherwood number Sh, respectively. These are defined as:

$$Re = \frac{\rho d_b u_b}{\mu} \tag{2.36}$$

$$Sh = \frac{K d_b}{D} \tag{2.37}$$

where d_b is the effective bubble diameter, defined such that the bubble volume $v_b = \frac{1}{6}\pi d_b^3$. ρ and μ are the density and viscosity of CO_2, D is the diffusivity of the CO_2-seawater system, and K is the mass transfer coefficient [20]. These dimensionless quantities are useful because they can be predicted from other dimensionless numbers which describe the physical properties of the droplet.

There are several pertinent dimensionless numbers describing droplet characteristics.

These include the Morton number M, the Eötvös number Eo, the Schmidt number Sc, the Peclet number Pe, the viscosity ratio κ and the density ratio γ. These numbers are defined as:

$$\begin{aligned} M &= \tfrac{g\mu^4\Delta\rho}{\rho^2\sigma^3}, & Eo &= \tfrac{g\Delta\rho d_b^2}{\sigma}, \\ Pe &= \tfrac{u_b d_b}{D}, & Sc &= \tfrac{\mu}{\rho D}, \\ \kappa &= \tfrac{\mu_b}{\mu}, & \gamma &= \tfrac{\rho_b}{\rho}. \end{aligned} \tag{2.38}$$

Quantities with the b subscript refer to CO_2 properties, while quantities without subscripts refer either to seawater or the CO_2-seawater system. Another dimensionless number commonly used, the Weber number We, can be expressed in terms of those already introduced:

$$We = \frac{\rho u_b^2 d_b}{\sigma} = \left(\frac{MRe^4}{Eo}\right)^{\frac{1}{2}}. \tag{2.39}$$

Bubble and droplet behavior can be grouped into different regimes, based on values of these dimensionless numbers, as illustrated graphically in Figure 2-4. At a depth of 800 meters, the values of M and Eo for a 1 cm diameter droplet are $M \approx 1 \times 10^{-13}$ and $Eo \approx 1.3$. For a 1 mm diameter droplet, $Eo \approx 1.3 \times 10^{-2}$. According to Clift, the droplets are in the wobbling and spherical regimes, respectively.

Droplet behavior is also affected by additional chemical factors. The presence of surfactants which collect on the droplet surface tends to interfere with internal droplet circulation, causing the droplet to behave more like a rigid particle. Apart from certain experimental setups in which the bulk fluid is highly purified, surfactant effects are almost always significant [20].

Bubble formation behavior is also affected by the presence of dissolved salts. In fresh

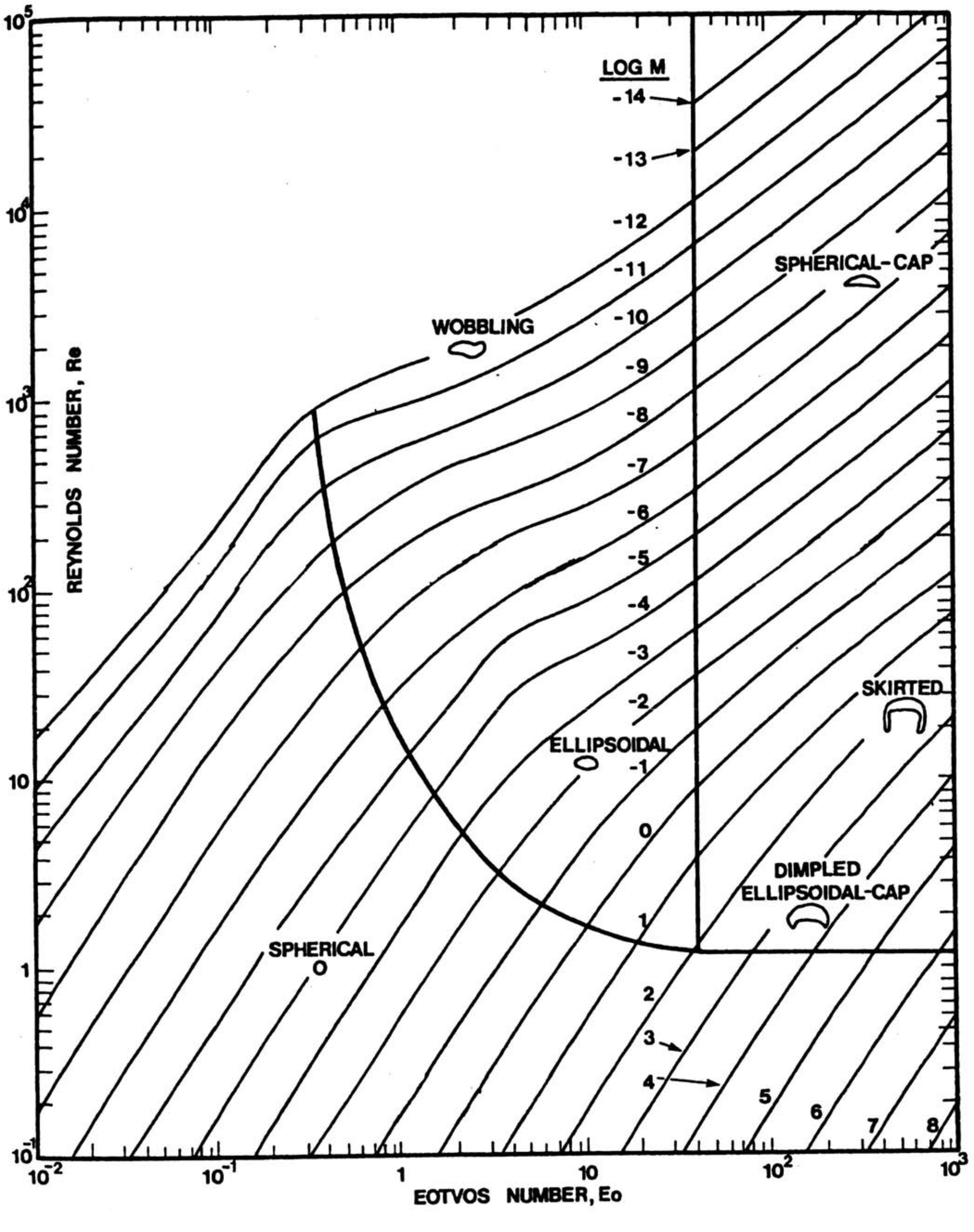

Figure 2-4: Bubble and droplet shape regimes. Source: Clift [20].

water, the size of bubbles emanating from a diffuser is primarily affected by the gas flow rate, and is less effected by the geometry of the diffuser [20, 35, 43, 60]. In seawater, however, small bubbles are more stable, and bubble size can be controlled to some degree by diffuser shape [12].

There is another chemical factor of concern in the case of deep-ocean CO_2 sequestration. At the high pressures and low temperatures characteristic of a deep-ocean environment, carbon dioxide and water tend to form a clathrate hydrate, which is crystal-like phase in which water molecules form a lattice with gaps filled by CO_2 molecules [31]. Hydrates have been observed to form on the surface of CO_2 droplets experimentally [31, 47] and in the field [14]. The phase diagram for the CO_2-H_2O system is shown in Figure 2-5. The formation of hydrates is significant because their presence has been observed to significantly reduce the rate of mass transfer [31, 47, 66].

Slip velocity

There are many correlations available for predicting a droplet's slip velocity. The challenge is to predict its drag coefficient C_d, defined by the equation

$$F = C_d \rho u_b^2, \tag{2.40}$$

where F is the mean drag force acting on the droplet. The primary factors determining C_D are the dimensionless numbers just described, the behavior of the droplet surface (i.e. mobile or fixed), and the ambient turbulence. The correlations given in Clift are for single bubbles, droplets and particles translating in a still medium— it is reasonable to expect

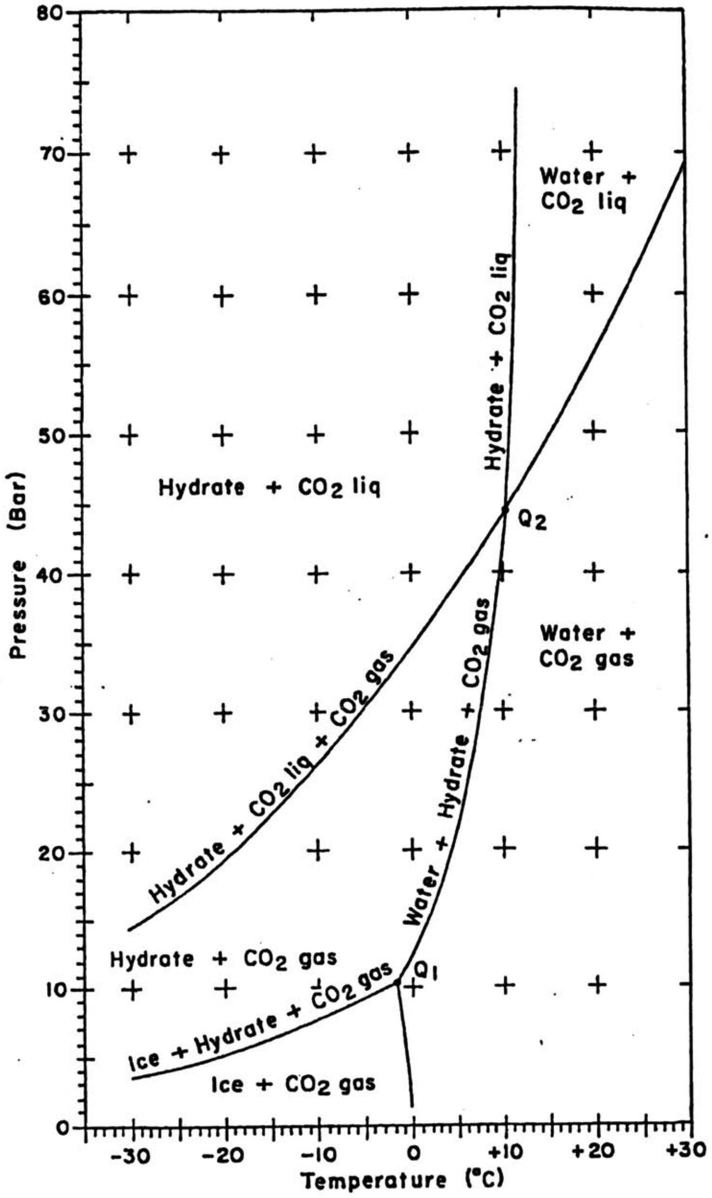

Figure 2-5: CO_2-H_2O phase diagram. Source: North et al. [50].

that the presence of neighboring bubbles and a turbulent flow field could alter bubble slip velocity. However, there is little experimental work concerning these effects, and current direct numerical simulations of bubble swarms are limited to just a few bubbles rising at Reynolds numbers in the range of 20 to 30 [24]. As proven correlations for effective slip velocities of droplets in a swarm are not readily available, one suitable course of action is to examine the sensitivity of plume behavior to slip velocity (Section 4.2.1).

Clift offers several correlations for bubbles and droplets based on the flow regime. For the case where $M < 10^{-3}$, $Eo < 40$, and $Re > 0.1$, the empirical correlation for the slip velocity of bubbles and drops is:

$$\begin{aligned} H &= \frac{4}{3} Eo\, M^{-0.149} \left(\frac{\mu}{\mu_w}\right)^{-0.14}, & (2.41) \\ J &= 0.94 H^{0.757}, \ (2 < H \leq 59.3) & (2.42) \\ J &= 3.42 H^{0.441}, \ (H > 59.3), & (2.43) \\ Re &= M^{-0.149}(J - 0.857), & (2.44) \end{aligned}$$

where $\mu_w = 9 \times 10^{-4}\ kg/ms$.

Algebraic manipulation reveals that slip velocity scales with $(d_b)^{0.514}$ when Equation 2.42 is valid, and otherwise scales with $(d_b)^{-0.118}$. For the case of a CO_2 droplet at 800 meters depth, the transition radius is about 6 mm. One practical advantage of this correlation for a numerical model is that is does not require an iterative procedure, which is often the case when a correlation predicts C_d as a function of Re.

Clift presents a different correlation for solid, spherical particles, based on the Nusselt number N_D,

$$N_D = C_D Re_T^2 = \frac{4}{3}\frac{\rho \Delta \rho g d^3}{\mu^2}. \tag{2.45}$$

In the range $580 < N_D \leq 1.55 \times 10^7$, $12.2 < Re \leq 6.35 \times 10^3$,

$$\log_{10} Re = -1.81381 + 1.34671W - 0.12427W^2 + 0.006344W^3 \tag{2.46}$$

where

$$W = \log_{10} N_D. \tag{2.47}$$

For higher Nusselt and Reynolds numbers, $1.55 \times 10^7 < N_D \leq 5 \times 10^{10}$ and $6.35 \times 10^3 < Re \leq 3 \times 10^5$,

$$\log_{10} Re = 5.33283 - 1.21728W + 0.19007W^2 - 0.007005W^3. \tag{2.48}$$

Figure 2-6 shows the predicted slip velocities for a CO_2 droplet at 800 meters as a function of bubble diameter for both the fluid and solid particle regimes. Over the size range of interest (the reasons for focusing on droplets with a diameter of $O(1\ cm)$ become apparent in Chapter 4), the predictions for the fluid and solid regimes are comparable.

Mass transfer

The rate of mass transfer, or dissolution, of CO_2 from a droplet to dissolved form can be described by the empirical Ranz-Marshall equation:

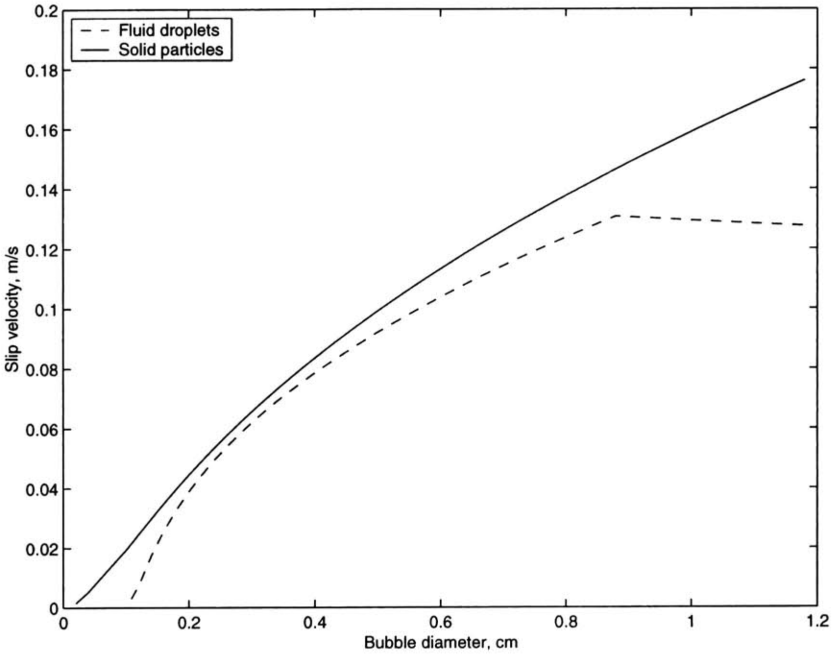

Figure 2-6: Slip velocity vs. effective droplet diameter for a CO_2 droplet at 800 meters.

$$\frac{dm_b}{dt} = -\pi d_b^2 K(C_s - c_i) \tag{2.49}$$

where $K[L/T]$ is a mass transfer coefficient, $C_s[M/L^3]$ is the surface concentration of CO_2, which is equivalent to the solubility of CO_2, and $c_i[M/L^3]$ is, as previously noted, the concentration of dissolved CO_2 in the vicinity of the bubble.

Substituting $m_b = v_b\rho_b = \frac{1}{6}\pi d_b^3$ into Equation 2.49 and assuming ρ_b to be constant yields

$$\frac{dd_b}{dt} = 2K\frac{(C_s - c_i)}{\rho_b} \tag{2.50}$$

Thus, the rate of droplet shrinkage (the most direct experimental observation) is affected by two components: the mass transfer coefficient and the solubility of CO_2 (assuming that

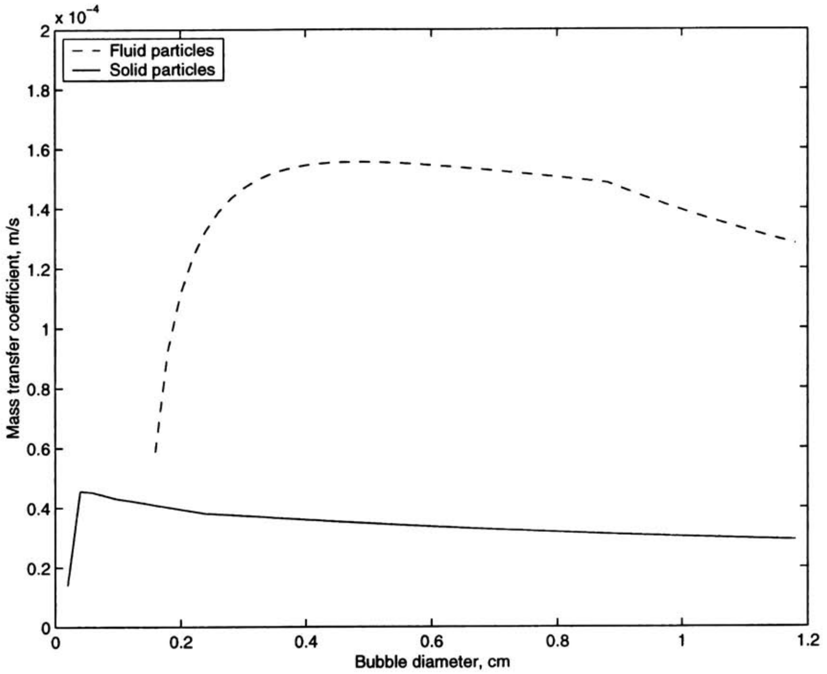

Figure 2-7: Mass transfer vs. effective droplet diameter for a CO_2 droplet at 800 meters. The plotted mass transfer rate for a fluid droplet does not apply for Reynolds numbers of less than 100, which corresponds to a droplet diameter of 0.25 cm.

$c_i \ll C_s$).

Multiplying Equation 2.49 by the bubble number flux describes the rate of change of the mass flux of CO_2 in the dispersed phase. Also, in order to be consistent with the governing equations of the plume model, this differential equation should describe a change over distance rather than time. This is achieved by dividing Equation 2.49 equation by the nominal bubble velocity, $(u_i + u_b)$:

$$\frac{dW_b}{dz} = -N_b \pi d_b^2 \frac{K(C_s - c_i)}{u_i + u_b}. \tag{2.51}$$

What remains, of course, is determination of K, which can be correlated with droplet properties. The correlations for K for a rigid particle, given by Clift [20], are:

$$\begin{aligned} Sh &= 1 + 0.425 Re^{0.55} Sc^{1/3} \qquad (Re \geq 2000), \\ Sh &= 1 + 0.724 Re^{0.48} Sc^{1/3} \quad (100 \leq Re < 2000), \\ Sh &= 1 + (1 + 1/Pe)^{1/3} Re^{0.41} Sc^{1/3} \qquad (Re < 100). \end{aligned} \tag{2.52}$$

For a fluid particle, Clift offers the following correlation for moderate Reynolds numbers:

$$Sh = \frac{2}{\pi^{1/2}} \left[1 - \frac{1}{Re^{1/2}} \left(2.89 + 2.15 \kappa^{0.64} \right) \right]^{\frac{1}{2}} Pe^{\frac{1}{2}} \quad (Re > 100). \tag{2.53}$$

A comparison between Equations 2.52 and 2.53 is shown in Figure 2-7. The author does not expect the higher values for a fluid droplet to apply to the current situation both because of surfactant effects and hydrate formation. Therefore, the model adopts Equation 2.52 exclusively.

Of course, the effects of hydrate formation on mass transfer must also be considered. Because of both the recognition that hydrate formation significantly affects mass transfer rate, and the increasing interest in CO_2 ocean sequestration, research on this topic has been quite active recently [26, 30, 31, 32, 46, 47, 50, 62]. Unfortunately, there remains significant uncertainty regarding mass transfer rates: different investigators report that droplets coated with hydrate films dissolve at rates that are anywhere from two times [30] to over 100 times [66] slower than comparable droplets without hydrates.

One source of confusion arises from comparison of diameter shrinkage rates. Equation 2.50 shows that the rate of diameter reduction is proportional to the mass transfer coefficient, K. However, from Equations 2.52 and 2.36 it is clear that, to a first approximation, $K \sim (U/d)^{1/2}$. Therefore, it is necessary to correct for both flow speed as well as droplet size (and CO_2 solubility, which depends on temperature and pressure) in order to compare different experiments.

Perhaps the most reliable comparative experimental dataset at present is that of Hirai et al. [30]. In their experiments, these researchers measured the shrinkage rate of CO_2 droplets. The droplets were fixed by a wire support in a pressurized vessel. Ion-exchange water was pumped with a velocity of a few centimeters per second in order to simulate rising droplets. Both the flow velocity and the system temperature (which affects hydrate formation) were varied, the latter from 276 K to 286 K. Hydrates did not form on the droplets at the highest temperature. The results showed that the dissolution rate was strongly dependent on fluid velocity and the ambient temperature and pressure. The dissolution rate of a hydrate covered droplet at 278 K, which is a typical ambient temperature at 800 meters, was about half that of a droplet with no hydrate formation at 286 K.

Warzinski and Holder [66] measured the dissolution rate of CO_2 droplets in a stagnant seawater environment. In these experiments, a droplet with a hydrate shell at 275 K was observed to dissolve nearly three orders of magnitude slower than a droplet without a hydrate shell at 281 K. The rate of dissolution at 278 K was about one tenth that of the 281 K case. As these experiments did not involve moving droplets, they are less pertinent than the Hirai dataset. Yet these results serve as a clear signal that mass transfer rates can change significantly due to hydrates.

Measurement of the shrinkage rate allows estimation of the product of the terms on the right hand side of Equation 2.50, but not of the individual terms. Thus, it is unclear from experimental data alone how hydrate formation inhibits mass transfer. Mori and Mochizuki [47] argued that the different dissolution rates in the data of Hirai et al. could be explained by the decreased solubility of CO_2 in seawater in the presence of hydrates; the solubility decreases as temperature decreases.

Knowledge of both how and by how much hydrate formation reduces mass transfer is rather uncertain. In order to account for this uncertainty, without delving into the details of hydrate chemistry, the model allows the calculated mass transfer rate to be reduced by a factor of an arbitrary constant. In order to explore the range of possible mass transfer rates, this constant is varied from 1 to 20, where the former case corresponds to a droplet with no hydrate formation, and the latter corresponds to a slowly dissolving, hydrate covered droplet. The base case constant is 2, which roughly corresponds to the degree to which hydrates retarded the dissolution rate in the experiments of Hirai et al.

Bubble Spread

Previous investigators observed that the width of the bubble core, the region of flow actually containing bubbles, is sometimes smaller than the width of the upward flowing fluid. Previous models have modeled this behavior by defining a spreading ratio λ. For a bubble plume to be self-similar, λ must be constant. However, it is not clear that it is constant for real plumes. Furthermore, λ seems to vary significantly across experiments, ranging across values from 0.3 [22] to 1.0 [19], probably due to differences in bubble slip velocity and experimental artifacts such as plume wandering (because low frequency oscillations of the plume centerline lead to overestimates of the plume width [43]). The current model formulation uses $\lambda = 1$, because the presence of the descending outer plume should confine rising fluid to the plume core.

2.3.4 Momentum Amplification

Introduced in (2.5), ξ accounts for the fact that the plume flow is turbulent. The instantaneous vertical plume velocity may be decomposed into mean and turbulent quantities: $u = \overline{u} + u'$. Values of $\xi > 1$ account for the momentum flux associated with $\overline{u'u'}$.

Milgram [43] presented an analysis of the momentum amplification effect for an unstratified bubble plume. There, Milgram correlated ξ with a phase distribution number, N_P, that describes the coherency of the bubble column, such that

$$\xi(N_P) = 1.07 + \frac{D_1}{N_P^{D_2}} \tag{2.54}$$

where $N_P = L_V/L_D$ and $L_V = U_m^2/gC_b$. Correlation with the available data gave $D_1 = 977$ and $D_2 = 1.5$.

A slow stream of isolated bubbles has a low N_P, which gives a high value for ξ. Leitch and Baines [36] also report that turbulent momentum flux increases with decreasing airflow rate, though they found discrepancies between their data and (2.54). In the opposite limit, as $N_P \to \infty$, $\xi \to 1.07$, the value for a single-phase plume.

For simplicity, the current model assumes a constant value of ξ, but treats it as a parameter that can be varied across runs. Sensitivity to momentum amplification is explored in Section 4.2.

2.3.5 Initial Conditions

The model requires initial values for its state variables. The initial bubble mass flow rate, and thus the droplet buoyancy flux, is known. However, because the flow near the release is not well understood, quantities such as the initial plume volume and momentum fluxes cannot be calculated with great accuracy. Fortunately, plume behavior is quite insensitive to the initial volume and momentum fluxes, provided that they are small [39, 43]. Following Liro, the current model is initialized by assuming that the initial flow is approximately that of a pure plume, so that the initial volume and momentum fluxes are:

$$Q_i^{init} = \frac{6}{5}\left(\frac{9\pi^2\alpha_i^4 B_i z_0^5}{10}\right)^{\frac{1}{3}}, \tag{2.55}$$

$$M_i^{init} = \left(\frac{81\pi\alpha_i^2 B_i^2 z_0^2}{100}\right)^{\frac{1}{3}}\rho_i, \tag{2.56}$$

where z_0 is a small vertical distance, taken to be 10 times the diameter of the release orifice, which is a design variable.

2.3.6 Buoyancy

The momentum flux changes with distance according to the force applied to the fluid over that distance. Thus, the relevant buoyant forces should be expressed in terms of a unit height.

The buoyant force associated with the droplets, $\hat{B}_b$, in a control volume is

$$\hat{B}_b = g\pi b_i^2(z)C_b(z)\rho_b(z) = g\frac{Q_b(z)}{u_b(z)+u_i(z)}\Delta\rho_b(z). \tag{2.57}$$

The buoyant force associated with the inner plume fluid is

$$\hat{B}_i = g\pi b_i^2(z)(1 - C_b(z))\Delta\rho_i(z) \approx g\pi b_i^2(z)\Delta\rho_i(z). \tag{2.58}$$

The buoyant force associated with the outer plume is

$$\hat{B}_o = g\pi(b_o^2(z) - b_i^2(z))\Delta\rho_o(z). \tag{2.59}$$

The formulations of these forces are considered as parameterizations because they involve certain assumptions. In particular, it is assumed that viscous dissipation associated with the work that the droplets perform on the plume fluid is negligible, and that non-hydrostatic pressure deviations can be neglected.

2.3.7 Turbulent Entrainment

Formulation of an integral model for free flows such as jets or plumes depends on a closure scheme describing the rate of mixing across the nominal edge of the flow. The classic parameterization, introduced formally by Morton, Taylor and Turner [49] and known as the entrainment assumption, involves the assumption that the rate of entrainment velocity perpendicular to the direction of mean flow is proportional to the magnitude of the mean flow, so that

$$u_e = \alpha U_m, \tag{2.60}$$

where u_e is the entrainment velocity, α is the entrainment coefficient (it bears no relation to the salting-out coefficient discussed in Section 2.3.1), and U_m is the characteristic mean plume velocity. It has been rigorously demonstrated experimentally that α has a constant value for pure jets and a different constant value for pure plumes in an unstratified environment. It appears that this is so because the mechanism of turbulent entrainment is controlled by the engulfing behavior of the largest-scale turbulent eddies, which in turn scale with the velocity difference across the shear layer [65]. It is a consequence of the self-similarity of the flow.

For both pure jets and pure plumes, the velocity profile of the flow is near-Gaussian,

$$u(r) = U_m e^{-\left(\frac{r}{b_g}\right)^2}, \tag{2.61}$$

where b_g is the nominal radius of the flow. In this context of Gaussian profiles, $\alpha_{jet} = 0.054$, and $\alpha_{plume} = 0.083$ [65]. The entrainment volume flux, per unit height, is $2\pi b_g u_e$.

With a velocity profile given by Equation 2.61, integration shows that the volumetric flow rate of fluid $Q = \pi b_g^2 U_m$, and the momentum flux $M \approx \frac{1}{2}\pi b_g^2 U_m^2$. A top-hat profile with identical volume flux and momentum flux may be obtained if the nominal width $b_{th} = \sqrt{2} b_g$ and $u_{th} = U_m/2$. Top-hat entrainment coefficients which yield identical volume fluxes are thus $\alpha_{jet} = 0.054\sqrt{2} = 0.076$ and $\alpha_{plume} = 0.083\sqrt{2} = 0.12$.

There are two primary factors which affect the application of the entrainment assumption to the model under consideration. First, the effect of droplet motion in the plume alters the character of the inner plume turbulence. Second, the entrainment assumption needs to be extended for application to the interface between the counterflowing inner and outer plumes.

The entrainment coefficient varies for a bubble plume in an unstratified environment.

Milgram [43] developed an empirical correlation for α based on local plume conditions:

$$\alpha(F_B) = K\frac{F_B}{A + F_B} \tag{2.62}$$

where $K = 0.165$ and $A = 7.598$. F_B is a bubble Froude number, defined as

$$F_B = C_b^{2/5}\frac{L_M}{L_D} \tag{2.63}$$

where $L_M = (Q_b^2/gC_b^2)^{1/5}$ and $L_D = (\sigma_b/g(\rho_w - \rho_b))^{1/2}/C_b^{1/3}$. Milgram suggested that L_M is a characteristic bubble mixing length, and L_D is a characteristic distance separating bubbles. He argued that an increase in the bubble Froude number enhances turbulent entrainment by increasing turbulence near the entrainment interface. The values for α which Milgram observed, which ranged from 0.037 to 0.165 (assuming Gaussian profiles), spans the range of values reported by other investigators [18, 60]. While it is worthwhile to note the dependence of α on local plume conditions, Milgram's correlation has not been incorporated directly into the current model.

The models of both McDougall [42] and Asaeda and Imberger [9] modeled entrainment between turbulent flows. McDougall reasoned that the mixing between the plumes, and between the outer plume and the ambient, could be parameterized with the entrainment assumption, so that the entrainment fluxes become

$$\begin{aligned} E_i &= 2\pi b_i \alpha_i (u_i - u_o), \\ E_o &= 2\pi b_i \alpha_o u_o, \end{aligned} \tag{2.64}$$

$$E_a = 2\pi b_o \alpha_a u_o,$$

These mixing assumptions are based in part on Morton [48], which applied the entrainment assumption to coaxial, coflowing single-phase jets. This particular application of the entrainment hypothesis has not been clearly verified by experiment. This set of entrainment equations is referred to as the *AI* entrainment method in Chapter 4.

McDougall found that, for his model to preserve an inner plume with slowly evolving radius and velocity, and thus volume flux, $2\alpha_i \simeq \alpha_o \simeq \alpha_a$. If the inner plume volume flux is nearly constant, this must also mean that, on average, $E_i = E_o$; these relationships indicate that $u_i \simeq 3u_o$. As the momentum flux from the outer to the inner plume is $E_i u_o$, and the momentum flux from the inner to the outer is $E_o u_i$, one may also show that the net momentum flux from the inner to the outer plume is approximately $2E_o u_o$. The net momentum flux must be in this direction, as this momentum flux is the only factor working to lift the fluid in the negatively buoyant outer plume.

The entrainment relationships of the Asaeda and Imberger model are identical to those of McDougall, except that in this case $u_o < 0$, so the entrainment fluxes (Equation 2.64) become

$$\begin{aligned} E_i &= 2\pi b_i \alpha_i (|u_i| + |u_o|), \\ E_o &= 2\pi b_i \alpha_o |u_o|, \\ E_a &= 2\pi b_o \alpha_a |u_o|. \end{aligned} \tag{2.65}$$

Asaeda and Imberger also found that the relationship $2\alpha_i \simeq \alpha_o \simeq \alpha_a$ produced the best fit of the model to their experimental data.

A formulation that is consistent with Abramovich's [2] observation that the spreading rate of a jet in a counterflow is the same as a jet in a quiescent environment is

$$\begin{aligned} E_i &= 2\pi b_i \alpha_i |u_i|, \\ E_o &= 2\pi b_i \alpha_o |u_o|, \\ E_a &= 2\pi b_o \alpha_a |u_o|. \end{aligned} \tag{2.66}$$

This entrainment model, labeled the *BC* model in Chapter 4, serves as an alternative to the *AI* model, Equation 2.65.

2.3.8 Buoyant Detrainment

As the mechanics of peeling are not well understood, previous investigators have chosen rough methods of simulating peeling in their numerical models. In the Liro model, peeling is assumed to occur at heights where the net buoyant force acting on the plume is zero. Reasoning that the slower, heavier plume fluid would peel at these locations, the Liro model assumes that, at the peeling locations, the plume loses one half of its volume flux, one half of its momentum flux, and the plume fluid's density difference with respect to the ambient fluid also decreases by one half [39].

McDougall [42], Asaeda and Imberger [9], and Schladow [57] all assume that peeling occurs when the momentum flux of the rising plume (the outer plume in the case of McDougall) approaches zero. This represents the highest point to which the plume fluid is capable of reaching, and thus represents an upper bound for the peeling event location.

Treating peeling as a discrete event is reasonable for plumes anticipated to exhibit Type 2 behavior, for which peeling events are widely separated, and the outer plume sections do not interact. However, such approaches are not appropriate for Type 3 plumes, or plumes where droplet dissolution and/or solute density effects are significant. The outer plume sections of such flows tend to merge, and the notion of discrete peeling events begins to lose meaning. The dynamics of such plumes often result in vertical peeling event spacings on the order of the plume width, which is inconsistent with the assumption of boundary-layer plume flow implicit in this model. A better approach would be to form a parameterization that calculates loss of fluid from the inner plume continuously due to local plume conditions, akin to the entrainment fluxes.

Several speculative parameterization were examined. One promising one is

$$E_p = \epsilon \left(\frac{u_b}{u_i} \right)^2 \left(\frac{B_i}{u_i^2} \right) \tag{2.67}$$

where ϵ is the peeling parameter. The rationale behind this expression is that it is dimensionally consistent and never fails for $\epsilon > 0$ to eject fluid from the inner plume before the momentum flux reaches zero. By tuning ϵ, it can also produce plume behavior that is consistent with experimental data (e.g. Socolofsky's [59] result that about 90 percent of the plume fluid is lost at a Type 2 peel).

2.4 Model Summary

2.4.1 State Variables

Inner Plume:

$$
\begin{aligned}
W_b &= \frac{1}{6}\pi d_b^3 N_b \rho_b \\
Q_i &= (1 - C_b)\pi b_i^2 u_i \\
M_i &= \xi Q_i \rho_i u_i \\
S_i &= Q_i s_i \\
J_i &= Q_i \rho_{ref} c_p T_i \\
C_i &= Q_i c_i
\end{aligned}
$$

Outer Plume:

$$
\begin{aligned}
Q_o &= \pi(b_o^2 - b_i^2)u_o \\
M_o &= \xi Q_o \rho_o u_o \\
S_o &= Q_o s_o \\
J_o &= Q_o \rho_{ref} c_p T_o \\
C_o &= Q_o c_o
\end{aligned}
$$

2.4.2 Dependent Variables

$$
\begin{array}{ll}
c_i = \frac{C_i}{Q_i} & c_o = \frac{C_o}{Q_o} \\
s_i = \frac{S_i}{Q_i} & s_o = \frac{S_o}{Q_o} \\
T_i = \frac{J_i}{Q_i c_p \rho_{ref}} & T_o = \frac{J_o}{Q_o c_p \rho_{ref}} \\
\rho_i = f(s_i, T_i, P(z)) & \rho_o = f(s_o, T_o, P(z)) \\
\Delta\rho_i = \rho_i - \rho_a & \Delta\rho_o = \rho_o - \rho_a \\
u_i = \frac{M_i}{\xi Q_i \rho_i} & u_o = \frac{M_o}{\xi Q_o \rho_o} \\
b_i = \left(\frac{Q_i}{\pi u_i (1 - C_b)}\right)^{\frac{1}{2}} & b_o = \left(\frac{Q_i}{\pi u_i} + b_i^2\right)^{\frac{1}{2}}
\end{array}
$$

2.4.3 Buoyancy Terms

Buoyancy Flux:

$$
\begin{aligned}
B_b &= g Q_b \frac{\Delta\rho_b}{\rho_{ref}} \\
B_i &= Q_i g \frac{\Delta\rho_i}{\rho_{ref}} \\
B_o &= Q_o g \frac{\Delta\rho_o}{\rho_{ref}}
\end{aligned}
$$

Buoyant Forces:

$$
\begin{aligned}
\hat{B}_b &= g \frac{Q_b}{u_b + u_i} \Delta\rho_b \\
\hat{B}_i &= g \frac{Q_i}{u_i} \Delta\rho_i \\
\hat{B}_o &= g \frac{Q_o}{u_o} \Delta\rho_o
\end{aligned}
$$

2.4.4 Governing Equations

Mixing:

$$\begin{aligned}
E_i &= 2\pi b_i \alpha_i (u_i - u_o) \ (AI) \\
E_i &= 2\pi b_i \alpha_i u_i \ (BC) \\
E_o &= 2\pi b_i \alpha_o u_o \\
E_a &= 2\pi b_o \alpha_a u_o \\
E_p &= \epsilon \left(\frac{u_b}{u_i}\right)^2 \left(\frac{B_i}{u_i^2}\right)
\end{aligned}$$

Inner Plume:

$$\begin{aligned}
\frac{dW_b}{dz} &= -N_b \pi d_b^2 \frac{K(C_s - c_i)}{u_i + u_b} \\
\frac{dQ_i}{dz} &= E_i + E_o + E_p \\
\frac{dM_i}{dz} &= \hat{B}_b - \hat{B}_i + E_i \rho_o u_o + E_o \rho_i u_i + E_p \rho_i u_i \\
\frac{dC_i}{dz} &= E_i c_o + E_o c_i + E_p c_i \\
\frac{dS_i}{dz} &= E_i s_o + E_o s_i + E_p s_i \\
\frac{dT_i}{dz} &= c_p \rho_{ref} (E_i T_o + E_o T_i + E_p T_i) + \frac{dW_b}{dz} \Delta H_{sol}
\end{aligned}$$

Outer Plume:

$$\begin{aligned}
\frac{dQ_o}{dz} &= E_i + E_o + E_p + E_a \\
\frac{dM_o}{dz} &= \hat{B}_o + E_i \rho_o u_o + E_o \rho_i u_i + E_p \rho_i u_i + E_a \rho_a u_a
\end{aligned}$$

$$
\begin{aligned}
\frac{dC_o}{dz} &= E_i c_o + E_o c_i + E_p c_i + E_a c_a \\
\frac{dS_o}{dz} &= E_i s_o + E_o s_i + E_p s_i + E_a s_a \\
\frac{dT_o}{dz} &= c_p \rho_{ref}(E_i T_o + E_o T_i + E_p T_i + E_a T_a)
\end{aligned}
$$

2.5 Model Solution

Solution of the governing equations yields a description of the steady-state properties of the modeled plume. The results in Chapter 4 are obtained by integrating the governing equations numerically. Although the model is posed in the form of an initial value problem, the decomposition of the plume structure into counterflowing inner and outer plumes requires that the equations be solved iteratively.

2.5.1 Numerical Integration Method

The conceptual model described in this section was implemented as a numerical model written in C++. The model features a GUI front-end, written in Tcl/Tk, that allows specification of several of the model design variables and parameters. This front-end also provides graphical output of the model's state variables as a model run progresses.

The discretized forms of the governing equations are solved with a fourth-order adaptive step Runge-Kutta algorithm [16]. An adaptive algorithm was used because the rate of change of the state variables varies over the length of the plume. Near the release point and near peeling events the state variable gradients become quite high, so the ability to decrease the step size in these regions is desirable.

2.5.2 Iteration Algorithm

Model solution begins with integration of the governing equations for the inner plume from the point of release to the point where the droplets disappear (when the mass flux of the droplets drops below a threshold, typically one percent of the initial mass flux) or the water surface is reached. On the first iteration, no outer plume segments exist, so the interactions with the environment are limited to entrainment of water into the inner plume and buoyant detrainment of water out of the plume. The model code also allows a ceiling depth to be specified— in the case of a CO_2 release, it is convenient to set the ceiling at about the depth where CO_2 flashes to vapor, as any plume reaching this height is ineffective at sequestering CO_2.

Once the inner plume integration is complete, the outer plume segments are integrated. Starting from the top, each outer plume section is initialized by stepping down the calculated inner plume and accumulating fluid lost from the inner plume. Once the outer plume is considered to be viable, the outer plume governing equations are integrated in the direction opposite that of the inner plume (usually downwards). At each step, properties of the inner plume pertinent to the outer plume governing equations (such as the inner plume width, velocity, rate of entrainment in both directions, etc.) are interpolated, and used in the outer plume integration (because of the adaptive step capability, the depths at which properties of the inner and outer plumes are calculated do not necessarily line up). The entrainment rates used in the outer plume governing equations are a weighted average of the rates calculated at that point, based on the updated outer plume properties, and those calculated during the ascent of the inner plume. The integration of each outer plume section continues until the momentum flux of the outer plume approaches zero, at which point it is assumed that the outer plume detaches from the inner plume and intrudes into the ambient environment (presumably rising slightly to reach the point of neutral buoyancy), or the outer plume disappears, having been fully re-entrained by the inner plume. Then, the next outer plume section is initialized and integrated until it reaches its terminus, and so on until the release point is reached. If a viable outer plume exists at this point, its governing equations are integrated past the release point (at which point the inner plume disappears) until the momentum flux approaches zero.

Integration of either the inner or outer plumes yields an array of data describing the spatial evolution of that portion of the plume. As the spacing of this array is not uniform in space because of the adaptive step algorithm, after each pass the property array is mapped onto a regularly spaced grid using linear interpolation. This procedure has two purposes: to produce tidy output files for analysis, and to allow superposition of outer plume profiles from multiple iterations.

The purpose of superimposing outer plume profiles is to promote model convergence. During development of this model, it was observed that, in many cases, profiles of plume properties would oscillate between two, three, or more states as the model iterations progressed. These oscillations did not always damp out as the number of iterations increased. Qualitatively, the model was behaving as an undamped dynamic system, initiated far enough from its equilibrium point to cause significant oscillation. In order to damp the model, after each integration of the outer plume segments, a composite outer plume profile is formed by adding weighted profiles from previous iterations. The number of previous iterations used in this averaging, N, is a model parameter, usually set to five. The weights assigned to each iteration are

$$w_i = \frac{2^{i-1}}{2^N - 1} \tag{2.68}$$

where i varies from 1 to N. w_1 is applied to the oldest iteration included in the averaging and w_N is applied to the most recent. This weighting was chosen because the weights sum to one for any N and the most recent iterations are much more heavily weighted.

The drawback of this technique is that it is a rather rough method of forcing convergence. It may be in some situations that the interactions between rising and falling fluid will result in an unstable system with significant oscillations. This is seen in Type 3 plumes and in negatively buoyant jets [64]. So it is possible that the model results stem from an artificially converged system.

The cycle of iterations is continued until the calculated plume profiles converge to the point where differences between iterations are very small. It typically takes 7-10 iterations to reach this state.

This method of model solution is different than that of the Asaeda and Imberger model. As mentioned in Section 2.1, that model is iterated one peel at a time. That approach is efficient when outer plume segments are known to be well separated, so the dynamics of each section of the plume are independent of the sections below it. For plumes where dissolution is significant, peeling events are less discrete, and outer plume segments often overlap lower peeling events. Thus, in such cases it is advantageous to integrate over the entire plume with each iteration.

Chapter 3

Experiments

A central assumption of this double-plume model is that the fluid in the immediate vicinity of the droplets, the inner plume, rises along with them. This assumption is clearly correct in the context of laboratory scale air bubble plumes in stratified environments [9, 42]. However, it is not so clear that it is valid in the case of plumes driven by dissolving CO_2 droplets. Because the positive buoyancy associated with the droplets decreases with height due to dissolution, and the negative buoyancy of the receiving water is enhanced by the dissolved CO_2, it is conceivable that the droplets would rise through fluid that is everywhere descending. A possible radial velocity profile for this situation is illustrated in Figure 3-1, along with the type of velocity profile that the current model assumes. The implications of the direction of fluid flow amidst the droplets is significant. If the fluid is rising, the droplets in the plume will tend to rise higher than a single, isolated droplet would. If the fluid is descending, the plume height would be smaller than the rise height of an isolated droplet. The height of the plume affects the depth at which the dissolved CO_2 is sequestered.

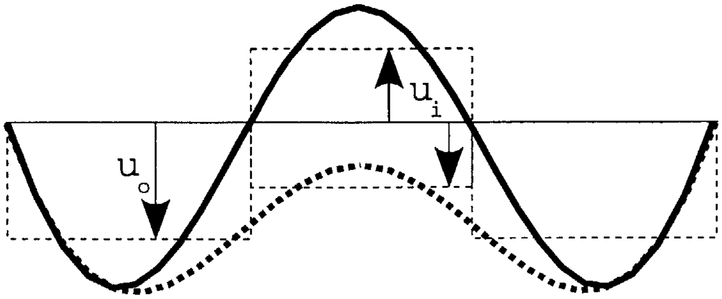

Figure 3-1: Counterflowing plume velocity profiles. The present model assumes a profile similar to the solid curved line. Other models infer a profile similar to the dashed curved line, so that the plume fluid flows downward everywhere. The dashed straight lines superimposed on the profiles represent corresponding top-hat profile approximations.

3.1 Motivation

The results of two studies which modeled CO_2 droplet plumes with time-dependent, three-dimensional Navier-Stokes models suggest that the droplets rise amidst descending fluid [55, 7]. Alendal et al. [7] modeled plume flow in an environment with both stratification and a crossflow, although one stagnant case was also considered. They used a modeling technique in which each phase, the dispersed droplets and the seawater, are modeled as separate continuous phases which are coupled by drag forces and mass transfer. With an initial droplet radius of 0.7 cm and a CO_2 flow rate of 1 kg/s, the pH field of the modeled plume rose about 75 meters above the release, and extended 50 meters below the release until the edge of the domain was reached.

In another study, Sato [55] used a mixed-fluid "drift-flux" scheme to model the dispersed (droplet) phase. The minimum node spacing was $1.0 \times 1.0 \times 8.0$ m (with the larger spacing oriented vertically). Modeling the case of a dissolving CO_2 droplet plume with no current or stratification, Sato found that the total height of the plume was insensitive to the initial droplet radius and that this height was smaller than the rise height of a single isolated droplet. This occurred because the fluid in the modeled plume flowed downward.

As these models make predictions that are substantially different from the present model, it is necessary to determine experimentally whether the fluid amidst the droplet core tends to rise with the droplets or descend against them.

3.2 Experimental Design

Some simple scoping experiments were performed to resolve this issue. The main differences between most stratified air-bubble plume experiments and a field CO_2 release are the enhanced negative buoyancy of the water in the latter case due to solute density effects, and the decreasing positive droplet buoyancy in the latter case due to dissolution. The net effect is that the ratio of negative buoyancy flux to positive buoyancy flux can be much greater in the CO_2 droplet plume than in the air-bubble case.

In order to simulate this situation, and evaluate the behavior of the fluid in the droplet (in these experiments, bubble) core, an experiment was devised in which the relative buoyancy fluxes of the fluid and the bubbles could be manipulated. This was accomplished by creating a counterflow system in which a rising bubble plume was surrounded by a descending single-phase plume of dense saltwater ("brine"). This brine was emitted from a port system located above the bubble plume source.

It is worthwhile estimating the worst-case ratio of positive to negative buoyancy ratios that might be encountered. A single kilogram of CO_2 at 800 meters depth will, with a density of 935 kg/m^3, exert a buoyant force of one Newton. The same kilogram of CO_2, dissolved in a cubic meter of seawater, will induce a negatively buoyant force of 2.8 N. Thus, the worst-case buoyancy ratio between rising droplets and descending fluid, neglecting stratification, is 1:2.8. This worst-case will only occur in plumes in which one outer plume segment shrouds the entire inner plume, and stratification is negligible. In practice, the ratio of positive to negative buoyancy flux at any given height in the plume will be greater than 1:2.8. As described in Section 4.1.2, the buoyancy flux ratio for a typical CO_2 release is typically 1:1.

3.2.1 Apparatus

The experiments took place in a $1.2 \times 1.2 \times 2.4$ m glass-walled tank described elsewhere [59]. An aquarium-type air diffuser was located on a small platform approximately 80 centimeters above the base of the tank, so that the bottom of the tank could collect descending brine. In a saltwater environment, this diffuser produced bubbles with a diameter of approximately 1-2 mm. A four-port diffuser, called the brine diffuser, was located ninety centimeters above the air diffuser. Each port consisted of a circular orifice with a diameter of about 2 mm. The four orifices were located on the vertices of an imaginary square with a length of 12.5 centimeters centered above the air diffuser. The purpose of spacing the ports in this manner was to ensure that the fluid emitted from the diffuser would envelop the rising bubble swarm. A schematic of the experimental setup is shown in Figure 3-2.

A thin rod was attached to the diffuser so that its tip was located along the centerline

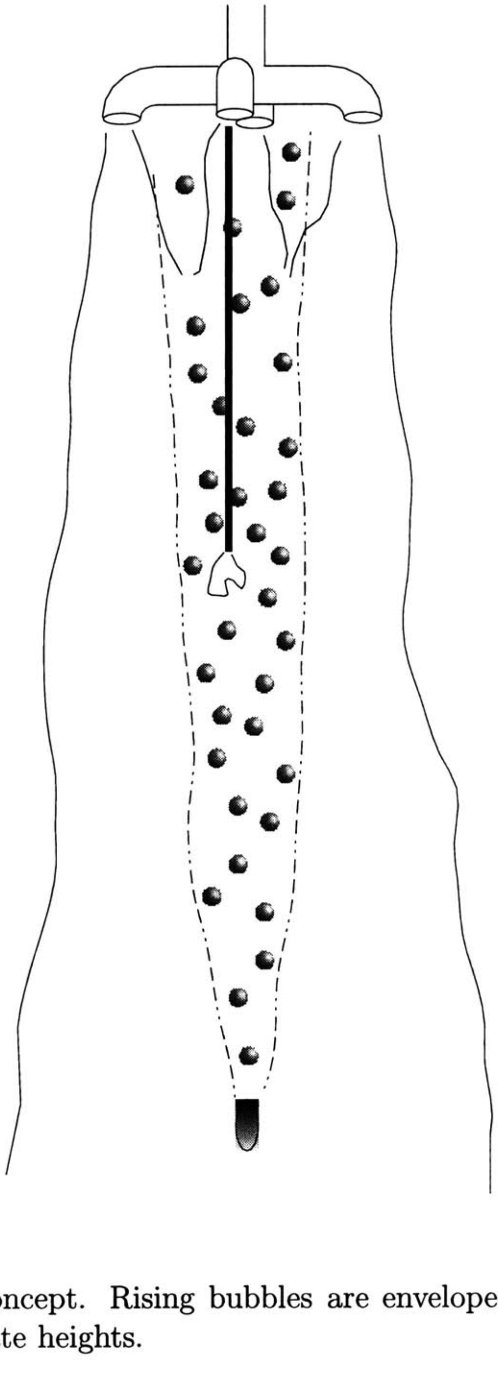

Figure 3-2: Experimental concept. Rising bubbles are enveloped by a descending plume. Dye is injected at intermediate heights.

between the brine diffuser and air diffuser. Plastic tubing was attached to this rod, with the end of the tubing located at the end of the rod. The other end of the tubing, located outside of the tank, was attached to a syringe loaded with Rhodamine 6G dye. The purpose of this setup was allow injection of small amounts of dye into the plume near its centerline to aid flow visualization. The depth of the rod tip could be adjusted to allow dye injection into different heights in the plume. Once injected, the dye was illuminated by a laser light sheet which was aligned with the centerline of the tank. Digital images of the dye were recorded with a digital camera, to allow quantitative analysis of the dye images. This experimental setup was devised as an add-on to other plume studies conducted at MIT. [59].

3.2.2 Methods

The tank was first filled with unstratified salt water (NaCl) with a density of 1005 kg/m^3. The purpose of using salt water was to narrow the size spectrum of bubbles. Then, the bubble plume was initiated by delivering a controlled, metered air flow to the air diffuser. Once a bubble plume was established, dense brine was supplied to the brine diffuser with a peristaltic pump at a constant, controlled flow rate. After allowing the downward flowing brine plume to become established, which typically took one to two minutes, the two slugs of dye were injected into the plume about thirty seconds apart. The dye slugs were meant to be delivered as an instantaneous release, but were typically delivered over an interval of two to five seconds. The slugs were also injected downward with a small initial velocity, so that the experiment was slightly biased against rising dye. The digital camera was configured to record several frames per second.

Name	Air Flow mL/min	Brine Flow mL/min	Air Buoy. Flux m^4/s^3	Brine Buoy. Flux m^4/s^3	Buoy. Ratio
a	100	715	1.6×10^{-5}	1.6×10^{-5}	1:1
b	200	1430	3.2×10^{-5}	3.2×10^{-5}	1:1
c	100	1430	1.6×10^{-5}	3.2×10^{-5}	1:2
d	100	1790	1.6×10^{-5}	4.0×10^{-5}	1:2.5

Table 3.1: Experimental parameters. For air, $\Delta\rho/\rho_a \approx 1$; for the brine used in these experiments, $\Delta\rho/\rho_a \approx 0.14$.

Both the air flow rate and the brine flow rate were varied in order to vary the ratio of positive buoyancy flux to negative buoyancy flux. The ratio was varied from 1:1 (air:brine) to 1:2.5 in the main body of experiments. The difference in density between the brine and the ambient tank water was 140 kg/m^3, while the difference in density between the tank water and the bubbles was $\approx$ 1000 kg/m^3. The air and brine flows for the primary set of experiments are summarized in Table 3.1.

3.2.3 Observations

The primary result of these experiments was that, for a buoyancy flux ratio ranging from 1:1 to 1:2.5, injected dye was observed to rise above its release point, indicating that the fluid located in the bubble core was in fact rising.

In all cases, the dye was observed to rise at least 10 cm or so above the release point, depending on the release depth and the buoyancy flux ratio. Dye was visibly entrained from the inner rising fluid to the falling outer fluid and re-entrained from the outer fluid to the rising inner fluid.

It was possible to estimate fluid velocities in both the rising and descending regions of

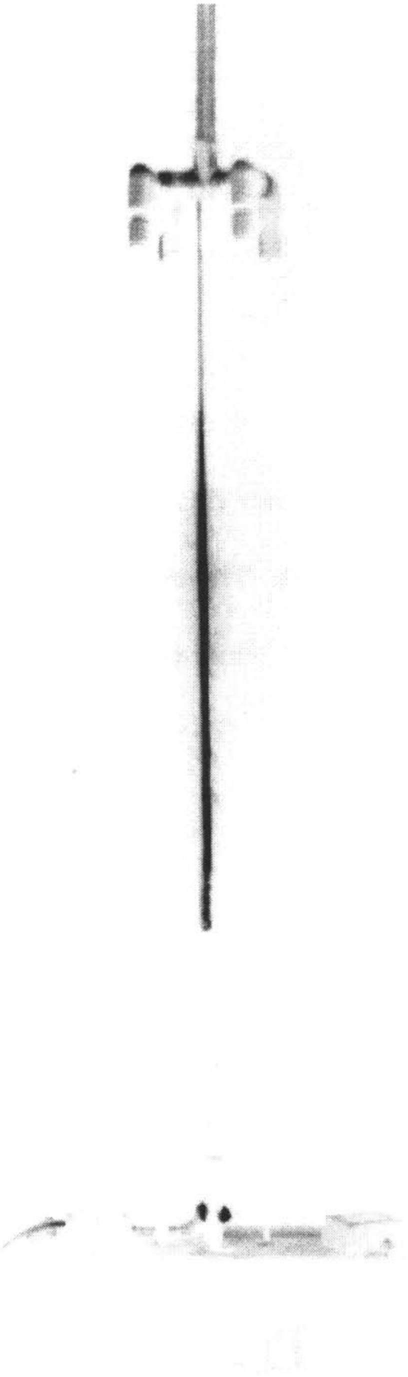

Figure 3-3: Image of experimental setup. The brine diffuser is at the top of the image, and the air diffuser is near the bottom. The dark line extending toward the air diffuser is the rod supporting the dye tubing.

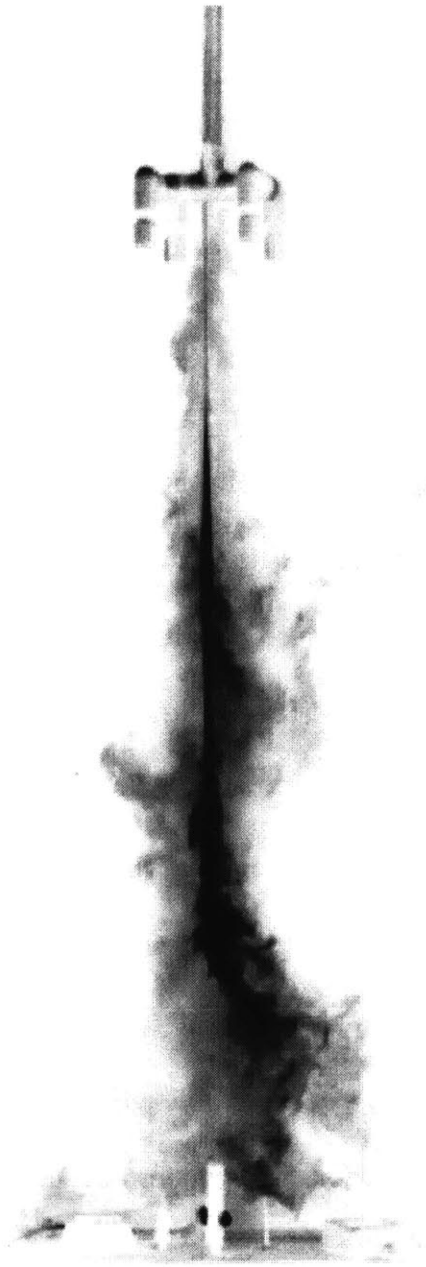

Figure 3-4: Image of dye release. Some of the injected dye rises the length of the experimental section. Much of the dye is stripped out by the descending outer plume.

the plume. These velocities were estimated by tracking the vertical advection of dye over the course of several captured images of the plume. Though rough, such measurements provide information that may be used for evaluating model parameters. This topic is discussed in Section 4.3.5.

3.2.4 Discussion

These rough experiments indicate that, over the range of buoyancy flux ratios that might be realized in a CO_2 droplet plume, the fluid in the immediate vicinity of the droplets should rise with the droplets. It is also clear that the rate of mixing between the rising and falling fluid is quite rapid, so that the residence distance over which a dye packet might travel in the rising inner plume before transferring to the descending outer plume is quite short. Essentially, the plume is "well-mixed."

These limited experiments do not fully resolve the issues at hand. The limited measurements do not allow rigorous analysis of the velocity profiles and entrainment rates. Also, while source buoyancy flux ratio is a significant factor in determining the velocity of the inner plume fluid, it is not the only one. Bubble slip velocity is another variable which is expected to impact the plume behavior, given its importance in stratified air bubble plumes.

Chapter 4

Results

This chapter has two purposes: to assess the validity of the model, and to investigate how sensitive its predictions are both to design variables and to uncertain parameters such as entrainment coefficients.

In Section 4.1, model settings for both a dissolving CO_2 droplet plume and a shallow air bubble plume, which serve as a baseline for sensitivity studies, are introduced. Examination of the latter case allows investigation of model behavior independent of dissolution effects which tend to dominate plume behavior and obscure other dynamics of interest. This case is meant to illustrate the sensitivity of the plume volume flux to some parameters. Section 4.2 reviews the sensitivity of the model output to both input parameters that are design variables, such as CO_2 flow rate and initial droplet diameter, and parameters which arise from the submodels of Section 2.3.

Evaluation of plume sensitivity depends on the choice of metrics used when analyzing model output. The two primary metrics used are the vertical scale of the plume and the mean concentration of CO_2 in plume fluid at the bottom of each outer plume segment, which is where the nearly neutrally buoyant fluid exits the plume and intrudes into the ambient environment. This point marks the end of the plume near-field, where plume dynamics dominate, and the start of the far-field, where ambient mixing controls further dissolution. To measure the vertical scale of the plume, four variables are tracked: the total plume height, the height of the uppermost intrusion, the height of the lowest intrusion, and the mean of the intrusion depths, weighted by the volume flux in each intrusion. The latter term represents a characteristic intrusion depth, while the difference between the highest and lowest intrusions represents the range of intrusion depths. Intrusion depths are pertinent because they represent the initial sequestration depth of the CO_2. It is also of interest whether the lowest intrusion depth and even the mean intrusion depth are below the point of release, which could have implications for impacts on benthic organisms if the diffuser is mounted on the sea bottom.

In Section 4.3, model results are compared to datasets describing various experimental plumes. Notably lacking are data for plumes with significant dissolution effects; such data is not available.

4.1 Base case

To provide a context for the parameter sensitivity results, it is useful to introduce typical results for the two scenarios under consideration, the shallow air bubble case and the deep, dissolving CO_2 case. The details of the release conditions, as well as preliminary choices for model parameters, are summarized in Table 4.1.

Case	Air	CO_2
Release Depth, z_0	50 m	800 m
Droplet Diameter, d_b	1.8 cm	0.5 cm
Flow Rate, Q_0	20 L/s	1.1 L/s
$\Delta\rho/\rho$	≈ 1.0	≈ 0.1
Buoyancy Frequency, N	$4.0 \times 10^{-2}\ s^{-1}$	$3.2 \times 10^{-3}\ s^{-1}$
Parameters	**Air**	**CO_2**
ξ	1.1	1.1
Entrainment	*BC*	*AI*
α_i	0.11	0.11
α_o	0.11	0.055
α_a	0.11	0.11
ϵ	0.01	0.1

Table 4.1: Base case release conditions. Flow rates are given in terms of in-situ pressure.

4.1.1 Air Bubble Plume

The radii, velocities, and density differences of the stratified ($N = 4.0 \times 10^{-2}\ s^{-1}$) air bubble plume are shown in Figure 4-1. While the velocity and flux quantities of the outer plume are generally negative, they are shown in these figures with reversed signs, to allow easy comparison with inner plume values. On the left panel, the radii are plotted in a mirrored fashion in order to simulate a profile. The middle panel shows the evolution of the characteristic plume velocities with height as well as the droplet slip velocity. The peeling event occurs over a short distance and the outer plume segments are spaced widely apart from one another (no attempt has been made to model the surface flow accurately).

Figure 4-2 illustrates the volume and buoyancy fluxes of this plume. The volume fluxes of the inner and outer plumes are of comparable order. Also, the buoyancy flux of the rising bubbles is significantly greater than that of the inner and outer plumes.

The volume flux of the inner plume divided by the rate of flow out of the inner plume,

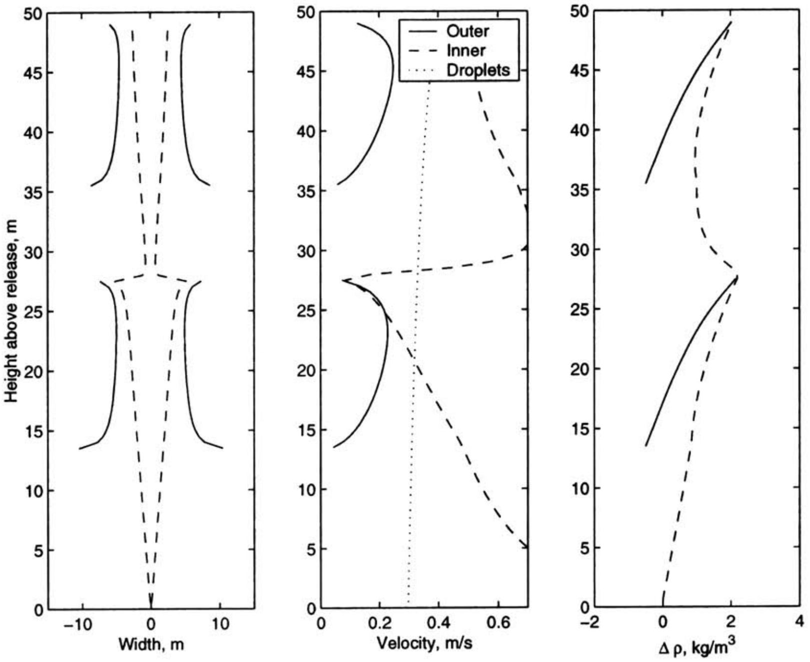

Figure 4-1: Air bubble plume properties, base case.

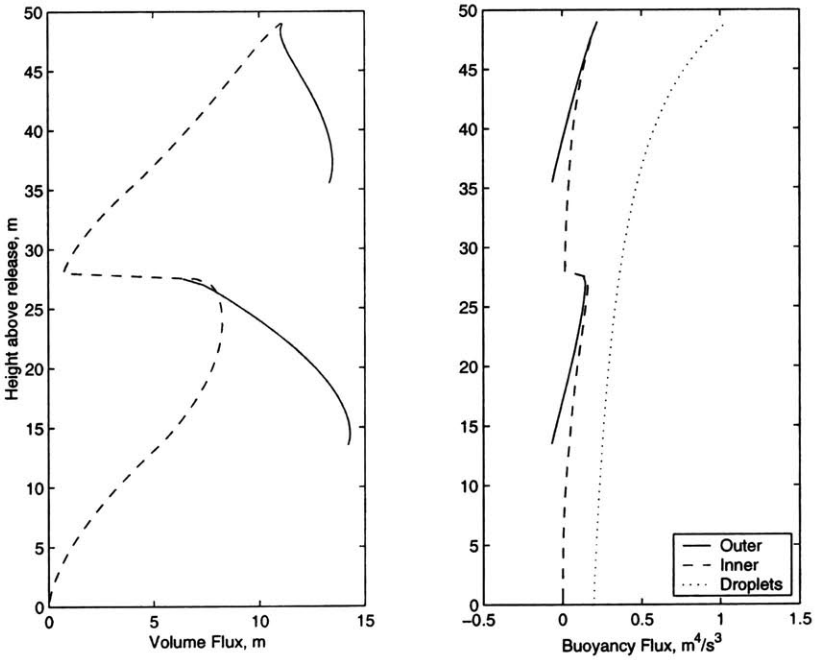

Figure 4-2: Air bubble plume fluxes, base case.

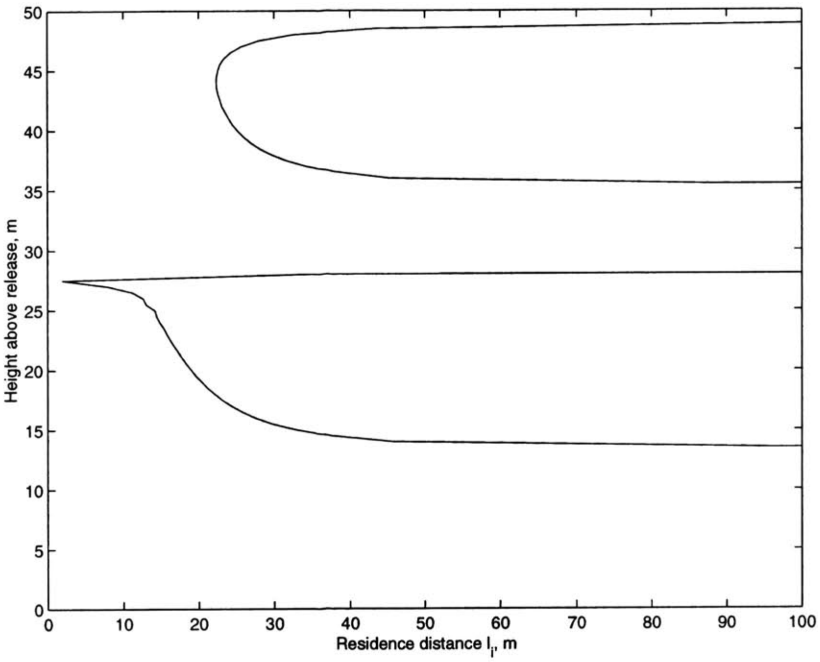

Figure 4-3: Air bubble plume residence distance, base case.

$l_i = Q_i/(E_o + E_p)$, is shown in Figure 4-3. The quantity l_i represents a characteristic vertical "residence distance" for the inner plume. It signifies the length a fluid particle might typically travel from the point where it is entrained into the inner plume to the point where is it lost from the inner plume, either due to turbulent entrainment or buoyant detrainment. Except near the peeling event, the residence distance is of the same magnitude as the plume height, or greater.

4.1.2 CO_2 Plume

Properties of the base CO_2 plume case are shown in Figures 4-4, 4-5, and 4-6. In all the figures, outer plume velocities and flux quantities, generally negative, are plotted with reversed signs to aid comparison with inner plume quantities.

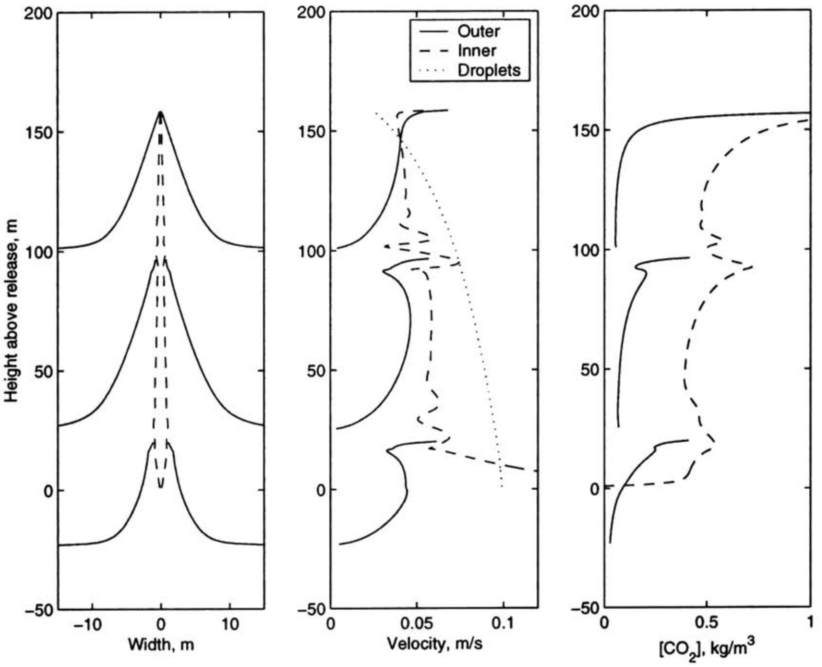

Figure 4-4: CO_2 Plume properties, base case.

In Figure 4-4, the leftmost panel illustrates the characteristic radii of the inner and outer plume. The outer plume is substantially wider than the inner plume. The middle panel shows the plume velocities as well as the droplet slip velocity. The velocity of the outer plume is generally about half that of the outer plume. The rightmost panel shows the concentration of dissolved CO_2 in the inner and outer plumes. Of primary concern in terms of environmental impact is the CO_2 concentration at the bottom of each outer section, which is where, fortuitously, the CO_2 concentrations are lowest.

Figure 4-5 shows three plume flux quantities. The symbols on the side of this panel indicate the locations of four quantities that are used as metrics in the sensitivity studies. They are, from top to bottom, the plume height, the location of the topmost intrusion, the weighted mean intrusion height, and the location of the lowest intrusion. The volume flux

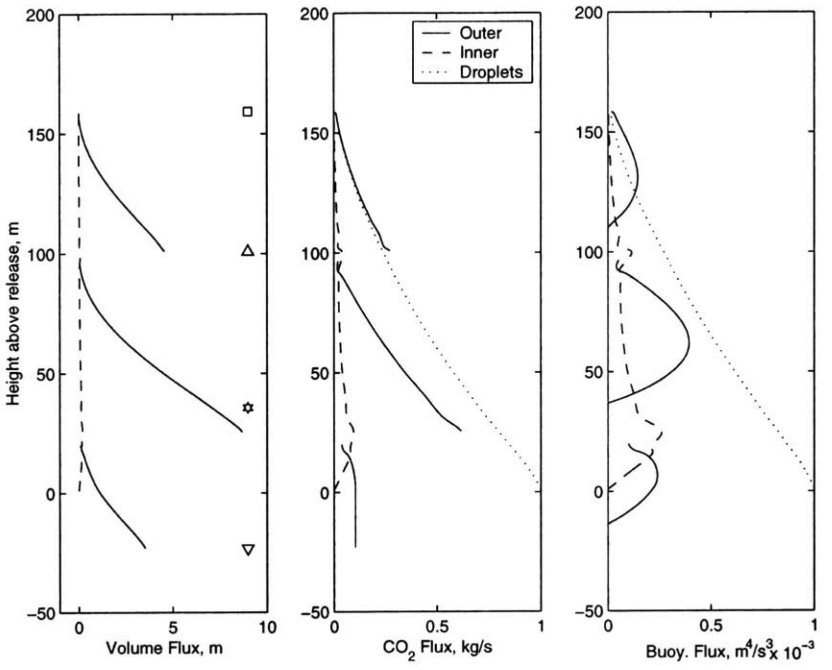

Figure 4-5: CO_2 Plume fluxes, base case.

profiles are shown on the left; as suggested by the plots of plume radii and velocities, most of the water in the plume is in the outer plume. Subsequently, most of the dissolved CO_2 is also in the outer plume, as shown in the middle plot. The profiles of CO_2 flux in the outer plume very closely mirror that of the CO_2 droplet flux, indicating that the dissolved CO_2 spends little time in the inner plume. The rightmost figure illustrates buoyancy fluxes for the plume sections and the buoyancy flux associated with the rising droplets. The signs of the fluxes in this plot are inconsistent for display purposes; positive values for the inner and outer plumes indicate that the fluid is heavier than ambient, while positive values for the droplets reflect the positive buoyancy of the droplets. The purpose of this plot is to illustrate the fact that the outer plume buoyancy flux is never much greater in magnitude than the buoyancy flux of the droplets.

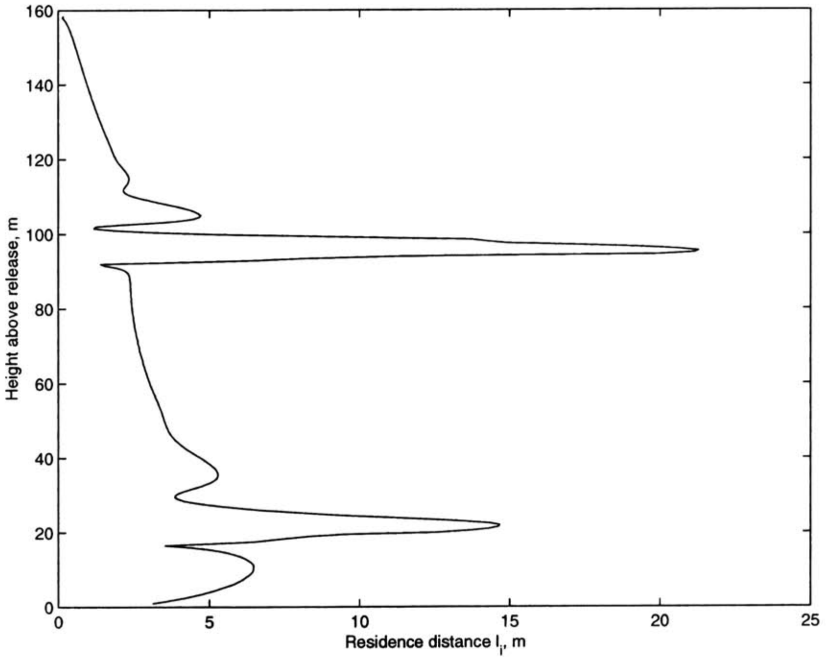

Figure 4-6: CO_2 Plume residence distance, base case.

The characteristic vertical residence distance for the inner plume is shown in Figure 4-6. Unlike the air bubble plume, the residence distance is much smaller than the vertical scale of the plume.

4.2 Model Sensitivity

This section explores the sensitivity of the model results with respect to both model parameters and design variables. Examining the sensitivity to model parameters is necessary to determine how accurate the model results are: if the model is quite sensitive to a parameter that is not well known, the accuracy of the results must be viewed with some uncertainty. In the current case, the design variables are CO_2 flow rate, the initial droplet size, and the

Parameter	Range
Mass transfer reduction	1 - 20
Entrainment coefficients α_i, α_o, α_a	0.02 - 0.15
peeling parameter ϵ	0.001 - 20
Momentum amplification ξ	1.0 - 2.0
Slip velocity multiplier	0.2 - 6.0
Density effect multiplier	0.0 - 2.0
Entrainment method	*AI / BC*

Table 4.2: Test ranges for parameters.

ambient stratification. The latter is considered a design variable because it can be varied somewhat according to the choice of the release location and depth.

4.2.1 Model Parameters

This section presents the results of model runs in which model parameters were varied individually to test for model sensitivity. The parameters involved, and the range over which they are varied, are summarized in Table 4.2.

Entrainment Coefficients

The entrainment assumption is central to the model formulation, so it is reasonable to expect that the model behavior is sensitive to variations in the entrainment coefficients. To check this sensitivity, the base case was modified by varying the three entrainment coefficients α_i, α_o, and α_a. Permuting the three coefficients over a set of four values, $0.02, 0.05, 0.10, 0.15$, resulted in 64 model runs. The resulting plume height for each combination is shown in Figure 4-7. Although changes in plume height do not completely describe changes in plume behavior from one case to the next, it does serve as a useful metric for evaluating plume

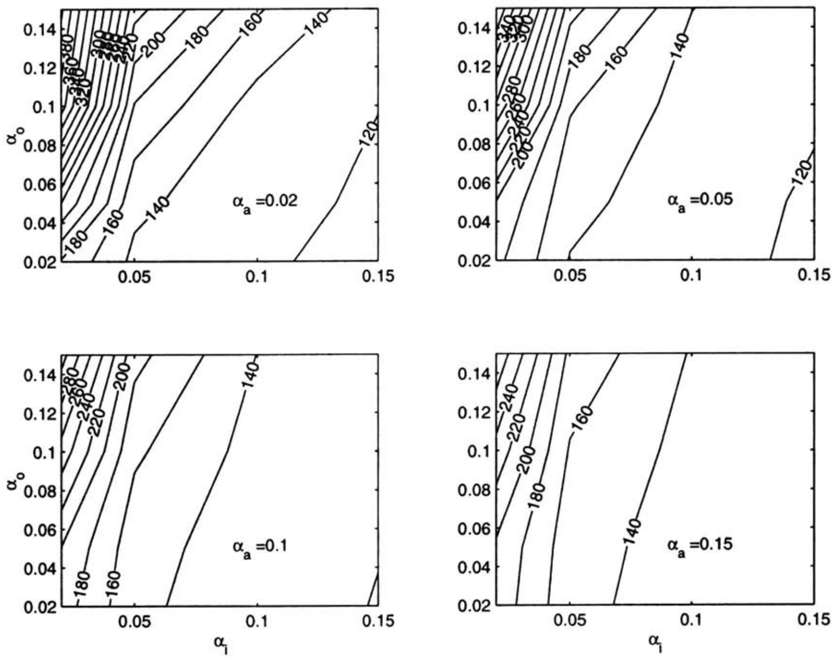

Figure 4-7: Sensitivity of plume height to entrainment coefficients.

sensitivity.

There are several apparent conclusions. One, the sensitivity of the plume height decreases with increasing entrainment coefficients: changing from $0.10, 0.10, 0.10$ to $0.15, 0.15, 0.15$ does not change the plume height significantly. On the other hand, the plume height changes quite a bit with changing coefficients when at least one of the coefficients is small. Further, plume heights become very large as α_i becomes very small and α_o becomes very large. This occurs because such combinations result in an inner plume with a very narrow, fast moving inner plume. This is not likely to reflect reality. If all combinations where at least one of the coefficients is 0.02 are neglected, the predicted plume height is $143 \pm 25.9\ m$, which represents the mean ± 1 standard deviation of the predicted height data.

Another sensitivity, the sensitivity of the CO_2 concentration in fluid leaving the plume

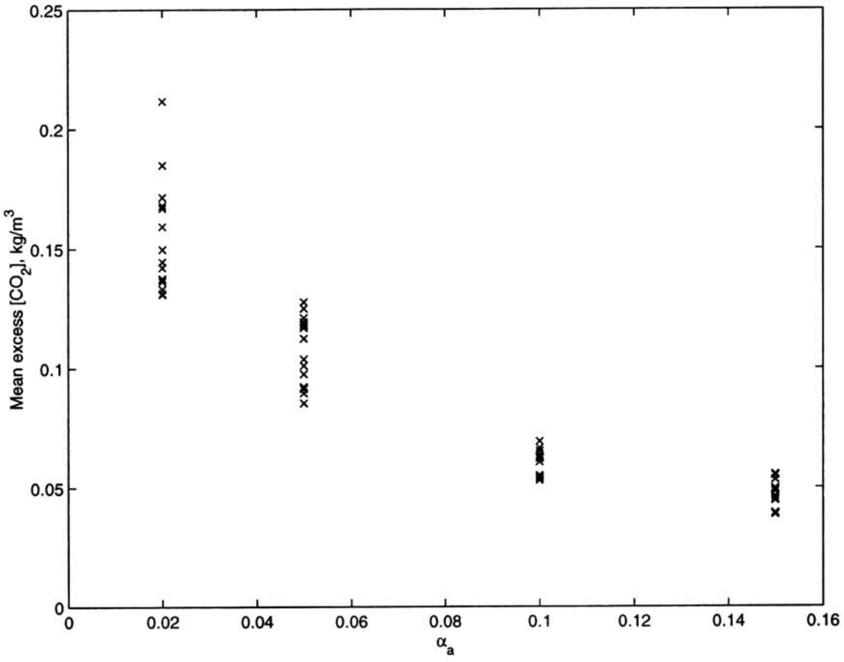

Figure 4-8: Sensitivity of CO_2 concentration to entrainment coefficients.

to entrainment coefficients is shown in Figure 4-8. In this plot, CO_2 concentrations are plotted against α_a, the entrainment coefficient for the outer plume. For each value of α_a, the concentrations for the 16 different combinations of α_i and α_o are plotted. The clear trend is that CO_2 concentrations decrease with increasing α_a. Considering only the cases with all coefficients greater than 0.02, the predicted CO_2 concentration is 0.09 ± 0.04 kg/m^3.

Although the entrainment coefficients for this type of plume are not well established, if one assumes that they are all in the range from 0.05 to 0.15, then one may conclude that the sensitivity of the model to entrainment coefficients is tolerable.

The uncertainty is reduced if one presumes to know α_a with some precision. As this coefficient describes mixing from the ambient into the outer plume, which is essentially a single-phase plume, it is reasonable to suppose that $\alpha_a \approx 0.11$. Considering only the test cases with $\alpha_a = 0.10$, the predicted plume height is $141 \pm 21.9\ m$. While this represents only a marginal improvement in uncertainty, the predicted CO_2 concentrations become much less scattered: with $\alpha_a = 0.10$, the model predicts a mean intrusion concentration of $0.064 \pm 0.003\ kg/m^3$.

Finally, one may compare different entrainment models. Figure 4-9 illustrates the differences in volume flux between three cases: AI_A corresponds to the AI model (Equation 2.64) with $\alpha_i = 0.055$, $\alpha_o = \alpha_a = 0.11$, as used in the CO_2 base case. AI_B corresponds to the AI model with $\alpha_i = \alpha_o = \alpha_a = 0.11$. Finally, BC_A corresponds to the BC model (Equation 2.65) with $\alpha_i = 0.11 = \alpha_o = 0.11 = \alpha_a = 0.11$. While Asaeda and Imberger [9] and McDougall [42] achieved good model results with AI_A, it is worthwhile examining other sets of coefficients.

The coefficient $\alpha_i^{BC_A}$ is double that of $\alpha_i^{AI_A}$ because E_i^{AI} is proportional to $u_i - u_o$, while E_i^{BC} is proportional to u_i alone. As u_i and u_o are generally of the same magnitude, one would expect the two models to be comparable if $\alpha_i^{BC} \approx 2\alpha_i^{AI}$. More generally, one would expect comparable results if $\alpha_i^{BC}/\alpha_o^{BC} \approx 2\alpha_i^{AI}/\alpha_o^{AI}$, as this ratio plays a significant role in determining the inner plume velocity. The volume flux profiles for the three cases are similar: the difference in plume height is 16 percent, while the mean CO_2 concentrations in the intrusions match to within five percent.

Peeling Parameter

Another significant model parameter which is not well established is the peeling coefficient ϵ. As this is a novel parameter, it is necessary to explore model sensitivity over a wide range

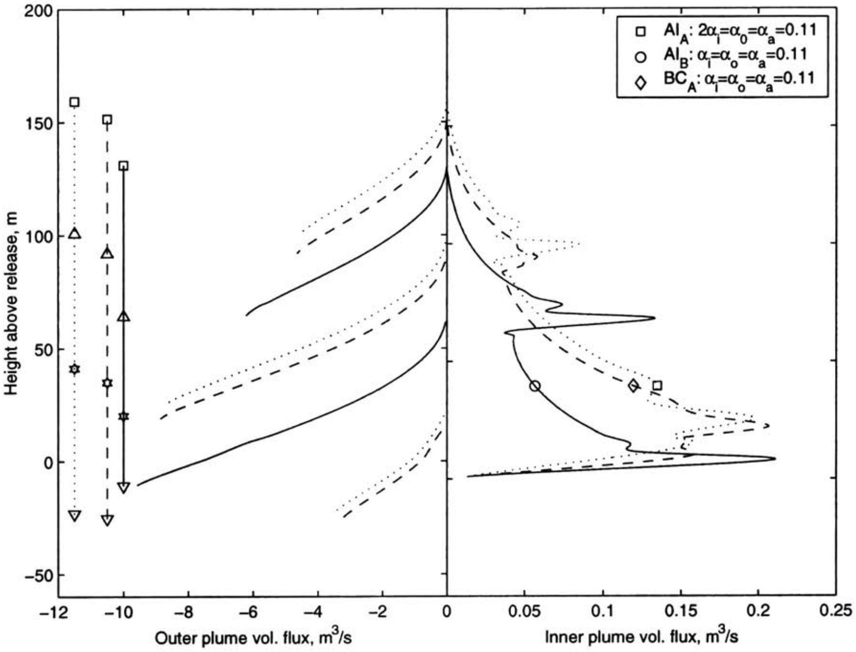

Figure 4-9: Sensitivity of plume structure to entrainment method.

of parameter values. Figure 4-10 plots the plume height, maximum intrusion height, mean intrusion height, and minimum intrusion height versus the peeling parameter, ϵ, which ranges over four orders of magnitude. Over this range, the plume height varies from 150 m to 250 m, and the mean intrusion height, relative to the release point, varies from 35 m to 75 m. While these changes are significant, it is worth noting that most of the variability occurs between $\epsilon = 5 \times 10^{-2}$ and $\epsilon = 2 \times 10^{1}$. One may argue, in fact, that this increasing trend is evidence that these values of ϵ are too high— peeling occurs too readily, leaving a fast-moving, slender inner plume, similar to that obtained by low ratios of α_i/α_o.

The sensitivity of the mean intrusion CO_2 concentration to the peeling parameter is quite negligible, as illustrated in Figure 4-11. This result suggests that the CO_2 concentrations are strongly controlled by other factors.

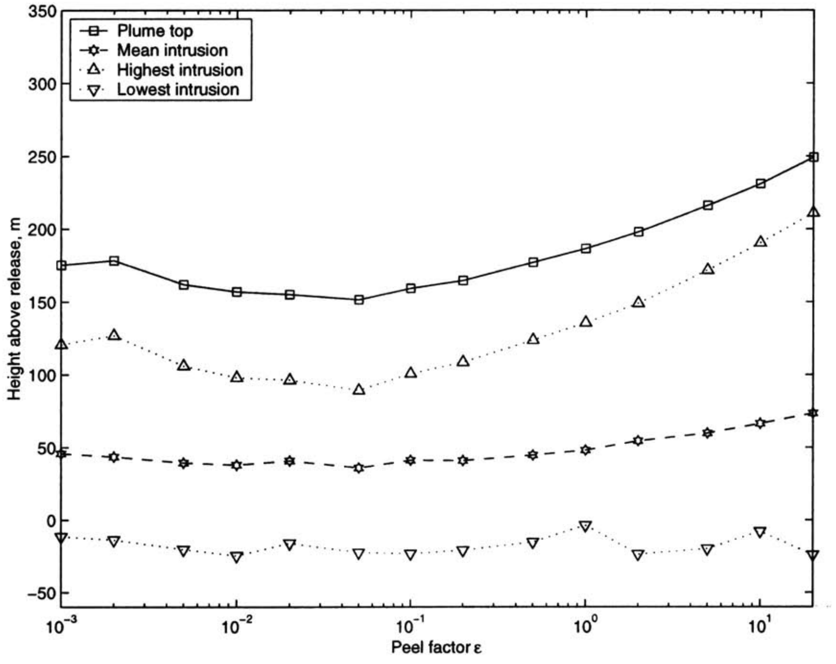

Figure 4-10: Sensitivity of plume structure to the peeling parameter, ϵ.

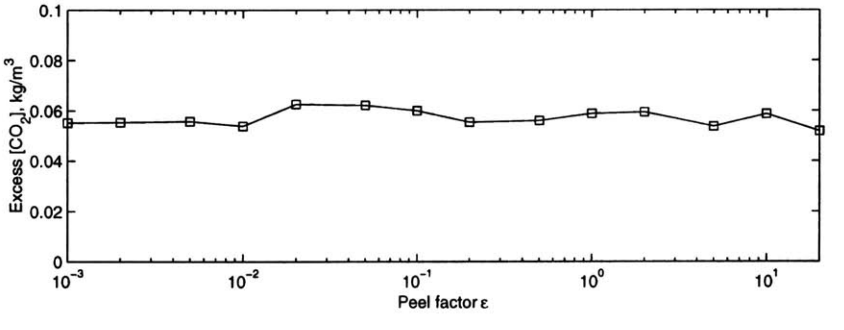

Figure 4-11: Sensitivity of CO_2 concentration to the peeling parameter, ϵ.

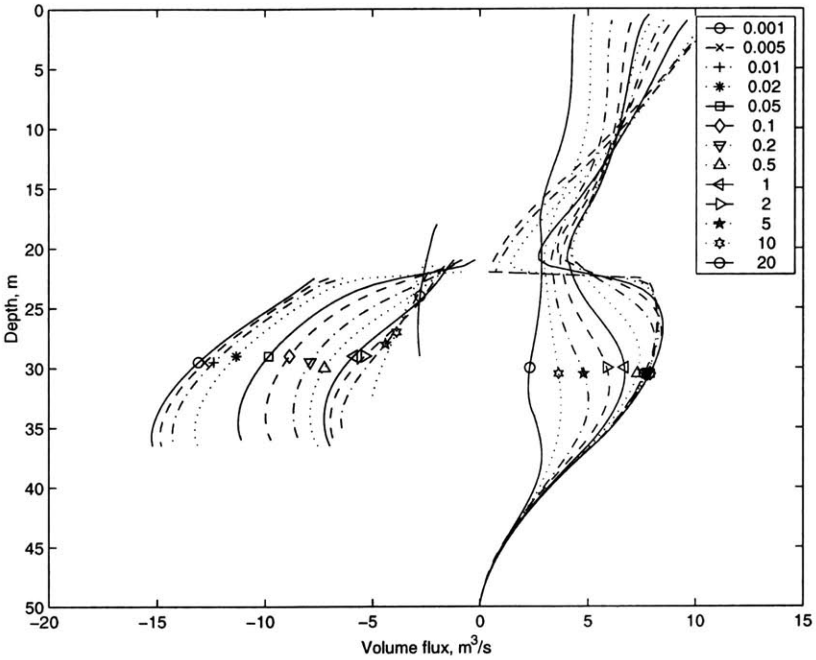

Figure 4-12: Sensitivity of air bubble plume volume flux to the peeling parameter.

Figure 4-12 illustrates the evolution of profiles of volume flux for the inner and outer portions of an air bubble plume versus changes in ϵ. The profiles that are consistent with experimental observations of Type 2 bubble plumes in stratification correspond to $\epsilon \ll 1$. Of course, ϵ may not be a constant across plume conditions. But what is also evident in this figure is that the plume behavior near the peeling event is relatively insensitive to variations at the low end of the range, just like the CO_2 case.

Momentum Amplification

To check sensitivity to the momentum amplification term, ξ was varied over the values $1.0, 1.1, 1.2, 1.5, 2.0$. Figure 4-13 reveals that the plume behavior is quite insensitive to this parameter. CO_2 concentrations are not sensitive either.

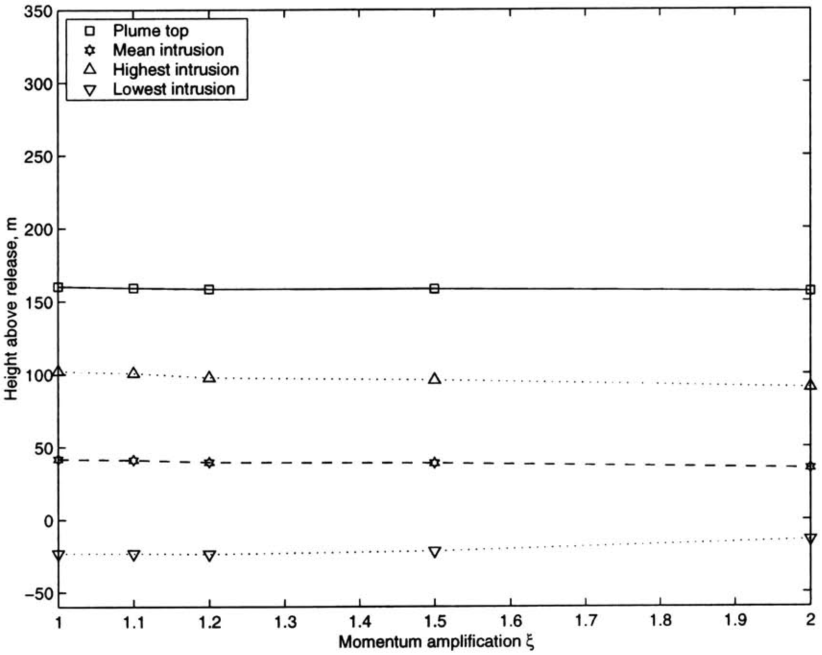

Figure 4-13: Sensitivity of plume structure to momentum amplification.

Slip Velocity

To extend the slip velocity range, the slip velocity was scaled over a range of 0.2 to 2.0 times the calculated value. Slip velocity can affect plume behavior in several ways. Increasing slip velocity increases the rate of mass transfer, all else being equal, but the latter does not increase as quickly as the former, so the droplet, independent of plume effects, should rise higher. On the other hand, faster slip velocities lead to a lower effective buoyant force, leading to more sluggish, Type 3 plume behavior. In the case of this model, increasing slip velocity also effectively increases the rate of buoyant detrainment, as the slip velocity, cubed, is in the numerator of this expression (Equation 2.67). So scaling the slip velocity also increases the effective rate of peeling in a manner that may not be realistic. As this effect confuses the situation, the peeling parameters were scaled down with increasing slip

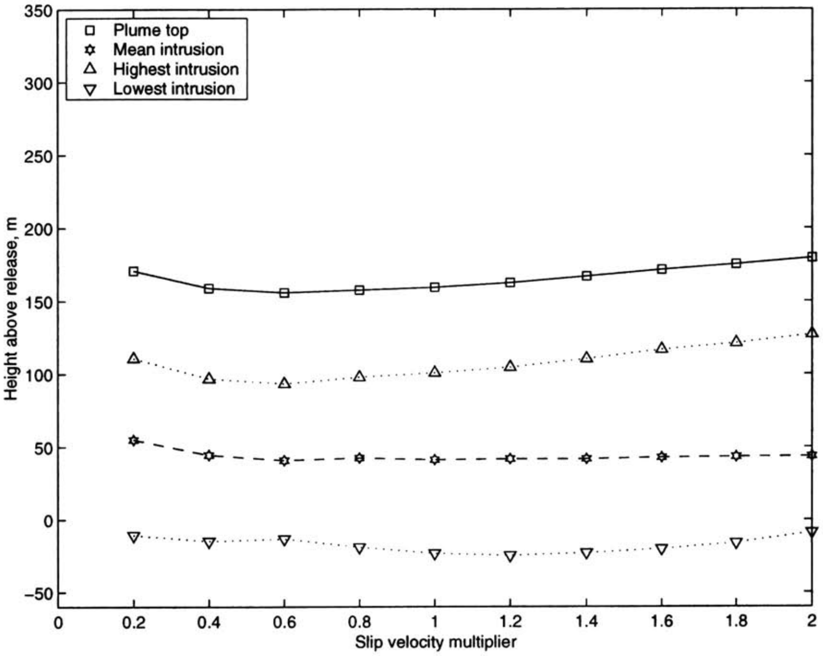

Figure 4-14: Sensitivity of plume structure to slip velocity.

velocity so that the effective peeling parameter, ϵu_b^2, remained constant.

Model sensitivity is shown in Figure 4-14. The competing effects of slip velocity are evident, as the plume height increases slightly with very slow slip velocities (due to a larger effective buoyant force acting on the plume) and with very large slip velocities (due to a decrease in the ratio of mass transfer to slip velocity). However, the sensitivity is not great.

Volume flux profiles for air bubble plumes with different slip velocity multiples are shown in Figure 4-15. The outer plume fluxes are negative while the inner plume fluxes are positive. Two trends are apparent: Peel height decreases with increasing slip velocity, as expected, and maximum volume flux also decreases with increasing slip velocity. The characteristic mixing distance also decreases, as shown in Figure 4-16. This means that the plume approaches Type 3 behavior, as such plumes are characterized by short residence distances, as indicated

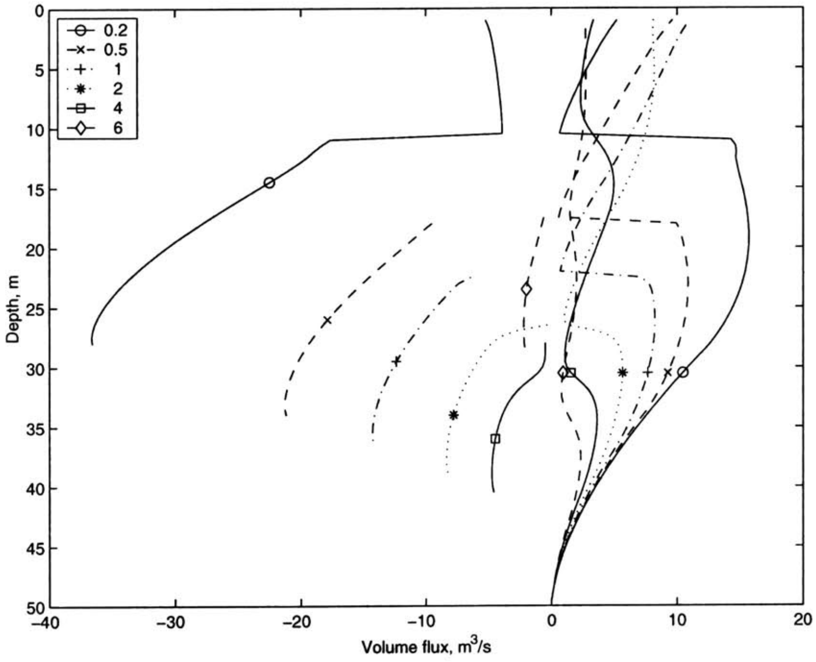

Figure 4-15: Sensitivity of air bubble plume volume flux to slip velocity.

by the small distances observed between intrusions. The present model, however, does not yield such closely-spaced intrusions. This is probably due to the fact that Type 3 plumes tend to be somewhat unsteady, irregularly ejecting eddies. The model, on the other hand, forces steady-state convergence.

Mass Transfer

The model is strongly affected by the mass transfer rate. To evaluate this sensitivity, the mass transfer reduction factor was varied over a range from 1 to 20. The base case uses a factor of 2, reflecting the mass transfer reduction factor associated with hydrate formation typical of many, but not all, experiments. A reduction factor of 20 results in mass transfer ten times slower than the base case. The initial droplet diameter used in these runs was 2

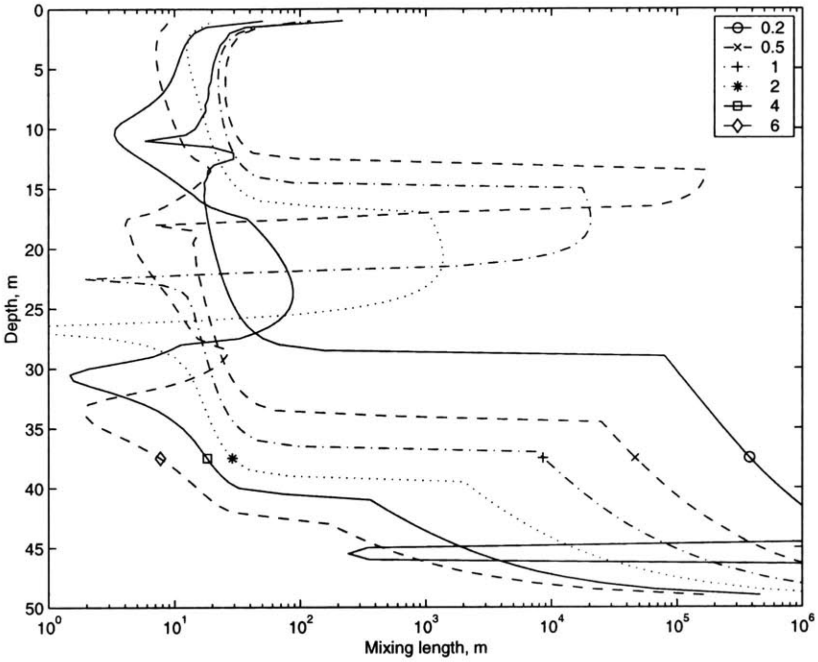

Figure 4-16: Residence distance sensitivity to slip velocity.

mm.

Figure 4-17 illustrates the sensitivity of the plume to the mass transfer rate. The structure of the plume is strongly affected by the effective mass transfer rate. The implications of this sensitivity are discussed in Section 4.2.2.

Surprisingly, the intrusion CO_2 concentrations are rather insensitive to the mass transfer rate, as shown in Figure 4-18. This result suggests that these concentrations are controlled by factors quite apart from the details of the plume itself.

Density Effect

Although the density effect of CO_2 is fairly well known, it is worthwhile examining plume sensitivity in order to gain insight into the role of the CO_2 solute density effect. To this

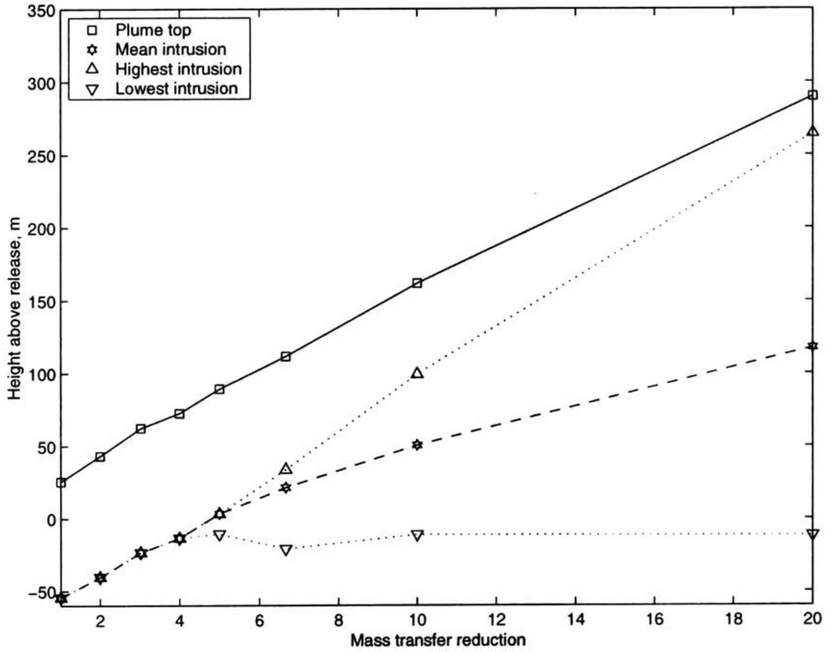

Figure 4-17: Sensitivity of plume structure to CO_2 mass transfer rate.

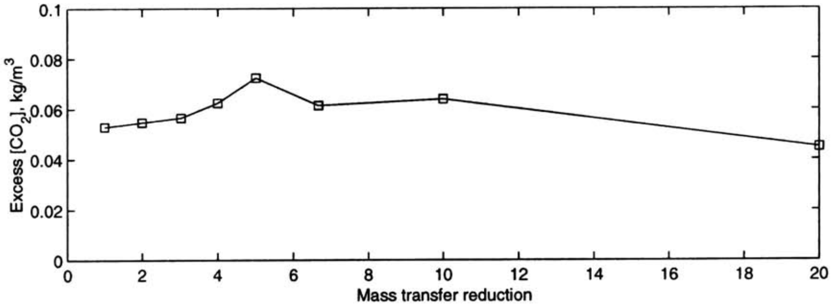

Figure 4-18: Sensitivity of CO_2 concentration to CO_2 mass transfer rate.

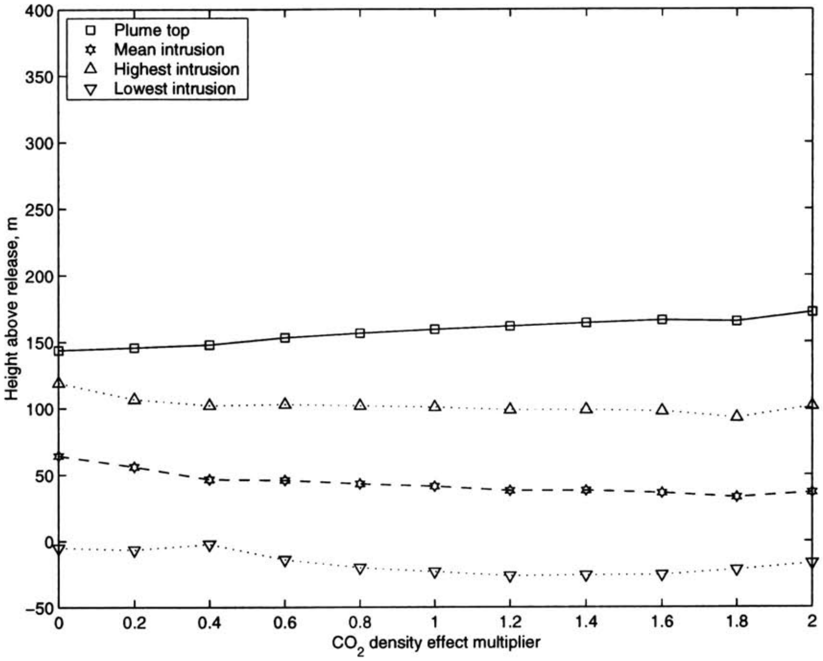

Figure 4-19: Sensitivity of plume structure to CO_2 solute density effects.

end, the density effect was scaled by a factor ranging from 0 to 2. The resulting plume behavior is summarized in Figure 4-19. This plot shows that plume height increases slightly with increasing density effect, while the top and mean intrusion heights decrease. This occurs because the outer plume sections, denser and faster moving, entrain more water from the inner plume, removing negative buoyancy and allowing it to rise higher. Overall, predicted plume behavior is surprisingly insensitive to this parameter. The CO_2 concentration, however, decreases with increasing density effect, as seen in Figure 4-20. This trend occurs because the outer plume segments are able to descend a longer distance with a larger velocity, encouraging dilution of the CO_2.

This exercise was repeated with an unstratified ambient, so that the density effect was the sole source of negative buoyancy. The results are shown in Figure 4-21. Of course, for

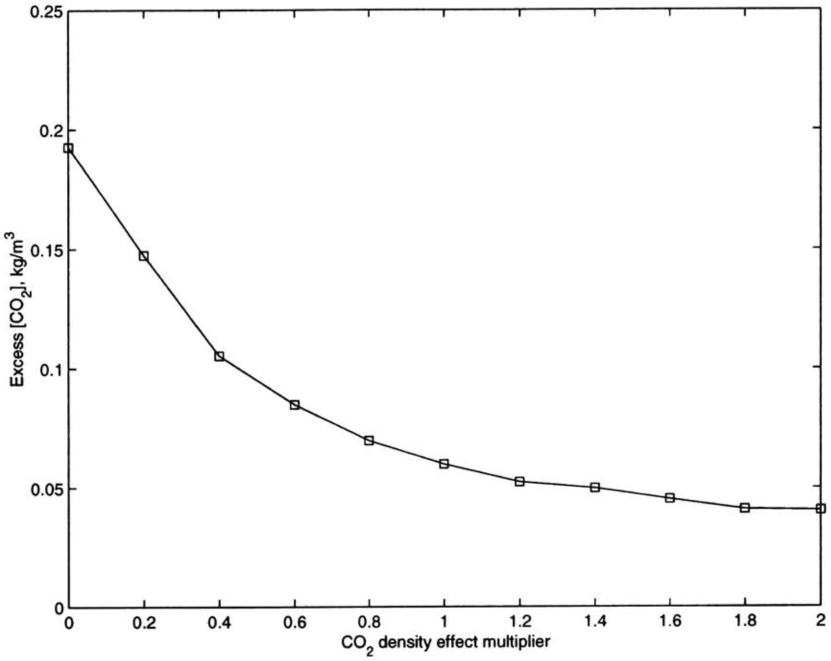

Figure 4-20: Sensitivity of CO_2 concentration to solute density effects.

the case where the density factor was zero, the plume did not form descending intrusions. Here as well, the plume height is surprisingly insensitive to the density effect. Mean intrusion CO_2 concentrations cannot be examined, because in this unstratified environment the outer plumes do not trap before reaching the edge of the model's domain.

4.2.2 Design Variables

The primary design variables for a CO_2 droplet release are stratification strength, initial droplet size, and volumetric flow rate. Variability in the mass transfer rate, although really a model parameter, is re-examined in this section because variations in mass transfer can be compensated for by variations in initial droplet size.

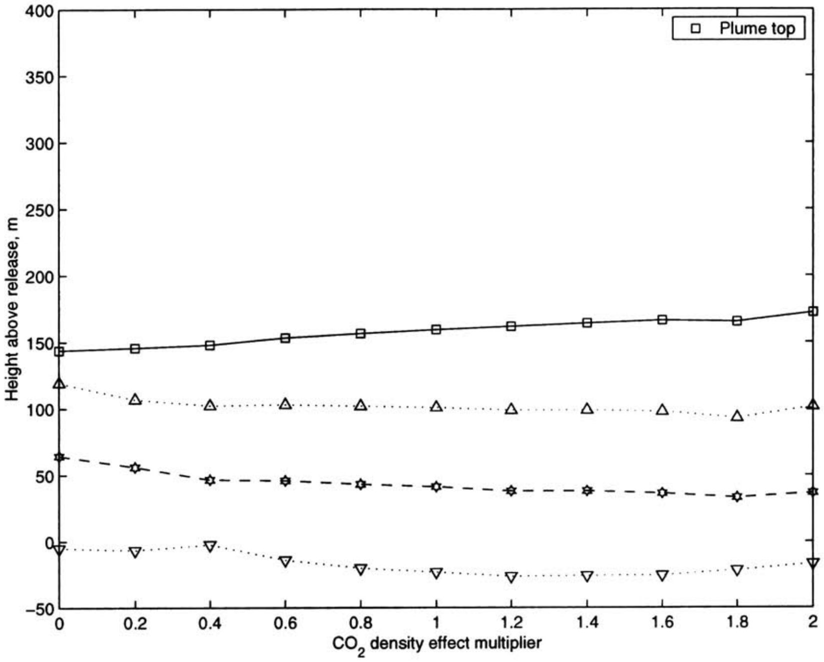

Figure 4-21: Sensitivity of plume structure to CO_2 solute density effects, unstratified case.

Stratification

The ambient density gradient, characterized by the buoyancy frequency, varies somewhat with geographic location and strongly with depth. One way to vary the stratification for a given site is to simply change the release depth. To evaluate sensitivity to stratification, the ambient density gradient was artificially decreased by a factor of four in order to half the buoyancy frequency to $N = 1.6 \times 10^{-3}\ s^{-1}$, and artificially increased by the same factor to provide a buoyancy frequency of $N = 6.4 \times 10^{-3}\ s^{-1}$. A comparison among plumes with the different degrees of stratification is illustrated in Figure 4-22. Although the rise heights are about the same, the cumulative volume flux in the intrusions decreases with increasing stratification because the outer segments trap more readily. Thus, the CO_2 concentrations, which are inversely proportional to the total intrusion volume flux, increase with increasing

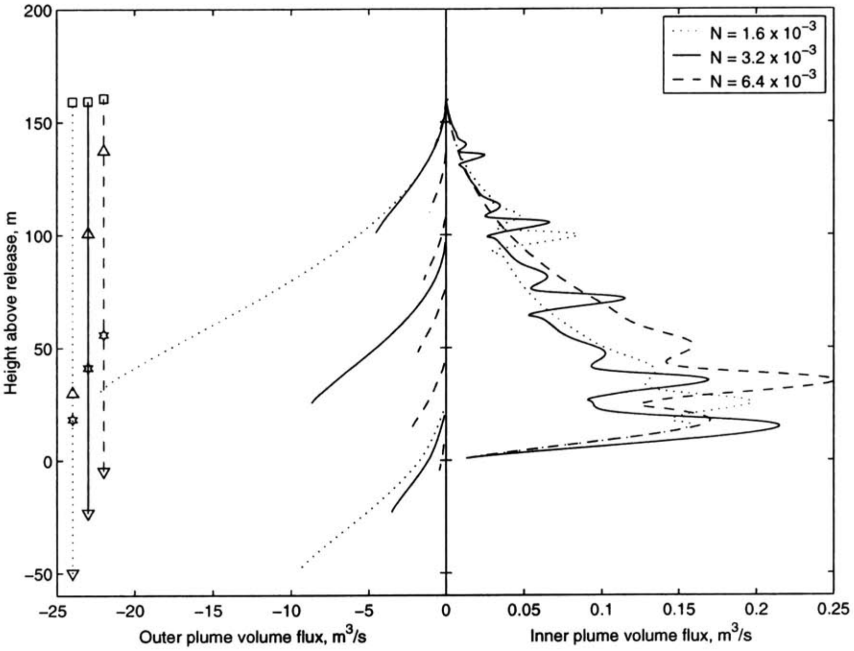

Figure 4-22: Sensitivity of plume structure to ambient stratification.

stratification.

Figure 4-23 illustrates the relationship between mean intrusion CO_2 concentration and the strength of stratification. The slope of the log-log line fitting the three points is 1.14.

Flow Rate

To explore the changes in plume behavior with the flow rate of CO_2, the latter was varied over a range from 10 g/s to 1000 kg/s. For reference, a 500 MW coal-fired power plant produces about 130 kg/s of CO_2 [39]. Figure 4-24 shows that, except for the highest flow rates, the plume height is rather insensitive to flow rate. More striking is the decrease of the top intrusion and mean intrusion heights. The increasing length of the uppermost intrusion is due to an increase in the CO_2 concentration. Figure 4-25 shows how the CO_2

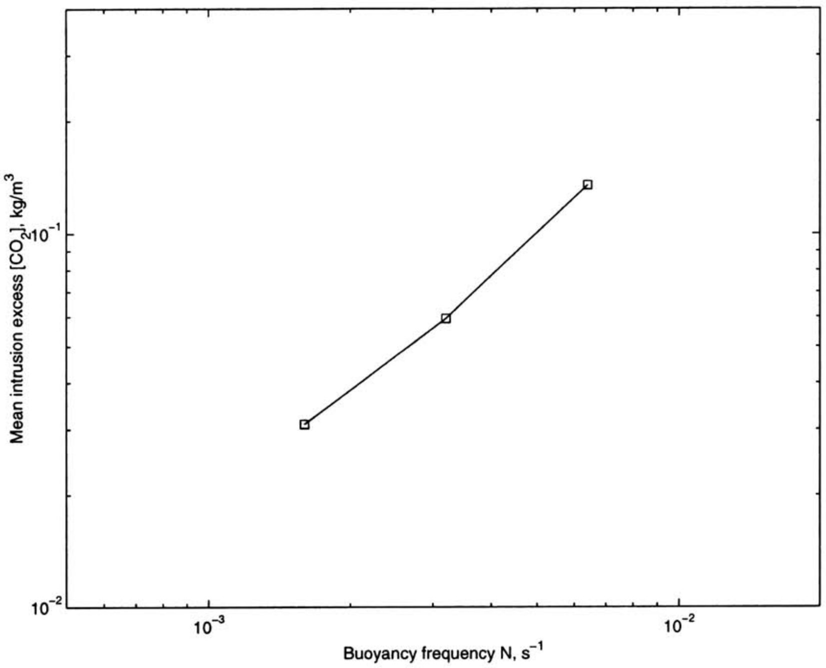

Figure 4-23: Sensitivity of CO_2 concentration to ambient stratification.

concentration in the intrusions leaving the flow increases with flow rate. This result is a strong argument for designing a CO_2 release which utilizes dispersed, low-flow diffusers.

Droplet Size and Dissolution Rate

Droplet size significantly affects dissolution rate because smaller droplets have a higher surface area to volume ratio. This effect is offset somewhat by the slower slip velocity, and hence mass transfer coefficient, of small droplets. Figure 4-26 summarizes the model response to changing droplet sizes. When droplets are very small, the inner plume is completely shrouded by one outer plume section which descends below the release point. With increasing droplet size, the plume height increases and multiple outer plume sections form. Interestingly, the length of the uppermost outer plume section (measured from the top of the plume to

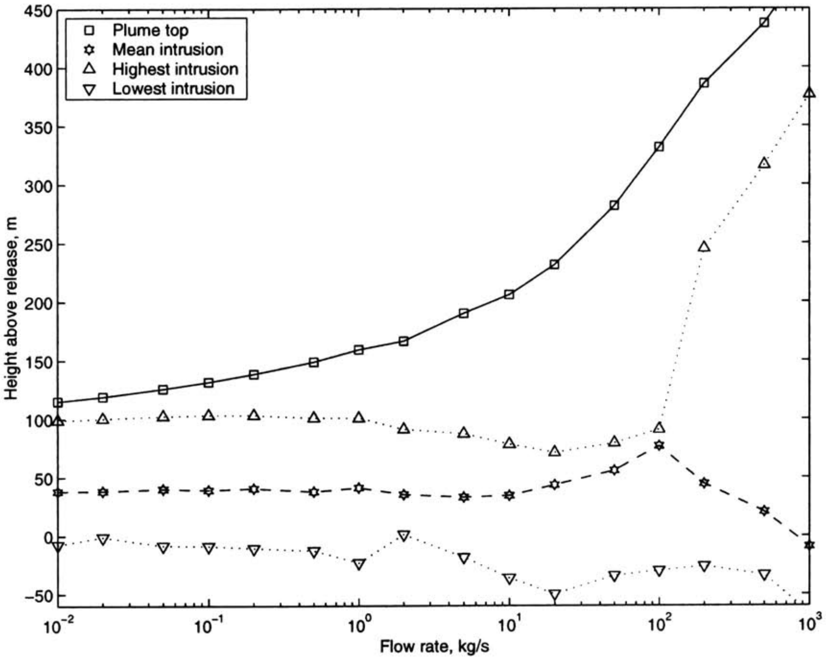

Figure 4-24: Sensitivity of plume structure to CO_2 flow rate.

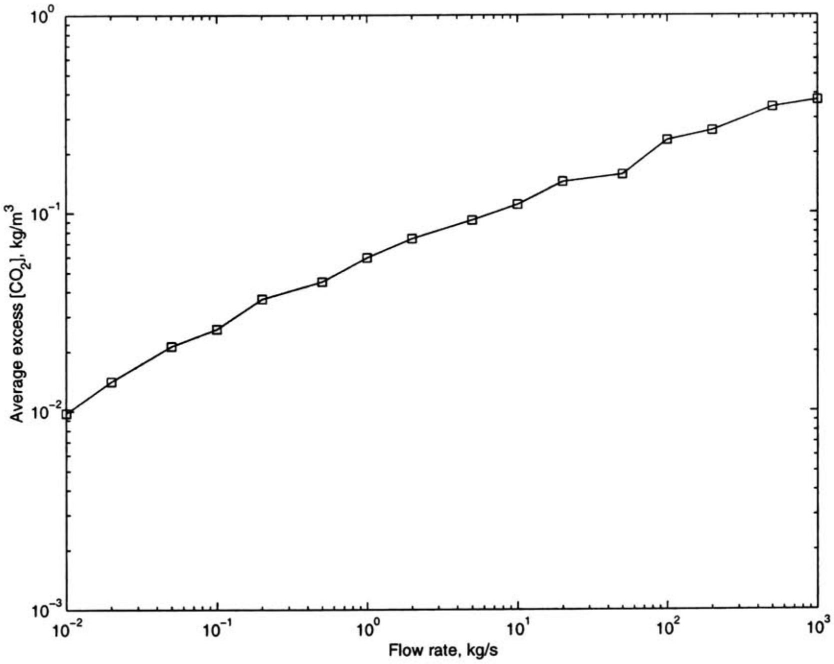

Figure 4-25: Sensitivity of CO_2 concentration to CO_2 flow rate.

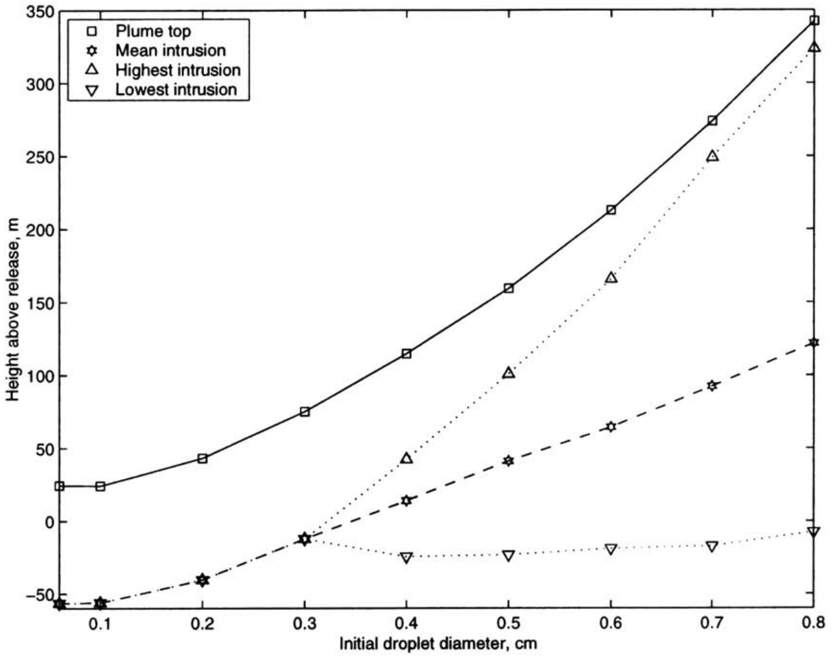

Figure 4-26: Sensitivity of plume structure to droplet size.

the highest intrusion) decreases with increasing droplet size.

The mean intrusion CO_2 concentration, shown in Figure 4-27, is not very sensitive to droplet size, just as it was insensitive to the mass transfer rate. This result is further evidence that the concentration of CO_2 in fluid leaving the plume is controlled by other factors, specifically the density effect and the strength of the ambient stratification.

The vertical scale of the modeled plume is quite sensitive to both droplet size and mass transfer rate. As the former is a design variable, and the latter a model parameter, it is of interest to vary both factors simultaneously in order to evaluate whether changing droplet sizes can compensate for changes in mass transfer rate. To this end, model runs were generated in which the droplet diameter was varied over the range from 0.06 to 0.8 *cm*. The mass transfer reduction factor was varied from one to ten.

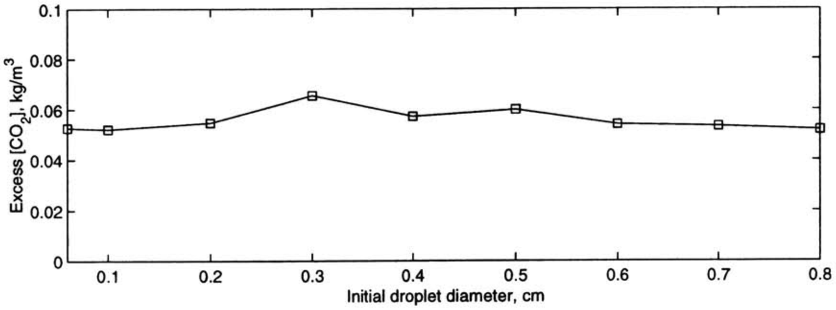

Figure 4-27: Sensitivity of CO_2 concentration to droplet size.

Model behavior in response to these variations is displayed in Figure 4-28. The maximum allowable plume height was limited to 450 meters, a height that was reached by 17 of the 63 combinations— as these plumes are essentially cut off at this height, the resultant intrusion heights and CO_2 concentrations are not valid. Plume heights and mean intrusion heights for the other 46 cases all increase with increasing droplet size and decreasing mass transfer rate (i.e. higher reduction factors). One interesting result is that the average CO_2 concentration in the intrusions does not vary systematically with either droplet size or mass transfer rate.

A contour plot of the plume height data is shown in Figure 4-29. This plot shows that, given a mass transfer rate, a target plume height can be reached by varying the initial droplet size over a reasonably small range. For example, in order to keep the plume under 200 meters tall, an order of magnitude reduction in the mass transfer rate can be balanced by reducing the droplet size by less than a factor of three.

For reference, Figure 4-29 can be compared with calculated rise heights for isolated, single droplets. These calculations were determined by only considering the droplet dynamics, and neglecting plume effects. These results are summarized in Figure 4-30. The ratio of the

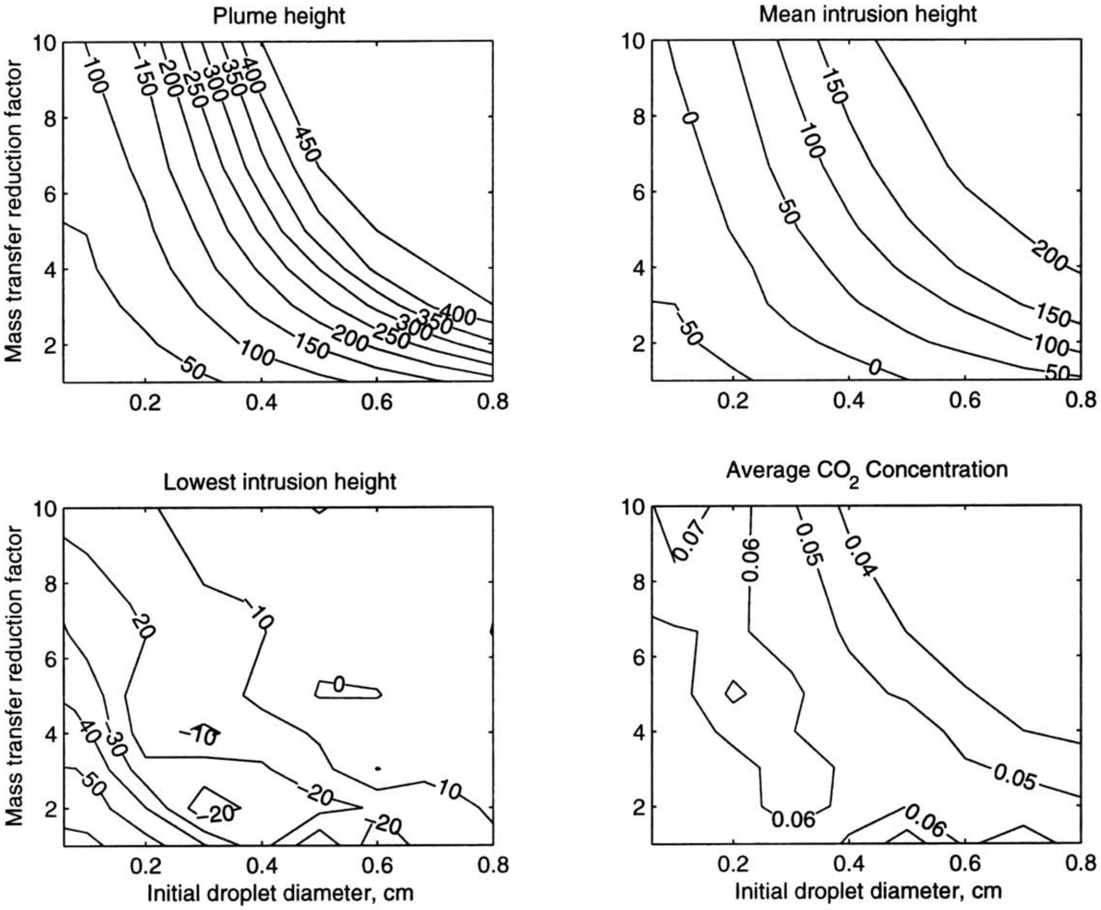

Figure 4-28: Sensitivity of CO_2 plume to droplet size and mass transfer rate. Plume height, mean and lowest intrusion heights, and mean CO_2 concentration are shown as a function of the initial droplet size and the mass transfer reduction factor.

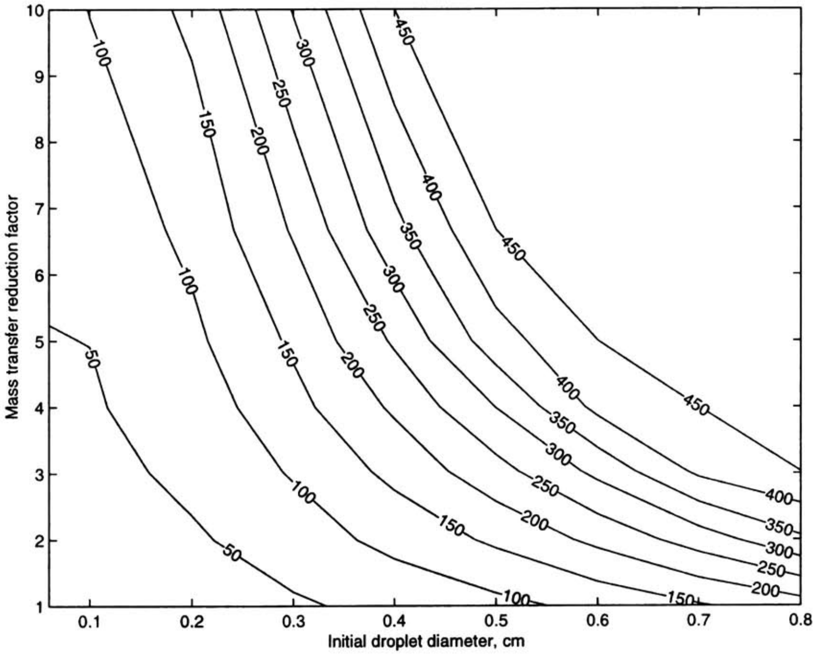

Figure 4-29: Sensitivity of plume height to droplet size and mass transfer rate. Contour lines show the total plume rise height as a function of initial droplet size and mass transfer reduction factor.

predicited plume heights to those of isolated droplets is shown in Figure 4-31, ignoring cases where the isolated droplets rise more than 450 meters. Plume effects result in the droplets rising two to four times higher than isolated droplets of intermediate size. The height ratio is insensitive to the reduction in the mass transfer rate.

4.3 Model Verification

The author is not aware of a dataset describing a two-phase plume with significant droplet dissolution which would be appropriate for evaluating the accuracy of this model. In fact, the absence of such information is one of the motivations for this study, in order to better plan the field experiment. However, it is imperative to assess model accuracy to whatever

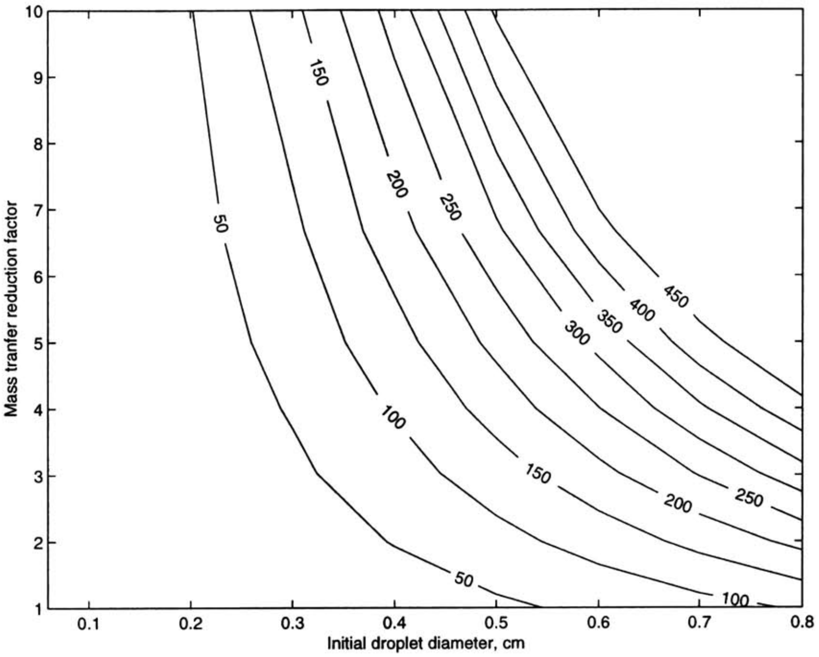

Figure 4-30: Droplet size vs. mass transfer rate, isolated CO_2 droplets. Contour lines show the total plume rise height as a function of initial droplet size and mass transfer reduction factor.

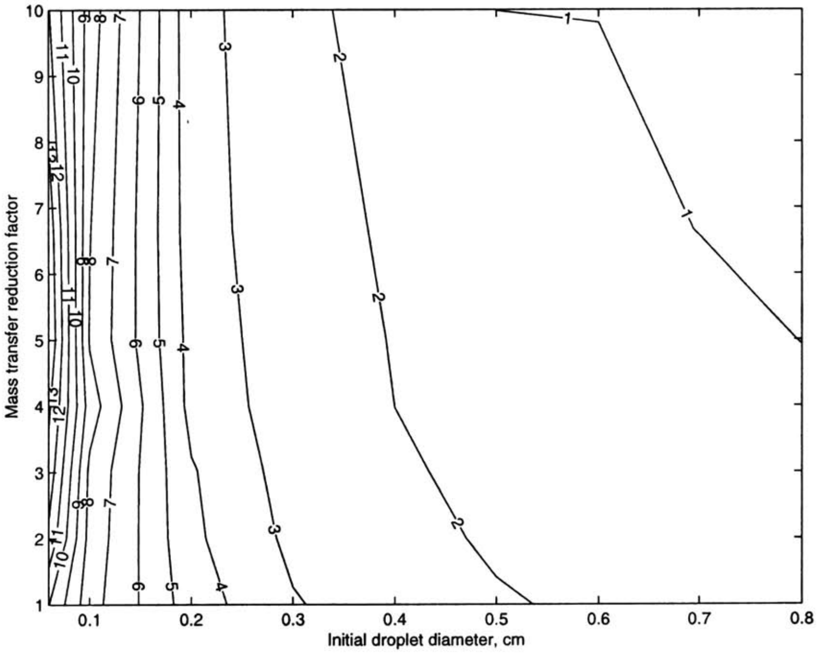

Figure 4-31: Plume height vs. isolated droplet rise height. Contour lines indicate ratio of plume height to the rise height of isolated droplets (no plume effect) for a given droplet size and mass transfer rate.

degree possible, so the model is compared against several different datasets and empirical equations describing plumes of varying similarity to the dissolving CO_2 droplet case. The test cases include comparison with the radius and velocity of a bubble plume in an unstratified environment, prediction of trap height for a (quasi-) single-phase plume, prediction of peel height for a two-phase plume in stratification, comparison with measured fluxes for a laboratory-scale stratified bubble plume, and comparison with velocity data obtained during the experiments described in Chapter 3.

4.3.1 Unstratified Bubble Plume

The highest quality dataset of a two-phase plume in an unstratified environment is that of Milgram [43], which has been described previously. This dataset consists of vertical velocity measurements recorded during large scale plume experiments. The experimental location was a 50 meter deep natural sinkhole, Bugg Spring. The normal (i.e. STP) air flow rates used in the experiments ranged from 2×10^{-4} to 5.9×10^{-1} m^3/s, which corresponds to the *in-situ* source buoyancy flux range of 3.3×10^{-4} to 9.6×10^{-1} m^4/s^3, owing to the compression of the air by a factor of six between the surface and the release depth of 50 meters. One of the factors contributing to the high quality of this dataset was the careful filtering of plume wandering effects, which consists of low frequency migration of the plume centerline from the geometrical centerline of the experimental domain.

To verify that the current model could properly simulate a two-phase plume in this simplified context, without stratification or dissolution, the model was run using the experimental parameters of the Milgram experiment in which the normal air flow rate was

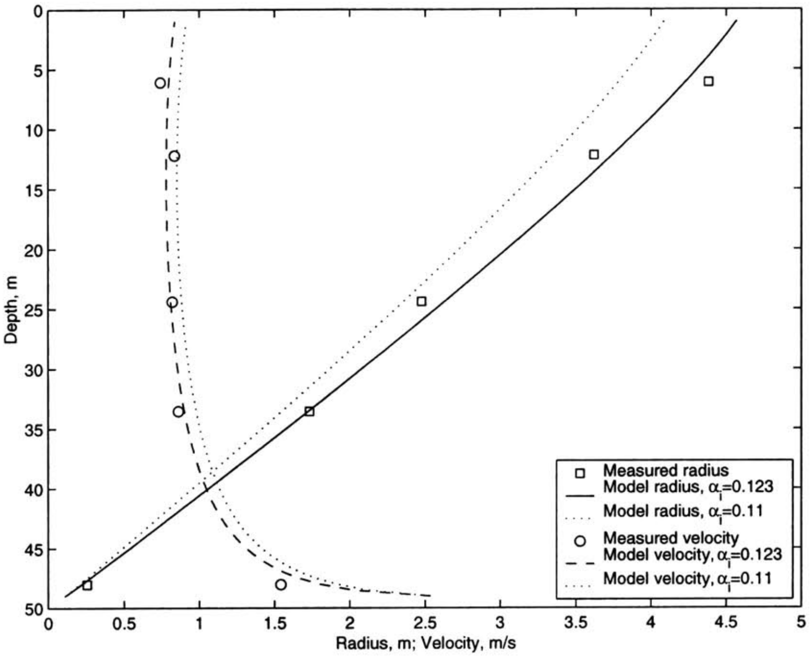

Figure 4-32: Simulation of a two-phase plume. Experimental data for $Q = 0.118\ m^3/s$ is from Milgram [43]. Model values are scaled to correspond to Gaussian profiles.

$1.18 \times 10^{-1}\ m^3/s$. The velocity and plume radius profiles predicted by the model are plotted against the experimental data in Figure 4-32. In order to make the comparison between the model's top-hat profiles and the experiment's Gaussian profiles, the model's velocity predictions were doubled and the radius predictions were reduced by a factor of $\sqrt{2}$, as described in Section 2.3.7. Using $\alpha_i = 0.123$, the model and data agree quite well. Using the pure plume value $\alpha_i = 0.11$, the fit is reasonable, but somewhat biased.

4.3.2 Trap Height of a Single-Phase Plume

Another test of the model is to check a well-known dimensional relationship for a single phase plume. The trap height (the mean height at which it intrudes into the ambient fluid) of a single phase plume in a stratified environment is given by the equation [65]

$$h_T = 3.8 \left(\frac{B}{N^3}\right)^{\frac{1}{4}}. \tag{4.1}$$

The present model can roughly simulate a single phase plume. This is achieved by artificially reducing the slip velocity and peeling parameters toward zero (setting either to zero causes numerical problems) and integrating the governing equations for the inner plume once, up to the point where the momentum flux approaches zero. The trap height was assumed to be the mean of the height at which the net buoyancy force of the plume first becomes negative and the point where the momentum flux neared zero; this method attempts to account for plume overshoot.. This was done for a release of CO_2 droplets at 800 meters, with $\alpha_i = 0.11$, the top-hat pure plume value [25]. The mass flux of CO_2 was varied from 10 grams per second to 10 kilograms per second, corresponding to a buoyancy flux ranging from $B_0 = 1.0 \times 10^{-5}\ m^4/s^3$ to $B_0 = 1.0 \times 10^{-2}\ m^4/s^3$. The buoyancy frequency N was $3.2 \times 10^{-3}\ s^{-1}$. The resulting trap heights are plotted against Equation 4.1 in Figure 4-33. The agreement between the model results and Equation 4.1 are reasonable, and improves with increasing source buoyancy flux. The exponent of a line fitted through the model data yields an exponent of 0.27 rather than 0.25.

4.3.3 Trap Height of a Two-Phase Plume

The height and volume flux of the lowest intrusion of a two-phase plume are functions primarily of B_0, N, and u_b, as described by Equations 1.3 and 1.4. To check the model's agreement with these trends, the base case model was run with no droplet dissolution. The

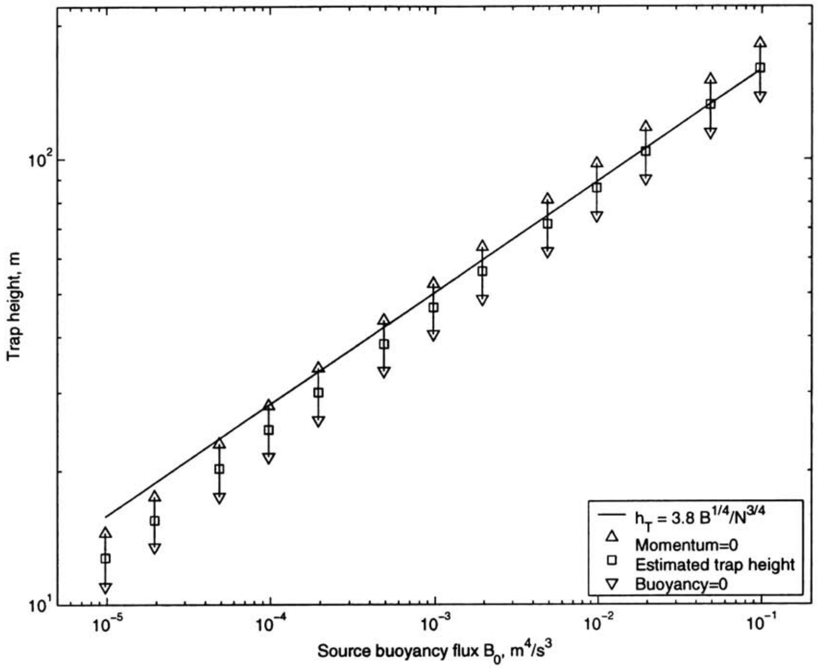

Figure 4-33: Prediction of the trap height of a single phase plume.

slip velocity was varied from 0.02 m/s to 0.14 m/s, which corresponds to dimensionless slip velocities ranging from 0.5 to 3.3. Of course, as the model implicitly assumes that the droplets remain in the inner plume, the model cannot describe Type 1* behavior for $U_N < 1$.

Also, the three entrainment schemes described in Section 4.2.1 were tested in order to evaluate the relative merits of each.

As illustrated in Figure 4-34, the parameter sets providing the best fit over the range $U_N < 3$ were based on the AI_A set $(2\alpha_i = \alpha_o = \alpha_a = 0.11)$, with α_i varying from 0.055 to 0.07. Given the scatter in the experimental data, no optimal parameter set is apparent. The other two entrainment regimes, AI_B and BC_A, predict trap heights that are significantly lower than the data and the predictions of Equation 1.3. Similar comments apply to Figure 4-35 and Equation 1.4.

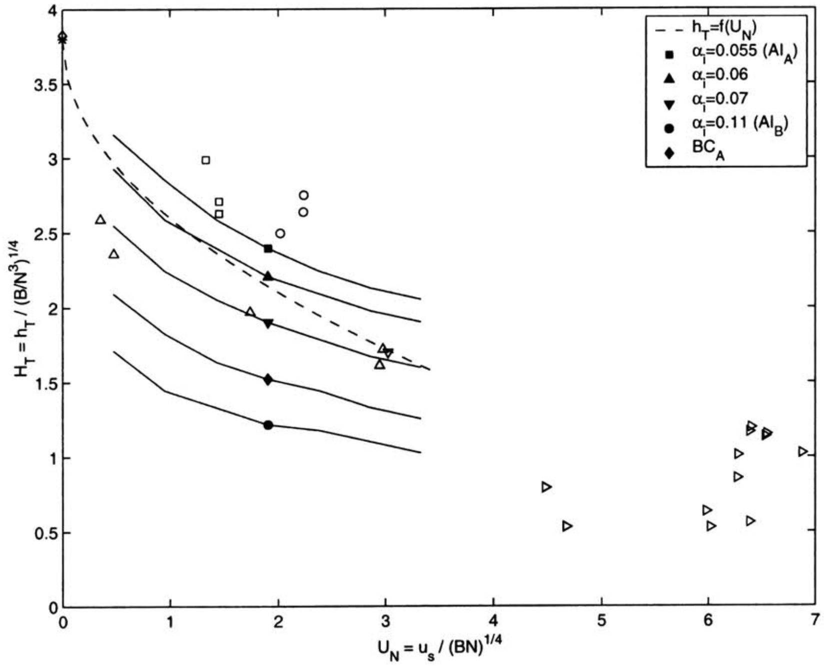

Figure 4-34: Height of the lowest intrusion: Model predictions, measurements, empirical fit. Open symbols represent experimental measurements: squares [59], circles [9], upward- and downward-pointing triangles [53], right-pointing triangles [37].

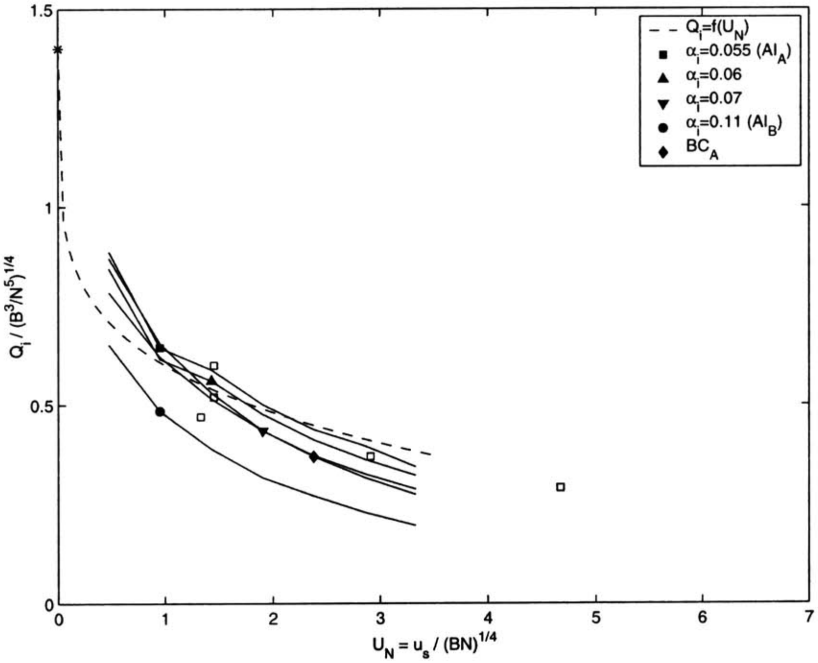

Figure 4-35: Volume flux in the lowest intrusion. Model predictions, measurements, empirical fit. Open squares represent experimental measurements from Socolofsky [59].

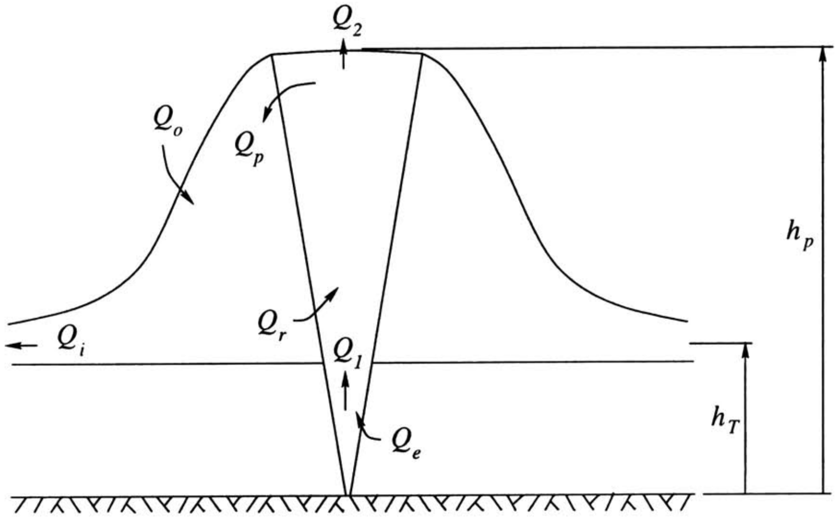

Figure 4-36: Schematic of the Socolofsky flux model. Source: Socolofsky [59].

4.3.4 Stratified Bubble Plumes

Socolofsky has developed a method for experimentally measuring gross fluxes of ambient fluid induced by two-phase plumes using a model depicted in Figure 4-36. The fluxes in the model are summarized in Table 4.3.

The current model was calibrated to agree with one of Socolofsky's preliminary bubble plume experiments. The experimental conditions were $Q_0 = 200\ mL/min$, $N = 0.33\ s^{-1}$,

h_p	Peel height: The highest point of a peeling event.
h_t	Trap height: Height where the outer plume intrudes.
Q_1	Volume flux of the inner plume just below h_t.
Q_e	Volume flux entrained below the outer plume, $= Q_1$.
Q_2	Volume flux of the inner plume above the first peel.
Q_o	Volume flux entrained by the outer plume.
Q_i	Volume flux of outer plume intruding into the ambient.
Q_p	Volume flux lost from the inner plume during peeling.
Q_r	Net recirculation flux between the inner and outer plumes.

Table 4.3: Flux model definitions associated with Figure 4-36.

and $u_b \approx 7\ cm/s$. Measurements compared against five different entrainment regimes: AI_A, AI_B, BC_A, and a best-fit regime with customized entrainment coefficients for both the AI and BC entrainment methods, referred to as AI_{bf} and BC_{bf}.

The measured and predicted fluxes are shown in Table 4.4 and plotted in Figure 4-37. The entrainment coefficients for the best-fit AI case were $\alpha_i = 0.04$, $\alpha_o = 0.11$, $\alpha_a = 0.06$, and the root mean squared error for between measurements and model results was 1.2 L/min. The entrainment coefficients for the best-fit BC case were $\alpha_i = 0.045$, $\alpha_o = 0.07$, $\alpha_a = 0.05$, and the root mean squared error was 1.0 L/min. The values of the entrainment coefficients are all reasonable, although one would expect α_a to approach the pure plume value of 0.11 as it applies to the single-phase portion of the flow. In contrast, none of the three basic entrainment regimes produce reasonable results. Although the AI_B scheme produces reasonable flux estimates, it predicts peel and trap heights that are half of those actually measured. The best prediction of the peeling and traps heights is produced by the AI_A approach, but even these values are not accurate. This result is not particularly troublesome, however, as entrainment coefficients can be expected to vary to some degree based on local plume conditions, as documented in the unstratified case by Milgram [43].

4.3.5 Counterflowing Plumes

The experiments described in Chapter 3 yielded rough velocity measurements at multiple heights for four different buoyancy flux ratios. The present model was modified slightly to simulate these experimental conditions; the primary modification was to set a stable initial condition for the descending outer plume at the depth of the brine diffuser. Modeled

	Measured	AI_{bf}	BC_{bf}	AI_A	AI_B	BC_A	Units
h_p	0.79	0.82	0.84	0.64	0.38	0.45	cm
h_t	0.51	0.51	0.49	0.41	0.22	0.26	cm
Q_1	24.2	20.5	21.0	24.4	23.0	27.1	mL/min
Q_2	3.6	2.9	2.5	2.8	4.4	3.7	mL/min
Q_o	20.4	23.3	22.4	32.6	20.5	26.0	mL/min
Q_i	43.1	41.5	42.3	57.3	36.7	49.6	mL/min
MSE	-	1.2	1.0	4.7	1.64	2.3	mL/min

Table 4.4: Flux model comparison. Heights are in meters, fluxes are in mL/min. MSE represents the root mean square error between the models and the experimental results.

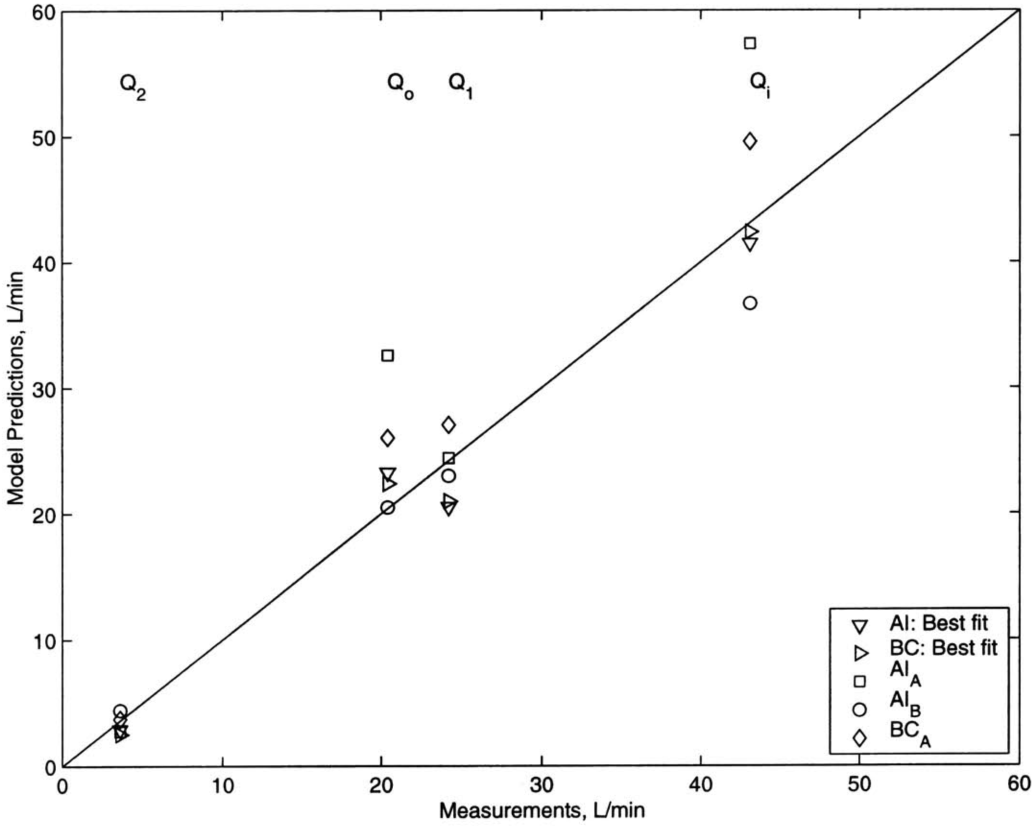

Figure 4-37: Comparison of model to experimental bubble plume data. Measured fluxes are plotted versus fluxes predicted by the model. For perfect agreement, the data points would lie on the diagonal line.

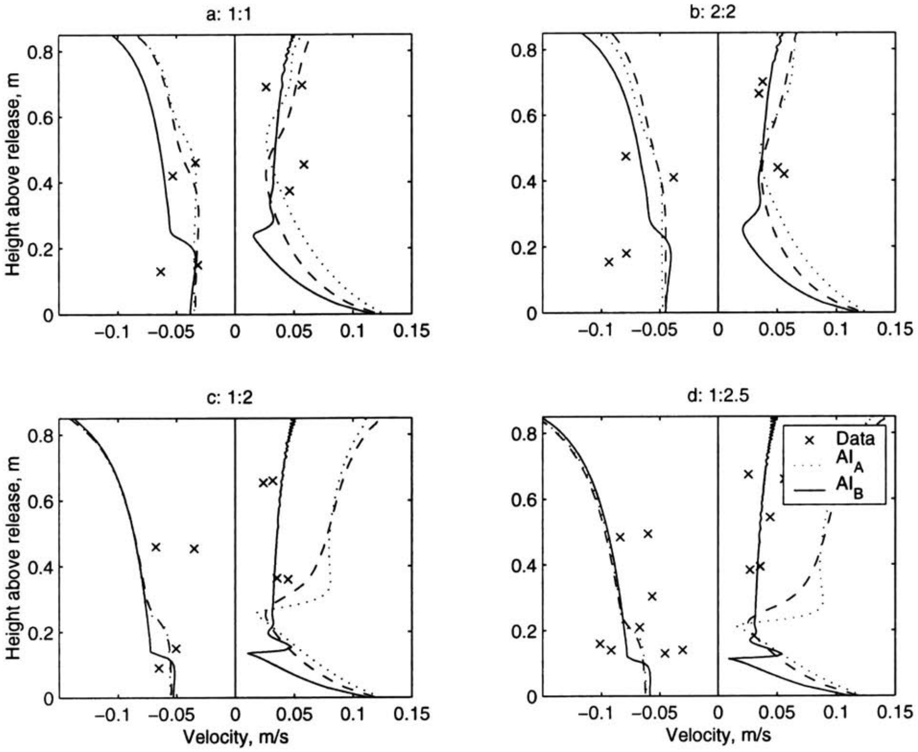

Figure 4-38: Comparison of model to experimental counterflow velocity data. The parameters describing the four cases *a*-*d* are summarized in Table 3.1.

velocity profiles are compared with the measured velocities in Figure 4-38. For cases (a) and (b), where the source buoyancy fluxes are equal, any of the three entrainment regimes, AI_A, AI_B, or BC_A, predict velocity profiles that are consistent with the admittedly rough measurements. However, for cases (c) and (d), where the negative buoyancy of the brine is greater than that of the bubbles, only AI_B produces velocity profiles that tend to agree with the data. The other two parameterizations tend to overpredict the inner plume velocity.

In this section, the present model has shown the ability to agree with a wide variety of empirical equations and experimental measurements. However, satisfactory agreement was only achieved by manipulating the entrainment coefficients on a case by case basis. This is not ideal in the current context, where the goal is to apply the model to a novel situation for which there is no experimental data. Fortunately, as was demonstrated in Section 4.2.1, the structure of a CO_2 droplet plume is not particularly sensitive to the exact entrainment formulation as it is strongly governed by dissolution and solute density effects.

4.4 Predictions

One goal of this work is to predict the characteristics of a pilot scale CO_2 plume in the context of the international field experiment described in Section 1.1.3. For a 1 kg/s release, an applicable prediction is the CO_2 base case described in Section 4.1.2. For this case, with a droplet diameter of 0.5 cm and a mass transfer reduction factor of 2, the plume rises 160 meters above the release point. The highest intrusion is located 100 meters above the release, the mean intrusion depth is about 40 meters above the release point, and the lowest intrusion is 20 meters below the release point. Of these height predictions, the last one is the most uncertain, as its location is determined by the depths of overlying intrusions. The excess DIC concentrations in the intrusions are about 0.06 kg/m^3, which translates to a depression of pH by 1.5 units.

These results are significantly different than those found by Alendal et al. [7] for a similar release into a still ambient which was described in Section 3.1. Using significantly larger droplets ($d_b = 1.4$ cm), that model predicted a rise height less than half that of the present model. The present predictions are much more conservative with respect to plume rise height. It is unclear whether the differences are caused by different mass transfer rates (Alendal et al. used a mass transfer correlation for droplets with mobile surfaces, and did not account for hydrate effects) or different velocity profiles near the droplet core, or both.

These results also differ from those described by Sato [55], which predict a plume rise height of $O(200\ m)$ for a release of approximately 200 kg/s of CO_2 at 2000 m, with initial droplet diameters of 1 and 2 cm. Sato found that the rise height did not vary significantly with droplet size, but that the effective dilution of CO_2 was greater for the larger droplet size. These findings are opposite those of this work, which found that plume height was sensitive to initial droplet size, but the intrusion CO_2 concentration was not.

Of course, the predictions of the present model are subject to the documented uncertainties in parameters such as the entrainment coefficients, the peeling parameter, and the rate of mass transfer. Uncertainty in these parameters affects the vertical distribution of the CO_2 more than it does the dilution, as the latter is primarily controlled by easily quantified factors such as the mass flow rate and the ambient stratification. Excluding the uncertainty of the mass transfer rate, but including uncertainty of the entrainment coefficients and the peeling parameter, the predicted plume height has an uncertainty of roughly ±30 percent. Given the numerous sources of uncertainty in the model parameters and in the model formulation itself, this assessment is meant as an estimate, rather than a hard number.

Chapter 5

Conclusions

Chapter 4 demonstrated that the model is reasonably consistent with the few cases against which it could be compared. It also showed that the model is moderately sensitive to several parameters whose values are not well known. The results also showed how plume behavior was affected by changing the design variables governing a CO_2 discharge. This chapter reviews the strengths and weaknesses of the model and the implications of the model results.

5.1 Model Limitations

The main weakness of the model is that it is fairly sensitive to parameterizations that are not well quantified, particularly the rates of entrainment between counterflowing plumes, and the peeling parameter. The uncertainty in plume behavior associated with the uncertainty of the values of these parameters limits the potential precision of the model.

The current treatment of droplet dynamics is another weakness. The model assumes that all droplets are of equal size and behave as solid spheres. Accounting for multiple droplet sizes is quite possible, merely requiring decomposition of the droplet mass flux into several mass fluxes, partitioned by size. The slip velocity and mass transfer of each could be calculated separately. As for the droplet dynamics, the main limitations are the lack of certainty about the mass transfer rate in the presence of CO_2 hydrates, and the effect of plume turbulence on both slip velocity and mass transfer.

The model assumes implicitly that all droplets remain in the inner plume. However, it appears that effective sequestration requires small droplet sizes. Such droplets, which have low slip velocities, are likely to be stripped from the inner plume either by turbulent entrainment or buoyant detrainment. This effect would probably result in less effective buoyancy in the inner plume, leading to shorter rise heights.

Also, it is not clear that small CO_2 droplets will resemble spheres due to hydrate formation. Especially small particles leaving the orifice may resemble a hydrate snow, with behavior different than that of spherical drops. Recent experiments conducted at the Southwest Research Institute have demonstrated such behavior [52].

The model is also not quite capable of simulating Type 3 plumes. As noted in Section 4.2.1, the model does predict decreasing mixing lengths and first intrusion heights with increasing U_N, but does not predict the type of outer plume behavior that is seen experimentally. This is most likely a product of the steady-state nature of the model; actual Type 3 plumes are somewhat unsteady.

This work is applicable only to the case where there is no ambient current, which obviously limits its applicability. However, the results of the other models indicate that the additional dilution of CO_2 due to a crossflow is only marginally greater than the stagnant case, indicating that consideration of the stagnant case yields pertinent results [7, 56].

A fundamental weakness is that this model takes the integral modeling approach to its limit. Integral plume models are best suited when the the profiles of the plume properties such as velocity and density difference are well-known and self-similar. As the property profiles in the complex flows of a dissolving CO_2 droplet plume may not be very self-similar, this model must be viewed more qualitatively than quantitatively.

5.2 Model Strengths

This model also has some unique strengths. First, it assumes that the fluid surrounding the droplet core is actually ascending, which is consistent with scoping experiments described in Chapter 3. Also, even though predictions of plume structure are fairly sensitive to parameter uncertainty, they are robust enough that they can be trusted as rough estimates. Furthermore, the predictions for excess CO_2 concentrations, and thus pH changes, in the plume intrusions are insensitive to parameters with uncertain values, with the possible exception of α_a. This appears to stem from the fact that the model is strongly constrained by the rate of droplet dissolution and the mixing induced by the density effect of dissolved CO_2 in the outer plume. Overall, the model is reliable enough to yield useful insight into the plume behavior.

5.3 Conclusions

There are a few major conclusions that can be drawn from Chapter 4. First, different plume properties are sensitive to different parameters. CO_2 concentrations leaving the plume increase with increasing mass flow rate and ambient stratification but are less affected by the droplet dissolution rate. Plume rise height, and the average and range of intrusion heights, in contrast, are more sensitive to the mass transfer rate. Reduction of the mass transfer rate, however, can effectively be countered by controlling the droplet size. For most runs, a (usually small) fraction of CO_2 enriched seawater descends below the injection point; this has implications for the environmental impact on benthic ecosystems and the design of the diffuser ports. The results also indicate that the plume has a strong negative feedback mechanism for controlling CO_2 concentrations leaving in the flow leaving the plume structure. In essence, the CO_2 concentration in fluid leaving the plume, which is nearly neutrally buoyant, is controlled by its negative buoyancy. Plume fluid with a higher CO_2 concentration, which increases the fluid density, requires more dilution before the fluid becomes neutrally buoyant. The strength of density stratification modulates this effect.

The model results provide guidance for designing a CO_2 droplet release. The initial droplet size, and, to a lesser extent, the flow rate of CO_2 control the plume height and the mean intrusion depth (given a specific mass transfer inhibition factor). The mass flow rate and the ambient stratification control the dilution of CO_2. As both the plume height and intrusion CO_2 concentration increase with increasing flow rate, an effective, low-impact sequestration scheme would require multiple, widely separated, low-flow diffusers, much like a sewage outfall.

Appendix A

CO_2 Equation of State

This model relies on the IUPAC equation of state for CO_2 [8].

The analytic equation of state, expressed explicitly in terms of the compressibility, Z, is

$$Z = 1 + \omega \sum_{i=0}^{9} \sum_{j=0}^{6} b_{ij} (\tau - 1)^j (\omega - 1)^i \tag{A.1}$$

where $\omega = \rho/\rho_1$, $\tau = T1/T$, $\rho_1 = 0.468\ g/cm^3$, and $T_1 = 304.2\ K$. The values of b_{ij} are shown in Table A.

This equation is not accurate near the critical point of CO_2, which is located at $T = 304.2\ K$ and $P = 73.86\ bar$. This equation is suitable to the current work because the ambient ocean conditions are never in the vicinity of the critical point.

Pressure is calculated from the expression

$$P = RT \frac{\rho}{M_{CO_2}} Z \tag{A.2}$$

	j=0	1	2	3
i=0	-0.725854437×10^{0}	-0.168332974×10^{1}	0.259587221×10^{0}	0.376945574×10^{0}
1	0.447869183×10^{0}	0.126050691×10^{1}	0.596957049×10^{1}	0.154645885×10^{2}
2	-0.172011999×10^{0}	-0.183458178×10^{1}	-0.461487677×10^{1}	-0.382121916×10^{1}
3	0.446304911×10^{-2}	-0.176300541×10^{1}	-0.111436705×10^{2}	-0.278215446×10^{2}
4	0.255491571×10^{0}	0.237414246×10^{1}	0.750925141×10^{1}	0.661133318×10^{1}
5	0.594667298×10^{-1}	0.116974683×10^{1}	0.743706410×10^{1}	0.150646731×10^{2}
6	-0.147960010×10^{0}	-0.169233071×10^{1}	-0.468219937×10^{1}	-0.313517448×10^{1}
7	0.136710441×10^{-1}	-0.100492330×10^{0}	-0.163653806×10^{1}	-0.187082988×10^{1}
8	0.392284575×10^{-1}	0.441503812×10^{0}	0.886741970×10^{0}	0
9	$-0.119872097\times10^{-1}$	$-0.846051949\times10^{-1}$	0.464564370×10^{-1}	0

	j=4	5	6
i=0	-0.670755370×10^{0}	-0.871456126×10^{0}	-0.149156928×10^{0}
1	0.194449475×10^{2}	0.864880497×10^{1}	0
2	0.360171349×10^{1}	0.492265552×10^{1}	0
3	-0.271685720×10^{2}	-0.642177872×10^{1}	0
4	-0.242663210×10^{1}	-0.257944032×10^{1}	0
5	0.957496845×10^{1}	0	0
6	0	0	0
7	0	0	0
8	0	0	0
9	0	0	0

Table A.1: Coefficients for the CO_2 Equation of State.

where $R = 8.3143\ J/mol\ K$ and $M_{CO_2} = 44.009\ g/mol.$

Fugacity may also be calculated using the equation of state:

$$\begin{aligned}\ln\left(\frac{f}{P}\right) &= -\ln Z + \left[2\sum_{i=0}^{9}\sum_{j=0}^{6}\frac{b_{ij}}{(i+1)}(\tau-1)^{j}(\omega-1)^{i+1}\right.\\ &\left.+\sum_{i=0}^{9}\sum_{j=0}^{6}b_{ij}(i)(\tau-1)^{j}\left(\frac{(\omega-1)^{i+1}}{(i+1)}+\frac{(\omega-1)^{i}}{i}\right)\right]_{0}^{\rho}.\end{aligned} \tag{A.3}$$

Appendix B

Seawater Equation of State

The ability to calculate seawater density based on relatively convenient measurements is quite useful in the field of physical oceanography. As a result, an accurate set of equations predicting seawater density as a function of temperature, salinity, and pressure has been developed [27]. The following equations calculate the seawater density $\rho_{sw}(S,T,P)$, where ρ_{sw} is in kg/m^3, temperature T is in degrees Celcius, salinity S is in practical salinity units, and the pressure P is in bars.

The density of water at one standard atmosphere $(P = 0)$ is

$$\begin{aligned}\rho_{sw}(S,T,0) = 999.842594 & \\ +6.793952 \times 10^{-2} \times T & \quad -9.095290 \times 10^{-3} \times T^2 \\ +1.001685 \times 10^{-4} \times T^3 & \quad -1.120083 \times 10^{-6} \times T^4 \\ +6.536332 \times 10^{-9} \times T^5 & \quad +8.24493 \times 10^{-1} \times S \\ -5.72466 \times 10^{-3} \times S^{\frac{3}{2}} & \quad +4.8314 \times 10^{-4} \times S^2\end{aligned} \tag{B.1}$$

$$
\begin{array}{ll}
-4.0899 \times 10^{-3} \times TS & +7.6438 \times 10^{-5} \times T^{2}S \\
-8.2467 \times 10^{-7} \times T^{3}S & +5.3875 \times 10^{-9} \times T^{4}S \\
+1.0227 \times 10^{-4} \times TS^{\frac{3}{2}} & -1.6546 \times 10^{-6} \times T^{2}S^{\frac{3}{2}}
\end{array}
$$

The density of water under pressure is

$$
\rho_{sw}(S,T,P) = \frac{\rho_{sw}(S,T,0)}{1 - \frac{P}{K(S,T,P)}} \tag{B.2}
$$

where

$$
\begin{array}{rll}
K(S,T,P) = 19652.21 & +148.4206 \times T & -2.327105 \times T^{2} \\
+1.360477 \times 10^{-2} \times T^{3} & -5.155288 \times 10^{-5} \times T^{4} & +3.239908 \times P \\
+1.43713 \times 10^{-3} \times TP & +1.16092 \times 10^{-4} \times T^{2}P & -5.77905 \times 10^{-7} \times T^{3}P \\
+8.50935 \times 10^{-5} \times P^{2} & -6.12293 \times 10^{-6} \times TP^{2} & +5.2787 \times 10^{-8} \times T^{2}P^{2} \\
+54.6746 \times S & -0.603459 \times TS & +1.09987 \times 10^{-2} \times T^{2}S \\
-6.1670 \times 10^{-5} \times T^{3}S & +7.944 \times 10^{-2} \times S^{\frac{3}{2}} & +1.6483 \times 10^{-2} \times TS^{\frac{3}{2}} \\
-5.3009 \times 10^{-4} \times T^{2}S^{\frac{3}{2}} & +2.2838 \times 10^{-3} \times PS & -1.0981 \times 10^{-5} \times TPS \\
-1.6078 \times 10^{-6} \times T^{2}PS & +1.91075 \times 10^{-4} \times PS^{\frac{3}{2}} & -9.9348 \times 10^{-7} \times P^{2}S \\
+2.0816 \times 10^{-8} \times TP^{2}S & +9.1697 \times 10^{-10} \times T^{2}P^{2}S &
\end{array} \tag{B.3}
$$

References

[1] CO_2 ocean sequestration field experiment. http://www.co2experiment.org.

[2] G. N. Abramovich. *The Theory of Turbulent Jets.* M.I.T. Press, Cambridge, Mass., 1963.

[3] E. E. Adams and H. J. Herzog. Environmental impacts of ocean disposal of CO_2. Technical Report MIT-EL 96-003, Energy Laboratory, Massachusetts Institute of Technology, 1996.

[4] E. Eric Adams, Jennifer A. Caulfield, Howard J. Herzog, and David I. Auerbach. Impacts of reduced pH from ocean CO_2 disposal: Sensitivity of zooplankton mortality to model parameters. *Waste Management*, 17:375–380, 1997.

[5] Eric Adams, Makoto Akai, Lars Golmen, Peter Haugan, Howard Herzog, Shigeo Masuda, Stephen Masutani, Takashi Ohsumi, and C. S. Wong. An international experiment on CO_2 ocean sequestration. In B. Eliasson, P. W. F. Reimer, and A. Wokaun, editors, *Greenhouse Gas Control Technologies*, pages 293–298. Elsevier Science Ltd., 1999.

[6] G. Alendal and H. Drange. Two-phase, near-field modeling of purposefully released CO_2 in the ocean. *J. Geophys. Res.: Oceans*, (submitted).

[7] G. Alendal, H. Drange, and F. Thorkildsen. Two-phase modeling of CO_2 droplet plumes. Technical Report 153, Nansen Environmental and Remote Sensing Center, 1998.

[8] S. Angus, B. Armstrong, and K. M. De Reuck. *International Thermodynamic Tables of the Fluid State.* Pergamon Press, 1976.

[9] Takashi Asaeda and Jörg Imberger. Structure of bubble plumes in linearly stratified environments. *J. Fluid Mech.*, 249:35–57, 1993.

[10] David I. Auerbach, Jennifer A. Caulfield, E. Eric Adams, and Howard J. Herzog. Impacts of ocean CO_2 disposal on marine life: I. A toxicological assessment integrating constant-concentration laboratory assay data with variable concentration field exposure. *Env. Model. and Assess. 2*, pages 333–343, 1997.

[11] W. D. Baines and A. M. Leitch. Destruction of stratification by bubble plumes. *J. Hydr. Engrg.*, 118(4):559–577, 1992.

[12] Jens Beyersdorf. *Verhalten von Luftblasen und Sedimenten in Blasensäulen in abhängigkeit vom Saltzgehalt im Wasser.* Mitteilungen, Heft 79, Franzius-Institut f. Wasserbau u. Küsteningenieurwesen, Universität Hannover, 1997.

[13] I. Brevik and R. Kluge. On the role of turbulence in the phenomenological theory of plane and axisymmetric air-bubble plume. *Int. J. Multiphase Flow*, 25:87–108, 1999.

[14] Peter G. Brewer, Gernot Friederich, Edward T. Petzer, and Franklin M. Orr Jr. Direct experiments on the ocean disposal of fossil fuel CO_2. *Science*, 284:943–945, 1999.

[15] Wallace S. Broecker. Thermohaline circulation, the achilles heel of our climate system: Will man-made CO_2 upset the current balance? *Science*, 278:1582–1588, 1997.

[16] Richard L. Burden and J. Douglas Faires. *Numerical Analysis.* PWS Publishing Company, Boston, 1993.

[17] Jennifer A. Caulfield, E. Eric Adams, David I. Auerbach, and Howard J. Herzog. Impacts of ocean CO_2 disposal on marine life: II. Probabilistic plume exposure model used with a time-varying dose-response analysis. *Env. Model. and Assess. 2*, pages 345–353, 1997.

[18] Klas Cederwall and John D. Ditmars. Analysis of air-bubble plumes. Technical Report KH-R-24, W. M. Keck Laboratory of Hydraulics and Water Resources, Division of Engineering and Applied Science, California Institute of Technology, Pasadena, California, September 1970.

[19] A.K. Chesters, M. van Doorn, and L. H. J. Goossens. A general model for unconfined bubble plumes from extended sources. *Int. J. Multiphase Flow*, 6:499–521, 1980.

[20] R. Clift, J. R. Grace, and M. E. Weber. *Bubbles, Drops, and Particles.* Academic Press, New York, NY, 1978.

[21] A. G. Dickson and C. Goyet, editors. *Handbook of Methods for the Analysis of the Various Parameters of the Carbon Dioxide System in Sea Water.* ORNL/CDIAC-74. Department of Energy, 1994.

[22] John D. Ditmars and Klas Cederwall. Analysis of air-bubble plumes. In *Proc. of 14th Int. Conf. Coastal Engrg., Copenhagen*, pages 2209–2226. ASCE, June 1974.

[23] T. Enns, P. F. Scholander, and E. D. Bradstreet. Effect of hydrostatic pressure on gases dissolved in water. *Journal of Physical Chemistry*, 89(2):389–391, 1965.

[24] Asghar Esmaeeli and Grétar Tryggvason. Direct numerical simulations of bubbly flows. Part 2. Moderate Reynolds number arrays. *Journal of Fluid Mechanics*, 385:325–358, 1999.

[25] H. B. Fischer, E. G. List, R. C. Y Koh, J. Imberger, and N. H. Brooks. *Mixing in Inland and Coastal Waters.* Academic Press, New York, NY, 1979.

[26] Y. Fujioka, K. Takeuchi, Y. Shindo, and H. Komiyama. Shrinkage of liquid CO_2 droplets in water. *International Journal of Energy Research*, 18:765–769, 1994.

[27] Adrian Gill. *Ocean-Atmosphere Dynamics.* Academic Press, New York, NY, 1982.

[28] Catherine Goyet. Spatial variation of total CO_2 and total alkalinity in the northern Indian Ocean: A novel approach for the quanitification of anthropogenic CO_2 in seawater. *Journal of Marine Research*, 57(1):135–163, 1999.

[29] Howard Herzog, Baldur Eliasson, and Olav Kaarstad. Capturing greenhouse gases. *Scientific American*, February 2000.

[30] S. Hirai, K. Okazaki, N. Araki, H. Yazawa, H. Ito, and K. Hijikata. Transport phenomena of liquid CO_2 in pressurized water flow with clathrate-hydrate at the interface. *Energy Convers. Mgmt.*, 37(6–8):1073–1078, 1996.

[31] S. Hirai, K. Okazaki, Y. Tabe, K. Hijikata, and Y. Mori. Dissolution rate of liquid CO_2 in pressurized water flows and the effect of clathrate films. *Energy*, 22(2/3):285–293, 1997.

[32] S. Hirai, K. Okazawi, Y. Tabe, and K. Kawamura. CO_2 clathrate-hydrate formation and its mechanism by molecular dynamics simulation. *Energy Convers. Mgmt.*, 38(Suppl.):S301–S306, 1997.

[33] P. D. Jones, D. E. Parker, T. J. Osborn, and K. R. Briffa. Global and hemispheric temperature anomalies–land and marine instrumental records. In *Trends: A Compendium of Data on Global Change.* Carbon Dioxide Information Analysis Center, Oak Ridge National Laboratory, U.S. Department of Energy, Oak Ridge, Tenn., U.S.A., 1999.

[34] C. D. Keeling and T. P. Wharf. Atmospheric CO_2 records from sites in the SIO air sampling network. In *Trends: A Compendium of Data on Global Change.* Carbon Dioxide Information Analysis Center, Oak Ridge National Laboratory, U.S. Department of Energy, Oak Ridge, Tenn., U.S.A., 1999.

[35] Helmut E. Kobus. Analysis of the flow induced by air-bubble systems. In *Proc. 11th Int. Conf. Coastal Engrg., London*, pages 1016–1031. ASCE, September 1968.

[36] A. M. Leitch and W. D. Baines. Liquid volume flux in a weak bubble plume. *J. Fluid Mech.*, 205:77–98, 1989.

[37] Charles J. Lemckert and Jörg Imberger. Energetic bubble plumes in arbitrary stratification. *J. Hydr. Engrg.*, 119(6):680–703, 1993.

[38] Sydney Levitus, John I. Antonov, Timothy P. Boyer, and Cathy Stephens. Warming of the world ocean. *Science*, 287:2225–2229, March 2000.

[39] C. R. Liro, E. E. Adams, and H. J. Herzog. Modeling the release of CO_2 in the deep ocean. Technical Report MIT-EL 91-002, Energy Laboratory, MIT, Cambridge, MA, June 1991.

[40] Per Christian Lund. Impact of CO_2 hydrates on ocean carbon dioxide deposition options. Technical report, Institutt for energiteknikk, April 1995.

[41] C. Marchetti. On geoengineering and the CO_2 problem. *Climatic change*, 1:59–68, 1977.

[42] Trevor J. McDougall. Bubble plumes in stratified environments. *J. Fluid Mech.*, 85(4):655–672, 1978.

[43] J. H. Milgram. Mean flow in round bubble plumes. *J. Fluid Mech.*, 133:345–376, 1983.

[44] L.A. Miller, W.K. Johnson, and M. Arychuk. Kona background survey, August 1999. Institute for Ocean Sciences, March 2000.

[45] Francois M. M. Morel and Janet G. Hering. *Principles and Applications of Aquatic Chemistry.* Wiley-Interscience, 1993.

[46] Yasuhiko H. Mori. Critique of 'CO_2 droplets in the ocean' by H. Teng and A. Yamasaki, *energy- the international journal*, 1997, 22, 751. *Energy*, 24(261–271), 1999.

[47] Yasuhiko H. Mori and Takaaki Mochizuki. Dissolution of liquid CO_2 into water at high pressures: A search for the mechanism of dissolution being retarded through hydrate-film formation. *Energy Convers. Mgmt.*, 39(7):567–578, 1998.

[48] B. R. Morton. Coaxial turbulent jets. *J. Heat and Mass Transfer*, 5:955–965, 1962.

[49] B. R. Morton, Sir G. I. Taylor, and J. S. Turner. Turbulent gravitational convection from maintained and instantaneous sources. *Proc. of the Royal Soc.*, A234:1–23, 1956.

[50] Wheeler J. North, Veronica R. Blackwell, and James J. Morgan. Studies of CO_2 hydrate formation and dissolution. *est*, 32(5):676–681, 1998.

[51] T. Ohsumi, N. Nakashiki, K. Shitashima, and K. Hirama. density change of water due to dissolution of carbon dioxide and near-field behavior of CO_2 from a source on deep-sea floor. *Energy Convers. Mgmt.*, 33(5–8):685–690, 1992.

[52] Masahiko Ozaki. Pers. Comm., 1999.

[53] Leah Sarah Reingold. An experimental comparison of bubble and sediment plumes in stratified environments. MS thesis, Dept. of Civ. and Envir. Engrg., MIT, Cambridge, MA, 1994.

[54] Rabindra N. Roy, Lakshimi N. Roy, Kathleen M. Vogel, C. Porter-Moore, Tara Pearson, Catherine E. Good, Frank J. Millero, and Douglas M. Campbell. The dissociation constants of carbonic acid in seawater at salinities 5 to 45 and temperatures 0 to 45 degrees C. *Marine Chemistry*, 1993.

[55] Toru Sato. Model. In *Proceedings of FEDSM 2000. 2000 ASME Fluids Engineering Division Summer Meeting.* ASME Fluids Engineering Division, 2000.

[56] Toru Sato. Pers. Comm., 2000.

[57] S. G. Schladow. Bubble plume dynamics in a stratified medium and the implications for water quality amelioration in lakes. *Water Resources Research*, 28(2):313–321, 1992.

[58] S. A. Socolofsky, B. C. Crounse, and E. Eric Adams. Bubble and droplet plumes in stratification I: Laboratory studies. In *Proc. IAHR 5th Int. Symp. Strat. Flow*, Vancouver, BC, July 10-13 2000.

[59] Scott A. Socolofsky. *Laboratory Experiments of Multi-phase Plumes in Stratification and Crossflow.* Ph.D. Thesis, Dept. of Civ. and Env. Engrg., MIT, Cambridge, MA, (in prep.).

[60] K. H. Tacke, H. G. Schubert, D. J. Weber, and Klaus Schwerdtfeger. Characteristics of round vertical gas bubble jets. *Metal. Trans. B*, 16B(2):263–275, June 1985.

[61] Mario N. Tamburri, Edward T. Peltzer, Gernot E. Friederich, Izuo Aya, Kenji Yamane, and Peter G. Brewer. A field study of the effects of CO_2 ocean disposal on mobile deep-sea animals. *Marine Chemistry*, submitted.

[62] Ho Teng and Akihiro Yamasaki. Dissolution of CO_2 droplets in the ocean. *Energy*, 22(9):751–761, 1997.

[63] Ho Teng and Akihiro Yamasaki. Solubility of liquid CO_2 in synthetic sea water at temperatures from 278 k to 293 k and pressures from 6.44 mpa to 29.49 mpa, and densities of the corresponding aqueous solutions. *Journal of Chemical Engineering Data*, 43:2–5, 1998.

[64] J. S. Turner. jets and plumes with negative or reversing buoyancy. *Journal of Fluid Mechanics*, 26:779–792, 1966.

[65] J. S. Turner. Turbulent entrainment: the development of the entrainment assumption, and its application to geophysical flows. *J. Fluid Mech.*, 173:431–471, 1986.

[66] Robert P. Warzinski and Gerald D. Holder. Ocean storage of CO_2: experimental observations of calthrate hydrates in seawater. In B. Eliasson, P. W. F. Reimer, and A. Wokaun, editors, *Greenhouse Gas Control Technologies*, pages 1061–1063. Elsevier Science Ltd., 1999.

[67] R. F. Weiss. Carbon dioxide in water and seawater: the solubility of a non-ideal gas. *Marine Chemistry*, 2:203–215, 1974.

[68] David L. Wilkinson. Two-dimensional bubble plumes. *J. Hydr. Div.*, 105(HY2):139–154, 1979.

[69] Alfred Wüest, Norman H. Brooks, and Dieter M. Imboden. Bubble plume modeling for lake restoration. *Water Resour. Res.*, 28(12):3235–3250, 1992.

[70] Poojitha D. Yapa and Li Zheng. Simulation of oil spills from underwater accidents I: Model development. *J. Hydr. Res.*, 35(5):673–687, 1997.

[71] Richard E. Zeebe, D. A. Wolf-Gladrow, and H. Jansen. On the time to establish chemical and isotopic equilibrium in the carbon dioxide system in seawater. *Marine Chemistry*, 65:135–153, 1999.